University of Bath

PHD

Multiple scattering theory for supported nanoscale metal chains

Langridge, David J.

Award date:
2002

Awarding institution:
University of Bath

Link to publication

Alternative formats
If you require this document in an alternative format, please contact:
openaccess@bath.ac.uk

Copyright of this thesis rests with the author. Access is subject to the above licence, if given. If no licence is specified above, original content in this thesis is licensed under the terms of the Creative Commons Attribution-NonCommercial 4.0 International (CC BY-NC-ND 4.0) Licence (https://creativecommons.org/licenses/by-nc-nd/4.0/). Any third-party copyright material present remains the property of its respective owner(s) and is licensed under its existing terms.

Take down policy
If you consider content within Bath's Research Portal to be in breach of UK law, please contact: openaccess@bath.ac.uk with the details. Your claim will be investigated and, where appropriate, the item will be removed from public view as soon as possible.

Download date: 05. May. 2023

MULTIPLE SCATTERING THEORY FOR SUPPORTED NANOSCALE METAL CHAINS

Submitted by David J. Langridge
for the degree of
Doctor of Philosophy
of the University of Bath
2002

COPYRIGHT

Attention is drawn to the fact that copyright of this thesis rests with its author. This copy of the thesis has been supplied on condition that anyone who consults it is understood to recognise that its copyright rests with its author and no information derived from it may be published without the prior written consent of the author.

This thesis may be made available for consultation within the University library and may be photocopied or lent to other libraries for the purposes of consultation.

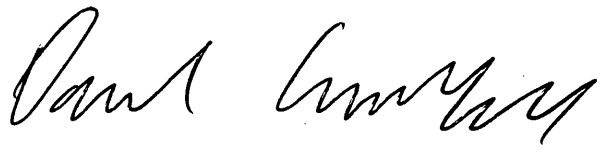

UMI Number: U153734

All rights reserved

INFORMATION TO ALL USERS
The quality of this reproduction is dependent upon the quality of the copy submitted.

In the unlikely event that the author did not send a complete manuscript
and there are missing pages, these will be noted. Also, if material had to be removed,
a note will indicate the deletion.

UMI U153734
Published by ProQuest LLC 2014. Copyright in the Dissertation held by the Author.
Microform Edition © ProQuest LLC.
All rights reserved. This work is protected against
unauthorized copying under Title 17, United States Code.

ProQuest LLC
789 East Eisenhower Parkway
P.O. Box 1346
Ann Arbor, MI 48106-1346

UNIVERSITY OF BATH
LIBRARY
45 - 5 FEB 2003
Ph. D.

Abstract

The ability to construct low-dimensional nanostructures of magnetic materials opens up a wide variety of interesting physical effects and applications. Until recently few studies have considered systems with one-dimensional periodicity. Recent progress in fabricating monatomic chains of atoms on surfaces provides the motivation for theoretical calculations on such systems.

In this thesis the layer multiple scattering method for performing electronic structure calculations on surfaces and interfaces is extended to allow for the treatment of systems with one-dimensional periodicity. A solution of the Poisson equation for a system with one-dimensional periodicity is developed. This involves one-dimensional lattice sums, the evaluation of which has necessitated the derivation of a Ewald sum technique for one-dimensional lattices. Comparison of the one-dimensional solution for arrays of chains to existing two-dimensional solutions confirms its accuracy.

Self-consistent electronic structure calculations for $3d$ chains on the Cu(001) surface have been performed for a variety of chain configurations, including single and multiple chains on the surface, embedded chains and step-edge type chains. Quantities calculated include local densities of states, total charges and magnetic moments. Results obtained are consistent with monolayer calculations using the layer multiple scattering method, and also with monolayer and adatom calculations in the literature.

The behaviour of the magnetic moments for the chain systems have been interpreted within a simple Stoner-like itinerant magnetism model. Trends in the moments across the $3d$ series, and between the various systems, are understood in terms of the interaction between states, with hybridisation between the d-orbitals of the $3d$ chain atoms themselves, and between the d-orbitals of the $3d$ chain atoms and the sp-orbitals of the Cu substrate, the principal mechanisms.

"The most merciful thing in the world, I think, is the inability of the human mind to correlate all its contents. We live on a placid island of ignorance in the midst of black seas of infinity, and it was not meant that we should voyage far. The sciences, each straining in its own direction, have hitherto harmed us little; but some day the piecing together of dissociated knowledge will open up such terrifying vistas of reality, and of our frightful position therein, that we shall either go mad from the revelation or flee from the deadly light into the peace and safety of a new dark age."

H. P. Lovecraft, The Call of Cthulhu

Acknowledgements

Firstly I would like to thank my supervisor, Dr Simon Crampin, for his invaluable help and guidance throughout this thesis.

Thanks must also go to the numerous people unfortunate enough to have been forced to share an office with me, especially Frank Hart, with whom I had many interesting discussions, some of which were even tangentially related to physics. I also need to mention the various reprobates in the physics department who have made living (and drinking) in Bath for the past five years enjoyable: a list in no particular order including (but not limited to) Hart, Hughes, Humphreys, Dodd, Partridge, Armitage and Moore. Thanks also to the members of the physics 7-aside football team, whose lack of fitness and ability ensured my time spent in goal was not inactive.

Lastly I would like to thank my parents, without whom this thesis would have been impossible for reasons too plentiful to list.

Contents

Chapter 1

Introduction

The electronic structure and magnetic behaviour of a material depend significantly on its structure and dimensionality. Only relatively recently have we seen the ability to tailor materials on the atomic scale, allowing construction of layer, row and adatom systems with monatomic precision. Construction of magnetic materials on the atomic scale, coupled with the high dependence of magnetic behaviour on structure and dimensionality, suggests many possible applications, e.g., in compact magnetic storage. Theoretical calculations of the electronic structure and magnetic properties of such systems are increasingly important in understanding the behaviour of magnetism in low-dimensional systems.

The transition metals, being on the borderline of magnetism, have attracted much interest in this regard. Transition metal structures on noble metal substrates can be considered as quasi-free systems, and thus represent close realisations of low-dimensional systems. In the past most experimental and theoretical studies have been concerned with two-dimensional systems, e.g., thin films and multilayers. While there has been some interest in adatom and cluster structures, very few studies have examined one-dimensional systems at surfaces, i.e., monatomic wires. Recent work has demonstrated that arrays of parallel monatomic chains can be deposited on vicinal surfaces [40]. Measurements of Co chains on the vicinal Pt(997) surface suggest the presence of local magnetic moments [24]. The experimental realisation of monatomic chains on surfaces provides the motivation for electronic structure calculations on such systems.

It is the aim of this thesis to develop an extension to the layer multiple scattering theory for electronic structure to enable the study of systems with one-dimensional periodicity, and to perform calculations of the electronic and magnetic structure of such systems. The structures that are examined are $3d$ transition metal wires on the Cu(001) surface. The results for these one-dimensional structures complement the existing calculations for $3d$ monolayers [5] and $3d$ adatoms [75] on the Cu(001) surface, giving a picture of the magnetic properties over the full range of dimensionality.

The remainder of this chapter discusses magnetism in low-dimensional systems, and examines previous experimental and theoretical work on one-dimensional systems.

Chapter 2 provides an overview of the methods used in electronic structure calculations, and gives a brief description of density functional theory, the framework within which the calculations are performed.

Chapter 3 details multiple scattering theory, the layer Korringa-Kohn-Rostoker (LKKR) Green function method for electronic structure calculations, and the extension of this method to the treatment of extended line defects.

Chapter 4 examines the solution of the Poisson equation, a vital step in the self-consistency cycle. In evaluating the Poisson contribution from a line defect there arise one-dimensional lattice sums; in order to evaluate these sums an extension of the Ewald sum technique to one-dimensional lattices is derived and tested.

Chapter 5 covers some of the steps required in the calculation of the electronic structure of a system, including the Brillouin zone integral, the energy contour integral, and the determination of the charge density. The convergence of one-dimensional defect calculations is examined with respect to the various parameters, including cluster size, $\mathbf{k}$-point set and angular momentum basis.

Chapter 6 presents results from electronic structure calculations on chains of $3d$ atoms on a Cu(001) surface. Densities of states and magnetic moments are compared between various chain systems, to clean surfaces, and to results from $3d$ monolayers on Cu.

Chapter 7 summarises the entire work, draws conclusions and suggests avenues for future work in this area.

The units used throughout this thesis, unless otherwise stated, will be atomic units, where

$$\hbar^2 = m_e = e^2 = 1 \tag{1.1}$$

with the Hartree (Ha) and the atomic unit (au) as the units of energy and length respectively,

$$1\text{Ha} = 27.2116 \text{ eV}, \quad 1\text{au} = 0.529177\text{Å}. \tag{1.2}$$

All graphs use electron volts (eV) as the units of energy and are scaled such that the energy zero is at the Fermi level.

1.1 Low-dimensional magnetism

The electronic and magnetic properties of a metallic system depend significantly on the dimensionality of the system. As the dimensionality is reduced quantum-size effects can give rise to exotic properties that have no equivalent in bulk systems. Surprising electronic phenomena are observed in a two-dimensional electron gas, e.g., fractional charge and the quantum Hall effect [122, 77]. The behaviour predicted for electrons confined to one-dimension is still more exotic. Electrons in one-dimension are predicted to behave as a Luttinger liquid, in which the electron loses its identity and separates into two quasiparticles, a spinon that carries spin but no charge, and a holon that carries the positive charge of a hole without spin [82]. While the Luttinger liquid state is a prediction for a true one-dimensional metal, the Peierls theorem [96] casts doubt on the existence of a metallic state in one-dimension. The Peierls theorem argues that a one-dimensional chain of atoms is unstable with respect to small displacements of the atoms, which creates an energy gap in the band structure near the Fermi energy, destroying the metallic character. One possible way round this restriction is to consider an atomic chain anchored to a surface, hence increasing the energy cost of displacing the atoms.

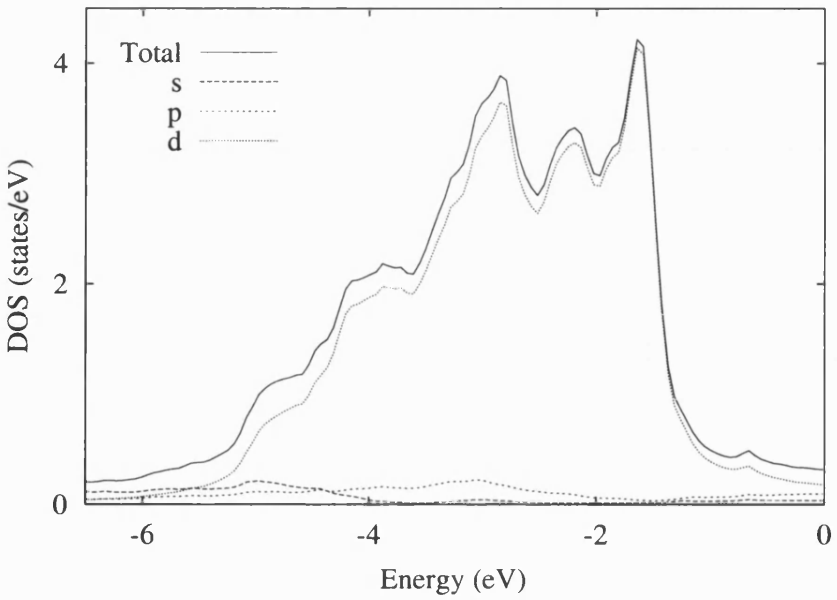

Figure 1.1: Densities of states for bulk Cu, showing the total and the s, p and d contributions.

Luttinger liquid behaviour is predicted for true one-dimensional systems. In the case of a monatomic metal chain on a metal surface, there will generally be some hybridisation between states in the chain and the surface. While this makes Luttinger liquid type behaviour unlikely in such systems, the low-dimensionality can still produce interesting electronic and magnetic effects.

The ability to tailor the structure and hence the magnetic properties of materials suggests interesting applications, especially in magnetic storage. Magnetic multilayers exhibiting giant magnetoresistance are one area in which considerable progress has been made, with applications including magneto-optical recording media, spin valve sensors, and magnetoresistive random access memory (MRAM) [5, 57]. Magnetic nanostructures offer the possibility of developing extremely compact devices with novel magnetic properties. Atomic wires suggest the eventual possibility of true nanoscale circuitry. Investigation of the properties of these structures is thus worthwhile, including the magnetic order and coupling between wires, average moment, interaction with the substrate, and magnetic anisotropy.

In the case of low-dimensional metallic systems, while these systems do not feature true confinement of electrons, the electronic and magnetic properties are still significantly affected [55]. Materials that are traditionally ferromagnetic can exhibit considerable enhancement in the size of the magnetic moment, and mate-

rials that are non-magnetic in the bulk can exhibit significant magnetic moments. Transition metal structures on noble metal surfaces are of particular interest in this respect, principally for two reasons. Firstly the interaction between transition metals and noble metals is relatively weak. This is because the main d-band component of the density of states (DOS) is located significantly below the Fermi level in noble metals, as opposed to straddling the Fermi level in transition metals. Figure (1.1) shows the DOS resolved into s-p-d contributions for bulk Cu. Clearly the d contribution is by far the most significant. The Cu d-band upper edge is about 1.5eV below the Fermi level, thus having little overlap with the d-band in transition metals. For Au and Ag the d-band edge is even lower in energy, about 2 and 3 eV below E_f respectively. This weak hybridisation means that transition metal structures on noble metal substrates can be considered as quasi-free systems.

Secondly, while Fe, Co and Ni are ferromagnetic as bulk crystals, many of the other transition metals are on the border of magnetism, making them good candidates to exhibit interesting changes in their magnetic behaviour. Numerous first-principles calculations have been performed for transition metal monolayers on noble metal substrates with the prediction that many of the monolayers should exhibit enhancements in their moments over their bulk values. An early full-potential linearised augmented plane-wave (FLAPW) study [38] predicted significant moments for Cr on Au(001), V and Fe on Ag(001), and Fe on Cu(001). Since then calculations have predicted large moments for $3d$ transition metal monolayers on Cu(001) [5] and on Ag(001) [13], and significant moments for some $4d$ and $5d$ transition metal monolayers on Ag(001) and Au(001) [9]. Figure (1.2) shows the calculated moments for $3d$, $4d$ and $5d$ transition metal monolayers on an Ag(001) surface [9]. Recent work has examined more complex structures and spin configurations, including calculations for several spin configurations of transition metal monolayers on Cu(111) and Ag(111) surfaces [72], calculations of multiple adlayers [11], and of sandwich type structures, e.g., multilayers of Fe on Au(001) with an overlayer of Au [20], and calculations of surface alloys, for example Mn alloys on Cu(001) [12] and Cu(111) [6] surfaces.

With the large moments seen for many transition metal adlayers on noble metal surfaces, it is natural to suppose that other low-dimensional structures will also be of interest. Isolated adatoms at surfaces represent the zero-dimensional limit for nanostructures on surfaces, and as such it is reasonable to expect that the

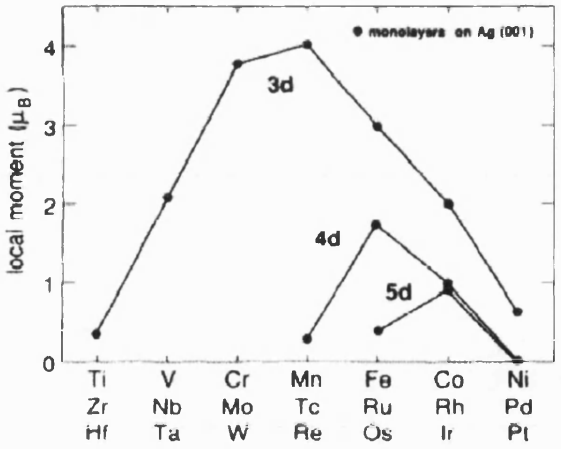

Figure 1.2: Local moments for $3d$, $4d$ and $5d$ monolayers on the Ag(001) surface [9].

further reduced dimensionality would lead to greater enhancement of the magnetic moments. Calculations for transition metal adatoms on noble metal surfaces support this view. $3d$ adatoms on the Cu(001) surface show considerable enhancement of their moments, while $4d$ and $5d$ adatoms on Ag(001) exhibit surprisingly large moments when compared to monolayer calculations [75]. Calculations have since been performed for numerous other adatom systems, including $3d$, $4d$ and $5d$ adatoms on Pd(001) and Pt(001) [119], $3d$ adatoms on Ni(001) and Fe(001) [90], and $4d$ adatoms on the same surfaces [91]. Figure (1.3) shows the calculated moments for $4d$ adatoms on the Cu(001), Ag(001) and Pd(001) surfaces [119].

Also of interest as low-dimensional systems are finite sized clusters on surfaces, including islands and finite length chains. These systems can be thought of as

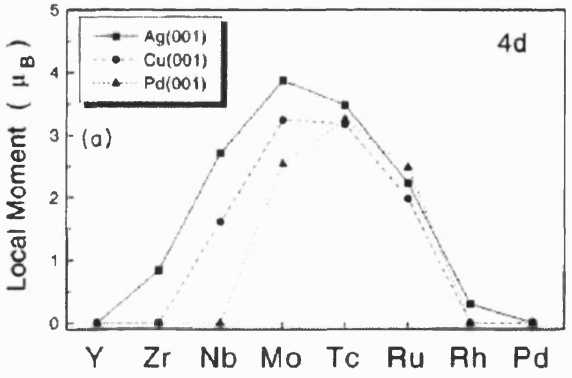

Figure 1.3: Local moments for $4d$ adatoms on the Cu(001), Ag(001), and Pd(001) surfaces [119].

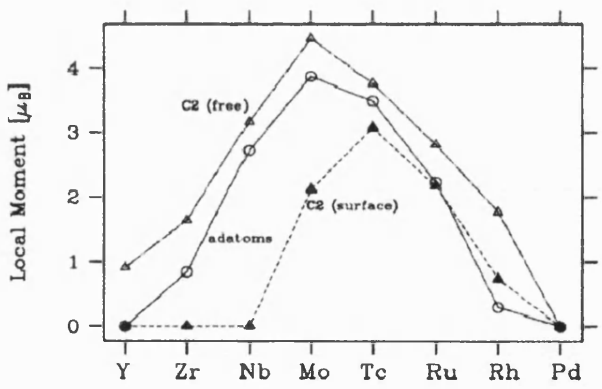

Figure 1.4: Local moments per adatom for $4d$ dimers(C2) and adatoms on the Ag(001) surface, and for $4d$ dimers in free space [128].

being intermediaries between monolayers and adatoms, thus for transition metal clusters on noble metal surfaces we would expect in many cases to see moments falling between the adatom and monolayer values. The magnetic moments for several finite chain and island clusters of $4d$ atoms on the Ag(001) surface have been calculated [128], with somewhat complex results. Broadly however, the moments for the chains and islands fall between the adatom and monolayer values, as expected. Figure (1.4) shows the moments for $4d$ dimers (2 atom chains) and adatoms on the Ag(001) surface, as well as $4d$ dimers in free space. As expected, the dimers on the Ag surface have smaller moments than the adatoms, but larger moments than the monolayer results shown in figure (1.2). Numerous calculations have since been performed for clusters on surfaces, including $3d$, $4d$ and $5d$ dimers on Ag(001) [118]. Rh clusters have been found to exhibit some surprising properties, with the local moments of Rh clusters strongly dependent on the number of atoms and the symmetry of the cluster [27, 125]. The moments for Rh dimers on Ag decrease sharply with increasing interatomic distance, in contrast to other transition metal dimers [117].

While two-dimensional (monolayer) and to a lesser extent zero-dimensional (adatom) and finite-sized low-dimensional (cluster) structures have received considerable attention very few studies have so far been presented for one-dimensional systems, i.e., monatomic chains.

Experimentally this is due to difficulties in realisation of these systems and in obtaining data from them. Theoretically the reduction in the symmetry of the system increases the computational costs. However, recent developments in experimental techniques have made progress in preparing and characterising one-

dimensional structures, and advances in computing power make *ab initio* studies of such systems feasible. The next section will give an overview of previous experimental and theoretical work on one-dimensional systems.

1.2 One-dimensional systems

There are a wide variety of one-dimensional systems that possess interesting physical properties. An interesting class of these is nanowires, freestanding wires between contacts ranging from the monatomic limit up to 10's of nanometres in width. There are a number of methods for production of freestanding nanowires, including manipulation of mechanically controllable break junctions [130], and combined scanning tunnelling/atomic force microscopies [107]. Numerous studies have been made of the mechanical, electrical and chemical properties of these structures, both experimentally and theoretically. The low-dimensionality of these structures leads to many interesting physical effects. Three-dimensional nanowires of Na are predicted to undergo a transition to a spin-polarised magnetic state at critical chain radii [131]. Calculations have been performed for the conductance of monatomic carbon atom wires (known as cumulenes) between metal electrodes, finding an oscillatory behaviour, with the resistance of chains comprising an odd number of carbon atoms being lower than that of a chain with an even number of atoms [73]. This effect is attributed to resonance states due to the interaction of the metal electrodes with the carbon wire. Calculations of the coupling between two such wires in parallel have also been carried out [74]. A similar result is obtained from first-principles calculations of monatomic Na wires - as is the case for the carbon nanowires above the conductance is found to be higher for chains comprising odd numbers of atoms [112]. In this homogenous system the oscillatory conductance is attributed to resonance states due to the sharp tip structure and local charge neutrality of the system. These conditions are believed to be common in other monovalent atomic wires, thus it is suggested that other monovalent atomic wires may exhibit this behaviour.

However, the focus of this thesis is on one-dimensional structures on surfaces, specifically chains of transition metal atoms on noble metal surfaces. The following two sections discuss previous experimental and theoretical progress in fabricating and understanding one-dimensional structures on surfaces.

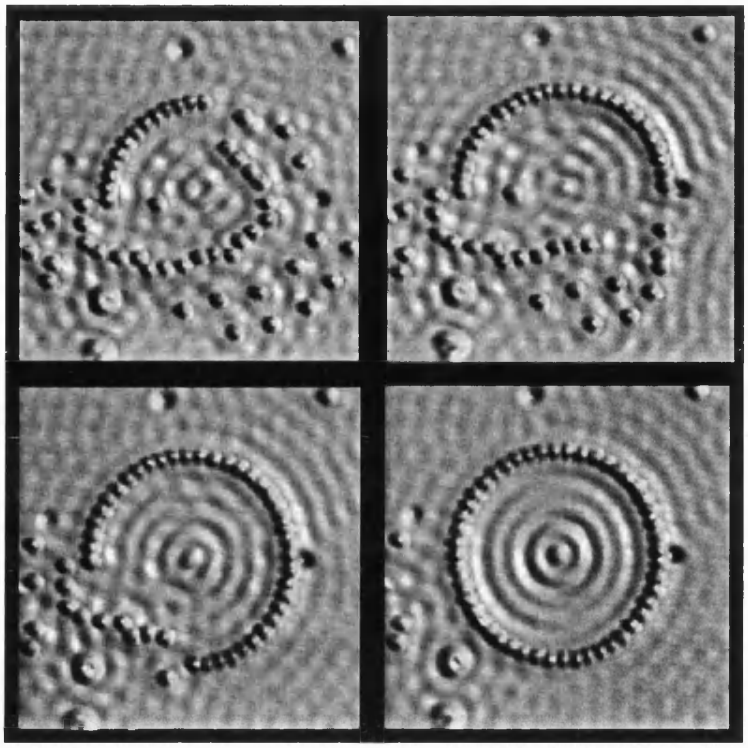

Figure 1.5: STM image of various stages in the construction of a 48 Fe atom corral on a Cu(111) surface [22].

1.2.1 Experiment

There are many methods for the generation of one-dimensional nanoscale structures at surfaces. The manipulation and positioning of single atoms on surfaces has been demonstrated by scanning tunnelling microscopy (STM) [22]. Figure (1.5) shows various stages in the construction of corral of 48 Fe atoms on a Cu(111) surface using STM to position the atoms individually. This technique allows the construction of arbitrary structures, however it does not permit the preparation of nanostructured large-area samples, which are required by standard experimental methods for band structure determination, such as photoemission and inverse photoemission. For these experimental probes an array of equally spaced one-dimensional structures is required. The spacing between the structures should be large enough to allow mostly intrachain interaction (e.g., weak interchain interaction), but small enough to ensure that the contribution from the one-dimensional structures to the photoemission spectra is significant.

Large-area samples with one-dimensional structures of nanometre scale can be

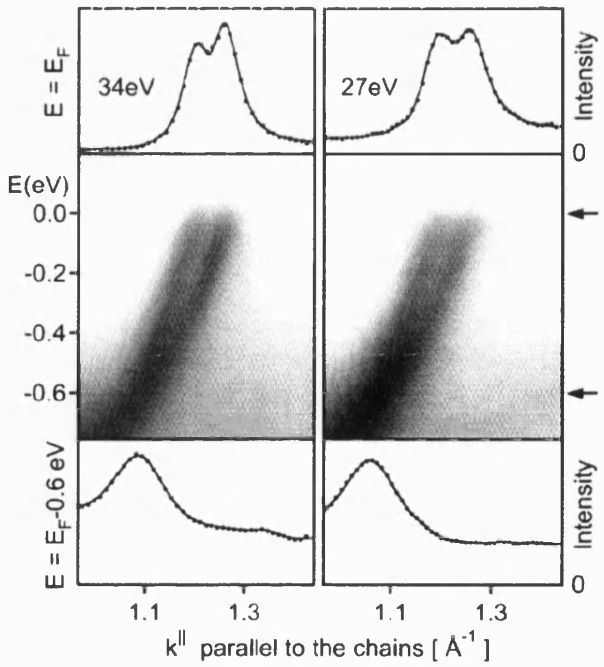

Figure 1.6: Band dispersion of the metallic surface state on Si(557)-Au near the Fermi level E_F. High photoemission intensity is shown dark. Two nearly degenerate bands are observed with a splitting that increases towards E_F. The momentum distributions at E_F (top panels) clearly show a splitting, while spinon and holon bands in a Luttinger liquid would have to converge at E_F [81].

synthesised by molecular beam epitaxy (MBE) exploiting the self-organisation of adatoms on anisotropic surfaces [106]. Examples of systems with one-dimensional structures grown by self-organisation include Cu, Pd and Fe chains on Pd(110) [106, 78], Gd on W(110) [95], Ir and Pd on W(110) [68] and Au on Ni(110), where a dimer-trimer chain structure is observed [103, 94]. In addition, some adsorbates on such surfaces have been found to self-organise into stripes, as in the case of O on Cu(110) [67].

Metallic chain structures can also be formed on semiconductor surfaces, an example being gold adsorbed on a stepped Si(111) surface. In this case two distinct one-dimensional structures are known, Si(557)-Au [110, 81, 80, 2] and Si(111)5×2-Au [80, 2], both of which exhibit chains of atoms along the [110] direction. Photoemission spectra from the Si(557)-Au surface found a one-dimensional metallic state at the surface, with a band splitting near E_F [110]. This splitting of the surface state was interpreted as an indication of spin-charge separation in a Luttinger liquid. Further photoemission studies of the same surface system suggest that this is not the case. Figure (1.6) displays photoemission data for the band

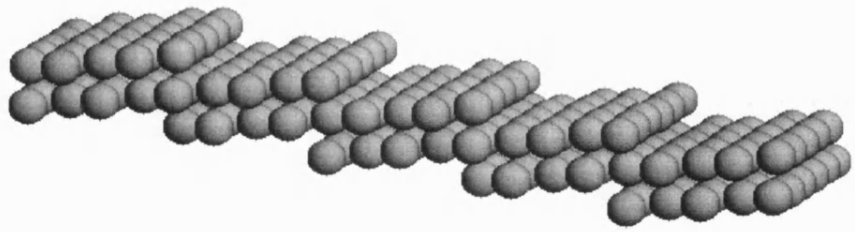

Figure 1.7: Diagram of a vicinal FCC(100) surface, in this case the (410) surface.

dispersion of the surface state, and clearly shows two nearly degenerate bands with a splitting at the Fermi level, ruling out the spinon-holon splitting predicted for a Luttinger liquid as spinon-holon bands have to converge at E_F [81]. An alternative interpretation is that of two metallic bands, corresponding to two chains in the unit cell [81]. This interpretation is in agreement with a recent theoretical calculation of the Si(111)5 $\times$ 2-Au surface [108].

Regular step arrays can be obtained on vicinal metal and semiconductor surfaces, effectively acting as an array of one-dimensional structures. It is possible to attain highly regular arrays of such steps, e.g., a stepped Si surface with only 1 kink per 20000 lattice sites [124]. Step decoration can then be used to grow nanowires, with the periodic arrays of steps acting as templates for step flow growth. In step decoration metal adatoms are deposited via MBE onto the stepped surface, where the step ledges act as preferential nucleation sites. There are numerous examples of the application of this technique for different surfaces and adatoms, including rare gases and metals on a vicinal Pt(997) surface [84], Cu on Mo(110) [101, 61, 62], Cu on W(110) [62] and Co on Cu(111) [25]. Figure (1.7) shows an example of a stepped FCC surface. The surface comprises (100) terraces separated by (110) steps, the terraces between the steps are 4 atoms wide, corresponding to a (410) vicinal surface. For more information on the classification of high Miller index surfaces, see [123]. Figure (1.8) shows the same surface with a single row of adatoms decorating the step-edges.

Low-dimensional analogues to all the classic thin-film growth modes are seen when decorating steps. Cu grows on a stepped Mo(110) surface in parallel stripes, a row-by-row growth mode that is equivalent to thin-film layer-by-layer growth [62]. For Cu on W(110) only the first row of Cu atoms decorate the step-edge,

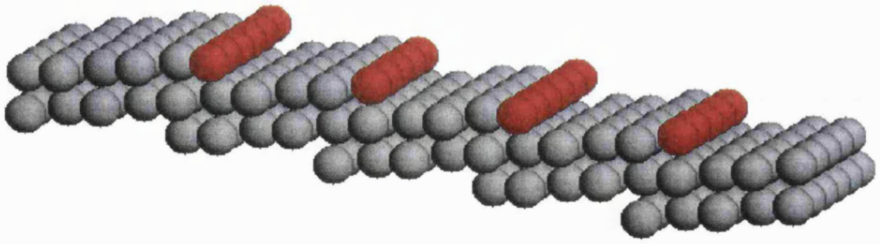

Figure 1.8: Diagram of an FCC(410) surface, with a single chain of adatoms decorating each step.

with additional Cu atoms forming monolayer height islands attached to the step-edges, the equivalent of Stranski-Krastanov growth [62]. The equivalent of island growth has been observed for Co on stepped Cu(111), Co islands nucleate at the step-edges, and eventually coalesce to form stripes at higher coverage [25].

Recent work has demonstrated that it is possible to grow high density arrays of parallel monatomic nanowires of Ag and Cu [40] and Co [39] on a vicinal Pt(997) surface. Figure (1.9) shows an STM image of a Pt(997) surface with monatomic Ag wires decorating the step-edges [24].

Epitaxial growth of Fe on W(110) results in one-dimensional stripes of Fe atoms

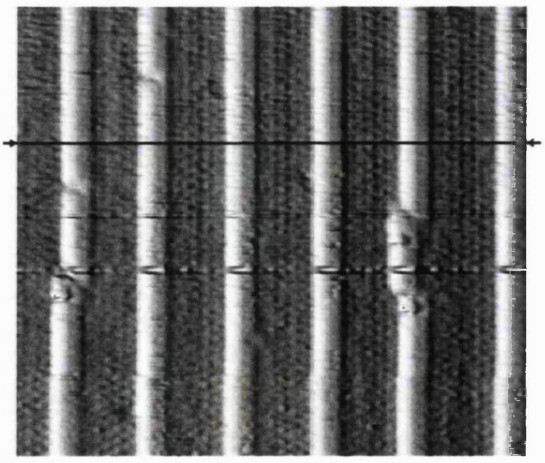

Figure 1.9: STM image of single monatomic Ag wires decorating the step-edges of a vicinal Pt(997) surface [24].

at step-edges, which were found by spin polarised low energy electron diffraction (SPLEED) to be ferromagnetic down to an Fe coverage of 0.005 ML [31]. Narrowly spaced monolayer stripes of Fe on W(110) still exhibited ferromagnetism at a coverage of 0.5 ML, with an average stripe width of 20 atomic rows [54]. Fe stripes with a width of 5-15 atoms and a height of 1-2 atoms on a vicinal Cu(111) surface, with a coverage of 0.3 ML, were found to be ferromagnetic from magneto-optical Kerr effect (MOKE) measurements [111].

With regards to the electronic structure of one-dimensional systems, a notable inverse photoemission experiment has been performed for Cu on W(331) [56], in which an electronic state has been interpreted as a single-row state, attributed to monatomic chains of Cu atoms deposited on the steps of the W(331) surface.

The electronic structure of monatomic Co and Cu wires on vicinal Pt(997) has been probed in an angle resolved photoemission experiment [24]. A single photoemission feature was associated with the $3d$ emission of the monatomic Cu wires, while a $3d$ double-peak feature is observed for the Co wires, as shown in figure (1.10). This is interpreted as indicating the presence of a one-dimensional exchange-split band and of local magnetic moments. We can estimate the size of the moment on the Co chain using the rough guide that an exchange-split of 1eV corresponds to a moment of $1\mu_B$. From the exchange-split of 2.1eV, we have an approximate moment of $2.1\mu_B$ for the Co chains. This is a considerable enhancement over the bulk moment, and is consistent with theoretical calculations for Co chains on Pt(997) [7]. No in-plane spin polarisation was found for temperatures down to 100K. While theoretical predictions based on Ising chains of spins prohibit long range ferromagnetic order for $T > 0$ K [30], there are several other possible explanations for this lack. These include the possibility that the Curie temperature for the chains is less than 100K, and also that the spins could be oriented in the out-of-plane direction.

The magnetism of monatomic Co wires on Pt(997) has been investigated by X-ray magnetic circular dichroism (XMCD) [41]. The local orbital magnetic moment for a monatomic Co chain was found to be enhanced by a factor of about 5 over bulk Co, and by a factor of nearly 2 over a biatomic Co wire, demonstrating the high dependence of the local orbital magnetic moment on the dimensionality. While the spin magnetic moment is expected to be less dependent on the atomic coordination than the orbital magnetic moment, unpublished local

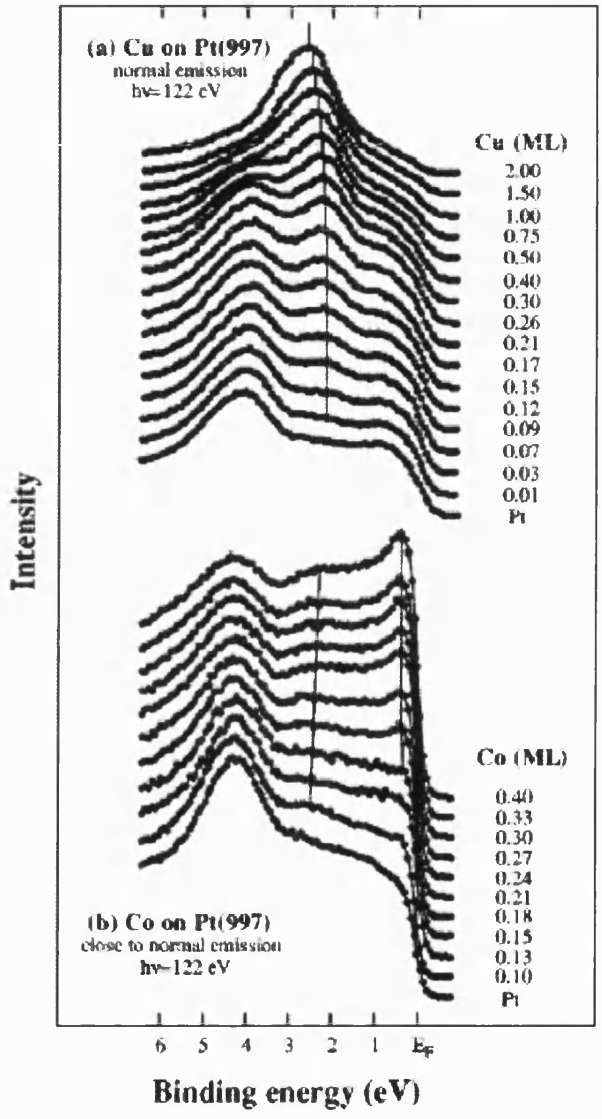

Figure 1.10: (a) Photoemission spectra taken at a photon energy of 122 eV displaying the development of Cu states on Pt(997) with increasing coverage. (b) Photoemission spectra taken at a photon energy of 122 eV displaying the development of Co states on Pt(997) with increasing coverage up to 0.40 ML. From [24].

spin density approximation (LSDA) calculations [7] indicate a small increase in the spin magnetic moment for a monatomic chain as compared to a monolayer. The magnetic anisotropy energy (MAE) was shown to be strongly affected by the dimensionality of the system, being considerably enhanced for monatomic chains as compared to monolayer results. The monatomic Co chains were also found to sustain both short- and long-range ferromagnetic order. At temperatures of less than 15 K there is a transition to a long-range ferromagnetically ordered state, contrary to the theoretical predictions for a one-dimensional Ising chain [30]. However, the model chain calculations do not take into account kinetic barriers preventing the system from reaching equilibrium, or interactions between the chain and the substrate.

Other methods for the fabrication of one-dimensional nanostructures include electrodeposition of metals onto a graphite substrate [98], laser focused atomic deposition [18], and filling pores in a polymer film with electroplated metals [8, 102, 79]. One-dimensional metallic edge states have also been observed for 2D slabs on semiconductors. The 1D edge states on MoS_2 islands can be viewed as examples of 1D conducting wires, and are the 1D equivalent to localised metallic surface states at semiconductor surfaces [14].

1.2.2 Theory

Theoretically, the treatment of one-dimensional structures on surfaces is difficult due to the loss of symmetry in going from three- to one-dimensional periodicity. For systems with two-dimensional periodicity, i.e., surfaces and interfaces, we have a unit cell which in principle is infinite in the direction normal to the surface. In practice calculations on such systems are often performed using a supercell (or slab) geometry. A surface system is modelled by a supercell comprising a slab of material surrounded by vacuum layers, which is then repeated periodically to restore periodicity. Figure (1.11) shows a cross-section view of the structure used in a typical supercell calculation of a surface. This method has two principal disadvantages. Firstly the size of the required unit cell is increased. Secondly it is an ersatz geometry, clearly not describing a true surface, with the possibility of interactions between the slabs.

For a system with one-dimensional periodicity there is even less symmetry. A

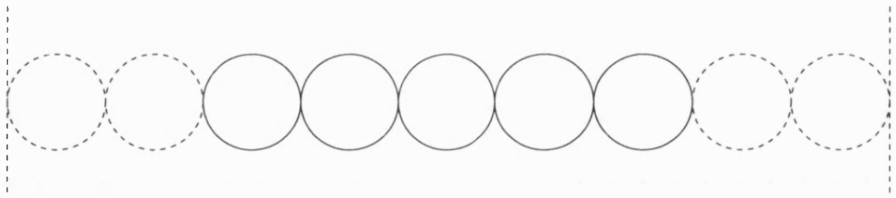

Figure 1.11: Cross-section of a 5 layer slab supercell geometry used to describe a surface. The dashed circles represent vacuum sites. This supercell is then repeated periodically to construct an infinite three-dimensional system.

single one-dimensional chain structure on a surface will in principle require an infinite unit cell in the directions normal to the surface and parallel to the surface but perpendicular to the chain axis. Again a similar type of supercell structure can be used, treating the chain as being part of an array of chains on the surface. However this will further increase the size of the required unit cell, and raise the prospect of interactions between the chains.

The high demands in computing power, combined with the paucity of experimental data on the electronic and magnetic structure of one-dimensional systems, have meant that until recently electronic structure calculations for one-dimensional systems were scarce.

Previous theoretical investigations of the electronic structure of one-dimensional surface systems include a first principles pseudopotential calculation of the Si(557)-Au surface [108]. As is mentioned in the previous section one-dimensional features are found on the surface of this system. Initial experimental work suggested that spin-charge separation of a Luttinger liquid was observed [110], however more recent data suggests the presence of two metallic bands [81]. The theoretical calculation predicts that the Au chains lead to two half filled metallic bands, supporting the latter interpretation.

First principles pseudopotential DFT calculations have also been performed for adsorbate atomic wires on an H-terminated Si(100) surface. These include calculations of the electronic structure of Ga [126] and As [129] atomic wires, and an LSDA calculation for Ga atomic wires which finds a ferromagnetic solution [93]. These pseudopotential calculations utilise a supercell geometry, with the first two using a slab with 5 layers of Si atoms, and the third using a slab with 8 layers of Si atoms. While pseudopotentials can be effective in describing these sorts of systems, they are much less efficient when describing materials with narrow

d-bands, e.g., the transition metals.

The magnetocrystalline anisotropy energy for free standing chains and rings of Fe adatoms has been calculated using a semi-empirical tight binding method [29], with the MAE showing a considerable enhancement over the freestanding monolayer value for both chains and rings.

The spin and orbital magnetic moments, and the MAE, have been calculated for free standing monolayers of Fe and Co with chain defects, using a self-consistent tight binding method [43]. Calculations were also performed for stepped monolayers, e.g., free standing vicinal layers. The orientation of the moments and the size of the MAE was found to depend on the orientation of the chain defects.

There have been few calculations performed for one-dimensional transition metal structures on surfaces. The MAE of freestanding Fe and Co chains, and of a Co chain deposited on a Pd(110) surface, has been calculated using a semi-empirical tight binding method [28], with the prediction of a perpendicular magnetic anisotropy in the deposited Co chain. Another semi-empirical tight binding calculation for Co chains on a Pd(110) surface has calculated the local magnetic moments and spin polarised local densities of states for various chain configurations, including isolated chains and adjacent chains with parallel and antiparallel magnetic coupling [105]. An 8% enhancement in the magnetic moment was found for a single Co chain compared with a Co monolayer.

The electronic and magnetic properties of Rh chains on Ag(001) surfaces have been investigated [3], again using a semi-empirical tight binding method, although the method used in this case takes explicit advantage of the one-dimensional symmetry of the chain systems. Several differing chain geometries were treated, with results for chains oriented along the $\langle 110 \rangle$ and $\langle 010 \rangle$ directions, for both adsorbed and embedded chains, and for arrays of up to 4 chains in width. The calculated magnetic moments were found to have some agreement with those found from *ab initio* KKR-GF calculations for finite sized Rh clusters on Ag(001) [128].

A recent paper presents *ab initio* calculations for $4d$ monatomic chains on vicinal Ag surfaces, using the screened-KKR GF method [4]. The results for these chains are complementary with previous calculations for adatoms, finite-length

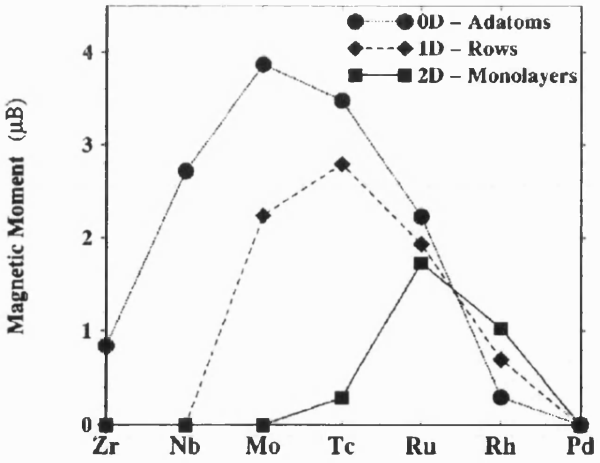

Figure 1.12: Local moments for adatoms [75], infinite close packed rows [4] and monolayers [10] of the $4d$ elements on the Ag(001) surface. From [4].

chains and monolayers, allowing the magnetism of these systems to be studied over the full range of dimensionality. Figure (1.12) shows the moments calculated for $4d$ monatomic rows on the Ag(001) surface, compared with results for adatoms [75], and monolayers [10]. As might be expected, the moments for the chains generally fall between the moments for the adatoms and the monolayers. With the increasing dimensionality the $4d$-$4d$ hybridisation increases, reducing the moments for the elements at the beginning and middle of the series, and the maximum moment is shifted towards higher valences. For three-dimensional systems, e.g., bulk crystals, this reduction is sufficient to quench the moments of all the elements, thus no $4d$ elements are ferromagnetic as bulk crystals.

Chapter 2

Electronic structure calculations

2.1 Introduction

The fundamental task in an electronic structure calculation is the solution of the time-independent Schrödinger equation, which for a fully-interacting many-electron system is given by

$$(T + V)\,\Psi = E\Psi, \tag{2.1}$$

where T is the kinetic energy operator and Ψ is the many-electron wave function. Due to the large number of electrons involved in bulk systems, the exact solution of this equation is impractical for all but the simplest of cases. Therefore it is necessary to use simplified Hamiltonians that capture as much of the physics as possible without becoming insolubly complicated.

The most common approximation used is the one-electron approximation, in which each electron is considered an independent particle moving in the mean field of the other electrons and the nuclei. This reduces the problem to solving the one-electron Schrödinger equation

$$\left(-\frac{1}{2}\nabla^2 + V_{\text{ion}} + V_{\text{c}} + V_{\text{xc}}\right)\psi_i = E_i\psi_i, \tag{2.2}$$

for the one-electron energies, E_i, and wave functions, ψ_i, where the total mean

field consists of contributions from the electrostatic field due to the nuclei, V_{ion}, and all the other electrons, V_{c}, plus corrections for exchange and correlation, V_{xc}.

In practice the Coulomb contribution is usually solved self-consistently. The Schrödinger equation is solved for some initial potential, V^{in}, from which the electronic charge density can be determined

$$\rho = \sum_{i}^{N} |\psi_i|^2. \tag{2.3}$$

This charge density is then used in a solution of Poisson's equation

$$-\nabla^2 V_{\text{c}} = 4\pi\rho, \tag{2.4}$$

which gives a new Coulomb potential. This is added to the potential from the nuclear charges, and from the exchange-correlation contributions to give a new total potential. It is not possible to use the new potential as the direct input to the next iteration of the cycle, the strong Coulomb forces tend to over-correct for charge imbalances and thus lead to unstable oscillations of charge in the system. Instead a weighted average of the initial and new potentials is used as the input for the next iteration of the cycle

$$V = \alpha V^{\text{old}} + (1 - \alpha) V^{\text{new}}, \tag{2.5}$$

where V^{old} and V^{new} are the original and calculated potentials respectively. Values of the mixing parameter α vary from of the order of 0.1 for bulk calculations down to as low as 0.001 for surface calculations, where charge neutrality is not guaranteed. For the chain defect calculations described in this thesis 0.01 was the typical value used. In order to accelerate the convergence cycle a Broyden mixing scheme [16] was employed. This involves the storage of previous sets of the potentials, but enables much faster convergence than simple linear mixing.

Once the new input potential has been generated, the cycle is then iterated until the two potentials are consistent. Figure (2.1) shows the steps involved in the self-consistency cycle. In determining the point at which the potentials can be said to be converged the difference parameter is defined as the new potential squared divided by the old potential squared, summed over all the grid points and sites. The potentials for the chain defect systems in this thesis are converged to a difference of less than 10^{-20}.

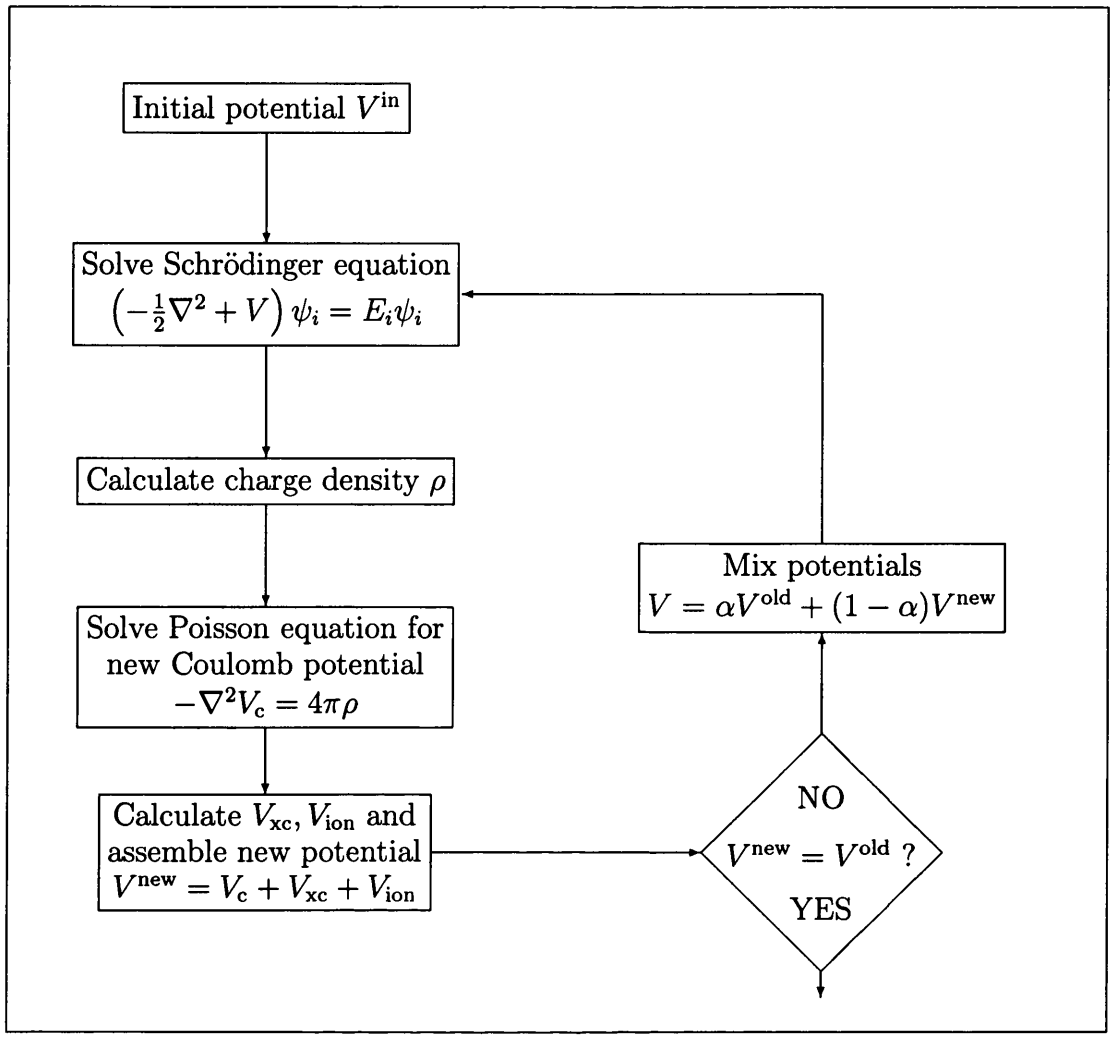

Figure 2.1: Illustration of a self-consistency cycle used in density functional electronic structure calculations.

There are various approaches to the form of the exchange-correlation term. In the Hartree approximation [53] the wave function is simply a product of non-interacting single-particle wave functions, hence no exchange or correlation effects between the electrons are considered, and thus no V_{xc} term appears. The Hartree-Fock approximation [37] extends the Hartree approximation to include the exchange interaction between the electrons by use of a Slater determinant wave function. Exchange is due to the Pauli exclusion principle, preventing electrons with identical spins occupying the same state. This leads to a non-local exchange term in the Schrödinger equation, making Hartree-Fock calculations computationally expensive, especially in the case of extended systems like bulk solids. While the inclusion of exchange effects gives a considerable improvement over the Hartree approximation, the Hartree-Fock approximation does not include correlation effects. Configuration interaction (CI) represents an attempt to

improve the Hartree-Fock approximation by inclusion of correlation effects. In principle CI leads to an exact wave function, however in practice the computational effort increases rapidly with the number of electrons in the system, thus only systems with relatively few electrons can be calculated accurately. In addition, the complexity of the resulting solutions makes interpretation of the results difficult.

For the treatment of bulk systems, it is desirable to have a method which scales well with the number of electrons in the system, includes both exchange and correlation effects, thus giving an accurate description of the electronic structure, while at the same time retaining the simplicity of the one-electron Schrödinger equation. Fortunately such a method exists, namely density functional theory.

2.2 Density functional theory

The basic theorems of DFT were derived by Hohenberg and Kohn [58]. Consider a system of N electrons moving in an external potential $V_{\text{ion}}(\mathbf{r})$ due to the ion cores. The Hamiltonian is given by

$$H = T + U + V, \tag{2.6}$$

where $V = \sum_i^N V_{\text{ion}}(\mathbf{r}_i)$, T and U are the kinetic energy and electron-electron interaction operators respectively. For all densities $n(\mathbf{r})$ which can be obtained from some antisymmetric wave function $\psi(\mathbf{r}_1, \mathbf{r}_2, \ldots, \mathbf{r}_N)$ the functional $F[n]$ is defined as

$$F[n] = \min_{\psi \to n} \langle \psi | T + U | \psi \rangle, \tag{2.7}$$

where the minimum is taken over all ψ that give the density n. $F[n]$ is independent of specific system or external potential details. Denoting E_{gs} , ψ_{gs} and $n_{\text{gs}}(\mathbf{r})$ to be the ground state energy, wave function and density respectively, the two fundamental theorems of density functional theory are

$$E[n] \equiv \int V_{\text{ion}}(\mathbf{r}) n(\mathbf{r})\, d\mathbf{r} + F[n] \geq E_{\text{gs}}, \tag{2.8}$$

and

$$\int V_{\text{ion}}(\mathbf{r}) n_{\text{gs}}(\mathbf{r})\, d\mathbf{r} + F[n_{\text{gs}}] = E_{\text{gs}}. \tag{2.9}$$

To prove (2.8) we define $\psi^n_{\text{min}}(\mathbf{r})$ as a wave function that minimises (2.7), i.e.,

$$F[n] = \langle \psi^n_{\text{min}} | T + U | \psi^n_{\text{min}} \rangle. \tag{2.10}$$

Recalling $V = \sum_i V_{ion}(\mathbf{r}_i)$, we have

$$\int V_{ion}(\mathbf{r}) n(\mathbf{r})\, d\mathbf{r} + F[n] = \langle \psi^n_{\text{min}} | V + T + U | \psi^n_{\text{min}} \rangle \geq E_{\text{gs}}, \tag{2.11}$$

due to the minimum property of the ground state. To prove (2.9) we once more use the minimum property

$$E_{\text{gs}} = \langle \psi_{\text{gs}} | V + T + U | \psi_{\text{gs}} \rangle \leq \langle \psi^{n_{\text{gs}}}_{\text{min}} | V + T + U | \psi^{n_{\text{gs}}}_{\text{min}} \rangle. \tag{2.12}$$

Subtracting the external potential terms gives

$$\langle \psi_{\text{gs}} | T + U | \psi_{\text{gs}} \rangle \leq \langle \psi^{n_{\text{gs}}}_{\text{min}} | T + U | \psi^{n_{\text{gs}}}_{\text{min}} \rangle. \tag{2.13}$$

However the definition of $\psi^{n_{\text{gs}}}_{\text{min}}$ gives the reverse inequality between the two sides of (2.13), which is only possible in the case where the two sides are equal, i.e.,

$$\langle \psi_{\text{gs}} | T + U | \psi_{\text{gs}} \rangle = \langle \psi^{n_{\text{gs}}}_{\text{min}} | T + U | \psi^{n_{\text{gs}}}_{\text{min}} \rangle. \tag{2.14}$$

Hence, completing the proof of (2.9)

$$\begin{aligned} E_{\text{gs}} &= \int V_{\text{ion}}(\mathbf{r}) n_{\text{gs}}(\mathbf{r})\, d\mathbf{r} + \langle \psi_{\text{gs}} | T + U | \psi_{\text{gs}} \rangle \\ &= \int V_{\text{ion}}(\mathbf{r}) n_{\text{gs}}(\mathbf{r})\, d\mathbf{r} + \langle \psi^{n_{\text{gs}}}_{\text{min}} | T + U | \psi^{n_{\text{gs}}}_{\text{min}} \rangle \\ &= \int V_{\text{ion}}(\mathbf{r}) n_{\text{gs}}(\mathbf{r})\, d\mathbf{r} + F[n_{\text{gs}}]. \end{aligned} \tag{2.15}$$

These two equations show that $E[n_{\text{gs}}] = E_{\text{gs}}$, the correct ground state energy. If we treat the ground state energy of a particular external potential as a functional of the density, $E[n]$ is a minimum at the true ground state density. That this is a useful property can be seen from the fact that $n(\mathbf{r})$ is a function of 3 variables whereas $\Psi(\mathbf{r_i})$ is a function of $3N$ variables. Since the ground state density determines the ground state wave function(s), from which all other ground state

properties can be found, these properties are therefore also functionals of the density. Thus (2.8) and (2.9) provide formal justification for basing calculations on the density.

These theorems provide a method for calculating ground state properties - assuming an approximation can be found for $F[n]$, we can then simply minimise $E[n]$ in (2.8) for the potential V_{ion} of interest. The ground-state electron density is the density which minimises the energy functional $E[n]$, which must satisfy the variational principle

$$\delta\left\{E[n] - \mu \int n(\mathbf{r})\, d\mathbf{r}\right\} = 0, \tag{2.16}$$

which yields the Euler equation

$$\mu = \frac{\delta E[n]}{\delta n(\mathbf{r})} = V_{\text{ion}}(\mathbf{r}) + \frac{\delta F[n]}{\delta n(\mathbf{r})}. \tag{2.17}$$

Here μ is the Lagrange multiplier associated with the constraint

$$\int n(\mathbf{r})\, d\mathbf{r} = N, \tag{2.18}$$

where N is the total number of electrons in the system.

2.3 Derivation of single-particle equations

To use the theorems of the preceding section to calculate ground state properties, it is necessary to find an expression for $E[n]$ in (2.8). This requires obtaining an approximation for the functional $F[n]$. In a method introduced by Kohn and Sham [70] we write the functional $F[n]$ as

$$F[n] = \frac{1}{2} \iint \frac{n(\mathbf{r})n(\mathbf{r}')}{|\mathbf{r} - \mathbf{r}'|}\, d\mathbf{r}\, d\mathbf{r}' + G[n], \tag{2.19}$$

where the double integral term is simply the classical Coulomb energy, and $G[n]$ is a universal functional of n. We then define $G[n]$ as

$$G[n] = T_s[n] + E_{\text{xc}}[n], \tag{2.20}$$

where $T_s[n]$ is the kinetic energy for a system of non-interacting electrons with density n moving in some external potential $V_s(\mathbf{r})$, and $E_{\rm xc}[n]$ is a term containing all the exchange and correlation effects. The exchange-correlation term, $E_{\rm xc}[n]$, which is not known exactly, contains all the electron-electron interactions beyond the Hartree approximation and the difference in kinetic energy between interacting and non-interacting electron systems. From (2.8) therefore, the energy functional is given by

$$E[n] = T_s[n] + \int V_{\rm ion}(\mathbf{r})n(\mathbf{r})\,d\mathbf{r} + \frac{1}{2}\iint \frac{n(\mathbf{r})n(\mathbf{r}')}{|\mathbf{r}-\mathbf{r}'|}\,d\mathbf{r}\,d\mathbf{r}' + E_{\rm xc}[n]. \tag{2.21}$$

All the terms in this expression can be evaluated exactly, with the exception of $E_{\rm xc}[n]$, for which some approximation is required.

The Euler equation (2.17) is thus given by

$$\mu = \frac{\delta E[n]}{\delta n(\mathbf{r})} = \frac{\delta T_s}{\delta n(\mathbf{r})} + V_{\rm eff}(\mathbf{r}), \tag{2.22}$$

where we have introduced the effective potential $V_{\rm eff}(\mathbf{r})$, defined as

$$V_{\rm eff}(\mathbf{r}) = V_{\rm ion}(\mathbf{r}) + \int \frac{n(\mathbf{r}')}{|\mathbf{r}-\mathbf{r}'|}\,d\mathbf{r}' + V_{\rm xc}(\mathbf{r}), \tag{2.23}$$

with the exchange-correlation potential

$$V_{\rm xc}(\mathbf{r}) = \frac{\delta E_{xc}[n]}{\delta n(\mathbf{r})}. \tag{2.24}$$

The Euler equation (2.22) with the constraint (2.18) is exactly the same equation that would be obtained from density functional theory when applied to a system of non-interacting electrons moving in the external potential $V_s(\mathbf{r}) = V_{\rm eff}(\mathbf{r})$. Therefore, for a given $V_{\rm eff}(\mathbf{r})$, the electron density $n(\mathbf{r})$ that satisfies (2.22) can be found simply by solving the N one-electron equations

$$-\nabla^2\psi_i(\mathbf{r}) + V_{\rm eff}(\mathbf{r})\psi_i(\mathbf{r}) = \varepsilon_i\psi_i(\mathbf{r}), \tag{2.25}$$

where the density is related to the wave function by,

$$n(\mathbf{r}) = \sum_{i=1}^{N} |\psi_i(\mathbf{r})|^2. \tag{2.26}$$

Since $V_{\text{eff}}(\mathbf{r})$ depends on $n(\mathbf{r})$, these equations must be solved self-consistently. The Kohn-Sham (KS) equations (2.23)-(2.26) reduce the problem of solving for a system of many interacting electrons to solving single-particle equations of Hartree form. In contrast to the Hartree-Fock approximation the effective potential is local, thus the computational effort is not significantly greater than that required within the Hartree approximation. In addition, the KS equations are exact, fully incorporating electron exchange and correlation effects. While in principle the KS-DFT method is exact, the exact form of E_{xc} is not known. Therefore the accuracy of any KS electronic structure calculation will be dependent on finding a satisfactory approximation for E_{xc}, a concern we will examine in the next section.

2.4 Local spin density approximation

The major limitation of DFT is that the functional E_{xc} is not known exactly, except in the case of a few simple model systems. Therefore some approximate functional is needed. The most successful and widely used approach is the local spin density approximation (LSDA), in which the exchange-correlation energy functional is written

$$E_{\text{xc}}^{\text{LSDA}}[n] = \int n(\mathbf{r})\varepsilon_{\text{xc}}[n_{\uparrow}(\mathbf{r}), n_{\downarrow}(\mathbf{r})]\, d\mathbf{r}, \tag{2.27}$$

where $\varepsilon_{\text{xc}}[n_{\uparrow}, n_{\downarrow}]$ is the exchange-correlation energy per particle of a homogenous, spin-polarised electron gas with spin-up and spin-down densities $n_{\uparrow}$ and $n_{\downarrow}$ respectively. The LSDA is formally valid in the limiting case of a slowly varying potential, however the LSDA has no formal justification in highly inhomogenous systems, such as atoms and bulk solids. Use of the LSDA in treatments of inhomogenous systems is principally justified by the remarkable accuracy of the numerical results obtained. In the calculations performed in this work, the Perdew-Wang form of the exchange-correlation functional is used [99].

Chapter 3

Scattering Theory

3.1 Introduction

This chapter details multiple scattering theory for a system of multiple scattering centres characterised by non-overlapping spatially bounded potentials. It is convenient to describe the scattering system as a collection of individual scattering potentials, and to describe the total system scattering matrix in terms of the scattering matrices of these individual potentials, these being the t-matrices detailed in the next section. Indeed in many cases it is necessary to treat the system in this way, e.g. periodic infinite solids. The Green function of a system contains all the physically relevant information about single site properties, and can be used directly to calculate such quantities, for example the charge density can be found from the imaginary part of the Green function. Calculating the total scattering matrix of the system allows us to solve for the Green function, and thus to calculate experimentally verifiable properties. In the next section we will examine single site scattering and the t-matrices. In the following sections we will examine multiple scattering theory in formal operator notation, then apply this to a system of muffin-tin (MT) potentials, these being spherically symmetric potentials bounded by non-overlapping spheres.

3.2 Single site scattering

Before we examine multiple scattering in extended systems, we need to consider the scattering from a single site. To determine this we need to solve the Schrödinger equation for the single site potential $v(\mathbf{r})$

$$\left(-\frac{1}{2}\nabla^2 + v(\mathbf{r})\right)\psi(\mathbf{r}) = E\psi(\mathbf{r}). \tag{3.1}$$

We restrict our discussion here to muffin-tin potentials, where the potential is spherically symmetric and $v(r) = 0$ for $r > R$, the muffin-tin radius. Expanding the wave function in partial waves

$$\psi(\mathbf{r}) = \sum_L c_L \psi_L(r) Y_L(\mathbf{r}), \tag{3.2}$$

we then need to find solutions of the radial Schrödinger equation

$$-\left[\frac{1}{2r^2}\frac{d}{dr}\left(r^2\frac{d}{dr}\right) - \frac{\ell(\ell+1)}{r^2}\right]\psi_L(r) + v(r)\psi_L(r) = E\psi_L(r). \tag{3.3}$$

The regular solution of equation (3.3) can be found by direct numerical integration, matching to the free space solution at the MT sphere radius, with the irregular solution found by inwards integration from the sphere boundary. The solutions are required to match smoothly up to the first derivative at the muffin-tin radius to the free space solutions

$$Z_\ell(r) \rightarrow m_\ell j_\ell(\kappa r) + h_\ell^{(1)}(\kappa r) \tag{3.4}$$

$$S_\ell(r) \rightarrow j_\ell(\kappa r), \tag{3.5}$$

where $m_\ell = t_\ell^{-1}$ is the inverse of the single site t-matrix, $j_\ell(\kappa r)$ is a spherical Bessel function, and $h_\ell^{(1)}(\kappa r)$ is a spherical Hankel function of the first kind. From the logarithmic derivative of the regular solution at the sphere boundary R

$$L_\ell(R) = \frac{Z_\ell'(R)}{Z_\ell(R)} = \frac{m_\ell j_\ell'(\kappa R) + h_\ell^{(1)'}(\kappa R)}{m_\ell j_\ell(\kappa R) + h_\ell^{(1)}(\kappa R)}, \tag{3.6}$$

we can then determine the inverse t-matrix

$$m_\ell = \frac{h_\ell^{(1)'}(\kappa R) - L_\ell(R) h_\ell^{(1)}(\kappa R)}{L_\ell(R) j_\ell(\kappa R) - j_\ell'(\kappa R)}. \tag{3.7}$$

The single site t-matrix describes the complete scattering from the site in question. These single site terms are then assembled within multiple scattering theory to describe scattering in extended systems. For more details on single site scattering, including scattering from general non-spherical potentials, see [46, 45].

3.3 Formal scattering

For an unperturbed system, with Hamiltonian H_0 and eigenstates $|\chi_\alpha\rangle$, the Schrödinger equation is

$$H_0|\chi_\alpha\rangle = E_\alpha|\chi_\alpha\rangle. \tag{3.8}$$

The scattered-wave solutions, $|\psi_\alpha\rangle$, of a perturbed system, with Hamiltonian $H = H_0 + V$,

$$H|\psi_\alpha\rangle = E_\alpha|\psi_\alpha\rangle \tag{3.9}$$

satisfy the Lippman-Schwinger equations [109]

$$|\psi_\alpha\rangle = |\chi_\alpha\rangle + G_0V|\psi_\alpha\rangle \tag{3.10}$$

$$= |\chi_\alpha\rangle + G_0T|\chi_\alpha\rangle, \tag{3.11}$$

where G_0 is the free particle Green function operator and T is the total scattering matrix operator of the system. T is related directly to V via a Dyson equation

$$T = V + VG_0T. \tag{3.12}$$

We can also introduce Dyson equations for the full Green function operator

$$G = G_0 + G_0VG \tag{3.13}$$

$$G = G_0 + G_0TG_0. \tag{3.14}$$

For a given system in which V is specified, T can in principle be solved directly from equation (3.12). However this method is impractical for many systems, especially those with an infinite number of scattering centres. A method which uses the individual t-matrix operators related to the scattering centres is more

useful in calculating T. Iterating equation (3.12) gives the series

$$T = V + VG_0V + VG_0VG_0V + \dots . \tag{3.15}$$

If we consider the potential as a sum of the individual non-overlapping cell potentials, $V = \sum_i V^i$, then equation (3.15) can be written as

$$T = \sum_i V^i + \sum_i V^i G_0 \sum_j V^j + \dots . \tag{3.16}$$

The single site t-matrix operator can be expressed in the form of (3.15), where the potential is that associated with a single site, as $t^i = V^i + V^iG_0V^i + V^iG_0V^iG_0V^i + \dots$. It then follows that the total T-matrix operator can be expressed in terms of these single site t-matrix operators as

$$T = \sum_i t^i + \sum_i \sum_{j\neq i} t^iG_0t^j + \sum_i \sum_{j\neq i} \sum_{k\neq i,j} t^iG_0t^jG_0t^k \dots . \tag{3.17}$$

With the interpretation of G_0 as a propagator, and of t^i as describing the interaction at site i, it is clear from equation (3.17) that no two consecutive scattering events occur at the same site, which is a necessary condition given that the t-matrix operator for a given potential characterises the complete scattering from that potential. Equation (3.17) shows that the T-matrix operator of an ensemble of scatterers may be viewed as being made up of sequences of scattering events, each sequence consisting of scattering at individual sites, coupled with free particle propagation between sites. Figure (3.1) shows some of the possible scattering paths that would contribute to T in a system with two scattering sites.

It follows from (3.17) that we can write T in the form

$$T = \sum_{i,j} T^{ij}, \tag{3.18}$$

where the site matrix elements T^{ij} are the sum of all scattering sequences which connect site i and site j. For non-overlapping potentials we can introduce the site off-diagonal elements, G_0^{ij}, of the free particle Green function, whereby the elements T^{ij} are then given by

$$T^{ij} = t^i\delta_{ij} + t^i \sum_{k\neq i} G_0^{ik}T^{kj}, \tag{3.19}$$

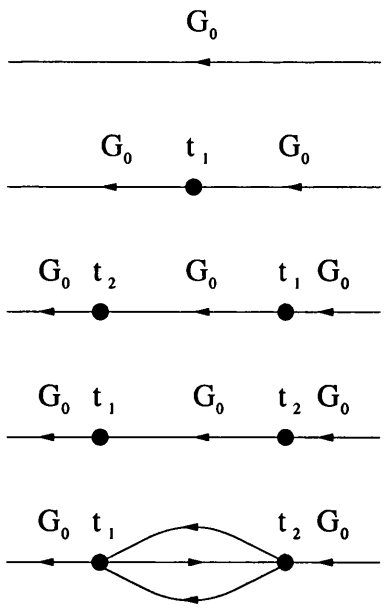

Figure 3.1: Some of the simplest scattering paths in a system with two scattering sites.

which can be easily verified by iteration. Equation (3.19) is known as the equation of motion in the literature [36].

3.4 Muffin-tin potentials

The equations of multiple scattering theory defined previously have been in abstract operator space. In this section we will derive equations suitable for computational purposes, within the muffin-tin approximation, that is spherically symmetric potentials bounded by non-overlapping spheres. The condition of spherical symmetry of the potential is helpful primarily in computation, but the geometric condition that the potentials be bounded by non-overlapping spheres considerably simplifies the expansion of the free particle Green function in angular momentum states. Most early work deriving and developing multiple scattering methods for electronic structure studies assumed this geometry. Only relatively recently has the validity of the resulting equations for more general potentials been demonstrated [47] [48] [133] [134] [88] [89] [44] [86].

In the coordinate representation we can write the Lippman-Schwinger equation

as [46]

$$\psi(\mathbf{r}) = \chi(\mathbf{r}) + \int G_0(\mathbf{r},\mathbf{r}')V(\mathbf{r}')\psi(\mathbf{r}')\,d\mathbf{r}' \tag{3.20}$$

$$= \chi(\mathbf{r}) + \iint G_0(\mathbf{r},\mathbf{r}')T(\mathbf{r}',\mathbf{r}'')\chi(\mathbf{r}'')\,d\mathbf{r}'\,d\mathbf{r}'', \tag{3.21}$$

and the T-matrix elements as

$$T^{ij}(\mathbf{r},\mathbf{r}') = t^i(\mathbf{r},\mathbf{r}')\delta_{ij} + \sum_{k\neq i}\int_{\Omega_i}\int_{\Omega_k} t^i(\mathbf{r},\mathbf{r}_1)G_0^{ik}(\mathbf{r}_1,\mathbf{r}_2)T^{kj}(\mathbf{r}_2,\mathbf{r}')\,d\mathbf{r}_1\,d\mathbf{r}_2 \tag{3.22}$$

where $G_0^{ik}(\mathbf{r}_1,\mathbf{r}_2)$ is the cell off-diagonal element of the free particle Green function, with the vectors $\mathbf{r}_1$ and $\mathbf{r}_2$ confined to cells i and k, respectively. A similar interpretation applies to the elements $T^{ij}(\mathbf{r},\mathbf{r}')$. These equations correspond to equations (3.10), (3.11) and (3.19) respectively. The philosophy of multiple scattering theory is evident on iteration of equation (3.22), showing the total scattering matrix to be made up by the scattering from individual cells, characterised by the cell t-matrices, with free propagation between the scattering cells via the free space Green function, $G_0^{ik}(\mathbf{r}_1,\mathbf{r}_2)$.

While intuitively useful, the coordinate representation is not ideal for computational purposes, due to the numerous integral equations. However, these recalcitrant integral equations can be transformed into matrix equations in the angular momentum representation. The matrices then have elements indexed via the $L = (\ell, m)$ of angular momentum eigenstates. The resulting matrix equations lend themselves more readily to computation. In this representation the on-the-energy-shell part of the T-matrix, that is the part connecting scattering events with the same energy, takes the form [127]

$$T_{LL'} = (-2i\kappa)\iint j_\ell(\kappa r)Y_L(\mathbf{r})T(\mathbf{r},\mathbf{r}')j_\ell(\kappa r')Y_L^*(\mathbf{r}')\,d\mathbf{r}\,d\mathbf{r}'. \tag{3.23}$$

We will now derive expansions of T and the Green function in the angular momentum representation. For muffin-tin potentials, the cell potentials are bounded by non-overlapping spheres. Therefore the vectors $\mathbf{r}_1$ and $\mathbf{r}_2$, measured from the centre of and confined to the cells 1 and 2, and the inter-cell vector $\mathbf{R}_{12}$ connecting the cell centres, as shown in figure (3.2), satisfy the following inequalities

$$|\mathbf{R}_{12}| > |\mathbf{r}_1|, \quad |\mathbf{R}_{12}| > |\mathbf{r}_2|, \quad \text{and} \quad |\mathbf{R}_{12}| > |\mathbf{r}_1 - \mathbf{r}_2|, \tag{3.24}$$

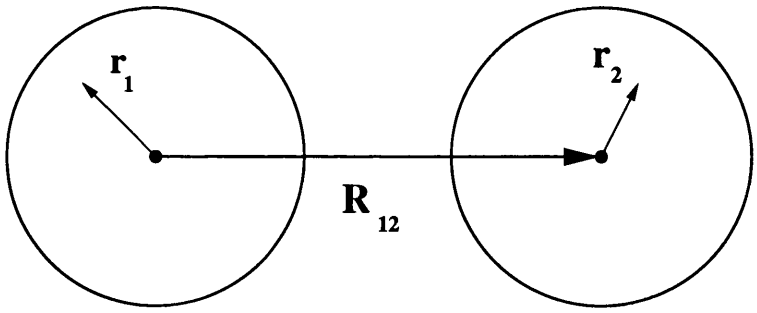

Figure 3.2: Diagram of two muffin-tin potential cells, showing intra-cell vectors $\mathbf{r}_1$ and $\mathbf{r}_2$, and the inter-cell vector $\mathbf{R}_{12}$.

$$|\mathbf{R}_{12} - \mathbf{r}_2| > |\mathbf{r}_1| \quad \text{and} \quad |\mathbf{R}_{12} + \mathbf{r}_1| > |\mathbf{r}_2|. \tag{3.25}$$

In this treatment we will use the familiar expansion of the free space Green function [46]

$$G_0(\mathbf{r}, \mathbf{r}') = G_0(\mathbf{r} - \mathbf{r}') = -2i\kappa \sum_L H_L(\mathbf{r}) J_L^*(\mathbf{r}'), \quad r > r', \tag{3.26}$$

where $J_L(\mathbf{r})$ and $H_L(\mathbf{r})$ are defined as

$$J_L(\mathbf{r}) = j_\ell(\kappa r) Y_L(\mathbf{r}), \tag{3.27}$$

$$H_L(\mathbf{r}) = h_\ell^{(1)}(\kappa r) Y_L(\mathbf{r}), \tag{3.28}$$

with complex conjugation of these functions taken to apply only to the spherical harmonic term, e.g., $J_L^*(\mathbf{r}) = j_\ell(\kappa r) Y_L^*(\mathbf{r})$.

In the muffin-tin case $\mathbf{r} - \mathbf{r}' = \mathbf{r}_1 - \mathbf{R}_{12} - \mathbf{r}_2$, and we can write the free particle propagator connecting different sites as

$$G_0^{12} = G_0(\mathbf{r}_1 - \mathbf{R}_{12} - \mathbf{r}_2) = -2i\kappa \sum_{LL'} J_L(\mathbf{r}_1) G_{LL'}(\mathbf{R}_{12}) J_{L'}^*(\mathbf{r}_2), \tag{3.29}$$

where we have used the expansion

$$H_L(\mathbf{r} - \mathbf{R}) = \sum_{L'} J_{L'}(\mathbf{r}) G_{L'L}(\mathbf{R}), \quad R > r, \tag{3.30}$$

with $G_{LL'}(\mathbf{R})$ given by

$$G_{LL'}(\mathbf{R}) = 4\pi \sum_{L''} i^{\ell - \ell' - \ell''} C_{L'L''}^L H_{L''}^*(\mathbf{R}). \tag{3.31}$$

For $\mathbf{R}$ a direct lattice vector, the $G_{LL'}(\mathbf{R})$ are the real space equivalents of the KKR structure constants introduced by Korringa [71] and by Kohn and Rostoker [69]. The expansion of the free particle Green function in (3.29) is dependent on the MT geometry, and is not necessarily valid for more general geometries, where the restrictions on $\mathbf{r}_1$, $\mathbf{r}_2$ and $\mathbf{R}_{12}$ are violated.

We now consider the expression for the full Green function of the system, the series equivalent of the operator equation (3.14)

$$G = G_0 + G_0 \sum_i t^i G_0 + G_0 \sum_i t^i G_0 \sum_{j \neq i} t^j G_0 + \ldots . \tag{3.32}$$

We will first examine the single scatterer term of equation (3.32), which we can write in the form [17],

$$\begin{aligned} G_0 t^i G_0 &= \iint G_0(\mathbf{r}-\mathbf{y}) t^i(\mathbf{y}-\mathbf{R}_i, \mathbf{z}-\mathbf{R}_i) G_0(\mathbf{z}-\mathbf{r}')\, d^3y\, d^3z \\ &= \iint G_0(\mathbf{r}-\mathbf{R}_i-\mathbf{y}') t^i(\mathbf{y}', \mathbf{z}') G_0(\mathbf{z}'+\mathbf{R}_i-\mathbf{r}')\, d^3y'\, d^3z', \end{aligned} \tag{3.33}$$

where $\mathbf{R}_i$ labels the vector to the centre of the cell (sphere) at site i, and

$$\mathbf{y}' = \mathbf{y} - \mathbf{R}_i \quad \text{and} \quad \mathbf{z}' = \mathbf{z} - \mathbf{R}_i. \tag{3.34}$$

If we consider the case where both of the arguments of the Green function fall outside of the bounding spheres, then $|\mathbf{r} - \mathbf{R}_i| > y'$ and $|\mathbf{r}' - \mathbf{R}_i| > z'$, and hence we can write

$$\begin{aligned} G_0 t^i G_0 = &\iint (-2i\kappa) \sum_L H_L(\mathbf{r}-\mathbf{R}_i) J^*_L(\mathbf{y}') t^i(\mathbf{y}', \mathbf{z}') \\ &\times (-2i\kappa) \sum_{L'} J_{L'}(\mathbf{z}') H^*_{L'}(\mathbf{r}'-\mathbf{R}_i)\, d^3y'\, d^3z' \\ = &-2i\kappa \sum_{LL'} H_L(\mathbf{r}-\mathbf{R}_i) t^i_{LL'} H^*_{L'}(\mathbf{r}'-\mathbf{R}_i) \end{aligned} \tag{3.35}$$

where $t^i_{LL'}$ is the single scatterer equivalent of equation (3.23). The two scatterer term in equation (3.32) can be treated in a similar manner, and can thus be written as

$$G_0 t^i G_0 t^j G_0 = -2i\kappa \sum_{LL_1} \sum_{L_2 L'} H_L(\mathbf{r}-\mathbf{R}_i) t^i_{LL_1} G_{L_1 L_2}(\mathbf{R}_{ij}) t^j_{L_2 L'} H^*_{L'}(\mathbf{r}'-\mathbf{R}_j). \tag{3.36}$$

Continuing with this process we can write an expression for the full Green function

$$G(\mathbf{r},\mathbf{r}') = G_0(\mathbf{r}-\mathbf{r}') - 2i\kappa \sum_{i,j} \sum_{LL'} H_L(\mathbf{r}-\mathbf{R}_i)\tau^{ij}_{LL'} H^*_{L'}(\mathbf{r}'-\mathbf{R}_j), \tag{3.37}$$

where $\mathbf{r}$ is in the interstitial region near cell i and $\mathbf{r}'$ in the interstitial region near cell j, and $i \neq j$. We have introduced here the scattering path operator (SPO) [49], which is a function of the energy E and is defined as

$$\tau^{ij}_{LL'} = t^i_{LL'}\delta_{ij} + \sum_{k\neq i} \sum_{L_1 L_2} t^i_{LL_1} G_{L_1 L_2}(\mathbf{R}_{ik}) \tau^{kj}_{L_2 L'} \tag{3.38}$$

and clearly satisfies the equation of motion, (3.19). Another useful form for the SPO, which can be obtained by repeated iteration and resummation and will be used later, is

$$\tau^{ij}_{LL'} = t^i_{LL'}\delta_{ij} + \sum_{k\neq i} \sum_{L_1 L_2} \tau^{ik}_{LL_1} G_{L_1 L_2}(\mathbf{R}_{kj}) t^j_{L_2 L'}. \tag{3.39}$$

3.5 Full Green function

The one-electron Green function is a highly useful quantity, since it allows the calculation of most properties of interest for a given system, e.g., the charge density. Therefore we require an expression from which it can conveniently be calculated within the angular momentum representation. Taking the arguments of $G(\mathbf{r},\mathbf{r}')$ to lie outside the bounding spheres but within the cell at the origin, we can write equation (3.37) in the form [17]

$$\begin{aligned} G(\mathbf{r},\mathbf{r}') =& G_0(\mathbf{r},\mathbf{r}') - 2i\kappa \sum_{LL'} H_L(\mathbf{r}) \tau^{00}_{LL'} H^*_{L'}(\mathbf{r}') \\ & - 2i\kappa \sum_{j\neq 0} \sum_{LL'L''} H_L(\mathbf{r}) \tau^{0j}_{LL'} G_{L'L''}(\mathbf{R}_j) J^*_{L''}(\mathbf{r}') \\ & - 2i\kappa \sum_{i\neq 0} \sum_{LL'L''} J_L(\mathbf{r}) G_{LL'}(\mathbf{R}_i) \tau^{i0}_{L'L''} H^*_{L''}(\mathbf{r}') \\ & - 2i\kappa \sum_{i\neq 0} \sum_{j\neq 0} \sum_{LL'L''L'''} J_L(\mathbf{r}) G_{LL'}(\mathbf{R}_i) \tau^{ij}_{L'L''} G_{L''L'''}(\mathbf{R}_j) J^*_{L'''}(\mathbf{r}'). \end{aligned} \tag{3.40}$$

Using an undertilde to denote matrices in angular momentum space, we use the expressions

$$\underset{\sim}{\tau}^{00} = \underset{\sim}{t}^{0} + \underset{\sim}{t}^{0} \sum_{i \neq 0} \underset{\sim}{G}^{0i} \underset{\sim}{\tau}^{i0} \tag{3.41}$$

and

$$\underset{\sim}{\tau}^{00} = \underset{\sim}{t}^{0} + \sum_{j \neq 0} \underset{\sim}{\tau}^{0j} \underset{\sim}{G}^{j0} \underset{\sim}{t}^{0}, \tag{3.42}$$

which together imply that

$$\sum_{i \neq 0} \underset{\sim}{G}(\mathbf{R}_i) \underset{\sim}{\tau}^{i0} = \underset{\sim\sim}{m}^{0} \underset{\sim}{\tau}^{00} - 1, \tag{3.43}$$

$$\sum_{j \neq 0} \underset{\sim}{\tau}^{0j} \underset{\sim}{G}(\mathbf{R}_j) = \underset{\sim}{\tau}^{00} \underset{\sim\sim}{m}^{0} - 1, \tag{3.44}$$

and

$$\sum_{i \neq 0} \sum_{j \neq 0} \underset{\sim}{G}(\mathbf{R}_i) \underset{\sim}{\tau}^{ij} \underset{\sim}{G}(\mathbf{R}_j) = \underset{\sim\sim}{m}^{0} \underset{\sim}{\tau}^{00} \underset{\sim\sim}{m}^{0} - \underset{\sim\sim}{m}^{0}, \tag{3.45}$$

which allow us to write equation (3.40) as

$$\begin{aligned} G(\mathbf{r}, \mathbf{r}') = &- 2i\kappa \sum_{LL'} \left[J_L(\mathbf{r}) m^0_L + H_L(\mathbf{r}) \right] \tau^{00}_{LL'} \left[m^0_{L'} J^*_{L'}(\mathbf{r}') + H^*_{L'}(\mathbf{r}') \right] \\ &+ 2i\kappa \sum_{L} \left[J_L(\mathbf{r}) m^0_L + H_L(\mathbf{r}) \right] J^*_L(\mathbf{r}') \end{aligned} \tag{3.46}$$

where we have chosen $\mathbf{r}' > \mathbf{r}$ and used the expansion of the free space Green function in equation (3.26). Since the Green function is continuous with respect to both of its arguments, and solves the Schrödinger equation as a function of $\mathbf{r}$ and $\mathbf{r}'$ for $\mathbf{r} \neq \mathbf{r}'$, we can extend this expression, valid in the region of the cell at the origin beyond the MT sphere where $v = 0$, into the MT sphere itself as

$$G(\mathbf{r}, \mathbf{r}') = -2i\kappa \left[\sum_{L} Z^0_L(\mathbf{r}) S^{0\,*}_L(\mathbf{r}') + \sum_{LL'} Z^0_L(\mathbf{r}) \tau^{00}_{LL'} Z^{0\,*}_{L'}(\mathbf{r}') \right], \tag{3.47}$$

where the functions $Z^0_\ell(\mathbf{r})$ and $S^0_\ell(\mathbf{r})$ are the regular and irregular solutions of the Schrödinger equation for the MT potential at the origin, that at the MT sphere

radius match smoothly onto the functions

$$Z_\ell^0(r) \rightarrow m_\ell^0 j_\ell(\kappa r) + h_\ell^{(1)}(\kappa r) \tag{3.48}$$

$$S_\ell^0(r) \rightarrow j_\ell(\kappa r). \tag{3.49}$$

Note that these functions are the regular and irregular solutions to the single potential Schrödinger equation detailed in section 3.2.

Hence for $\mathbf{r}' > \mathbf{r}$ and both vectors inside cell α, we have

$$\begin{aligned} G(\mathbf{r},\mathbf{r}') = &-2i\kappa \sum_L Y_L(\mathbf{r}_\alpha) Z_\ell^\alpha(r_\alpha) S_\ell^\alpha(r'_\alpha) Y_L^*(\mathbf{r}'_\alpha) \\ &-2i\kappa \sum_{LL'} Y_L(\mathbf{r}_\alpha) Z_\ell^\alpha(r_\alpha) \tau_{LL'}^{\alpha\alpha} Z_{\ell'}^\alpha(r'_\alpha) Y_{L'}^*(\mathbf{r}'_\alpha). \end{aligned} \tag{3.50}$$

The first term in (3.50) is the single scattering centre expression (since $\tau = 0$ for a single scatterer). Once $G(\mathbf{r},\mathbf{r}')$ has been calculated all the single site properties of the system, such as the charge density, can readily be found. The determination of the Green function is now reduced to the evaluation of the site diagonal elements of the τ-matrix, although, as will be shown later, in order to determine the τ-matrix of a defect system it is necessary to also calculate the site off-diagonal elements of the τ-matrix.

3.6 General potentials

For many systems the MT approximation gives adequate results, specifically those with a close packed crystal structure such as FCC, HCP and BCC bulk crystals [87]. However when we consider more open systems, or systems with reduced symmetry such as surfaces, interfaces and other defects, it is desirable to go beyond the MT approximation, and treat the system as non-overlapping space-filling potential cells.

Restricting the potentials to the MT form allows us to derive the MST equations in the relatively simple and intuitive manner of the previous section. The MT approximation places two restrictions on the form of the potentials, first that the potentials are bounded by non-overlapping spheres, and second that the potentials are spherically symmetric. The second restriction, that of spherical

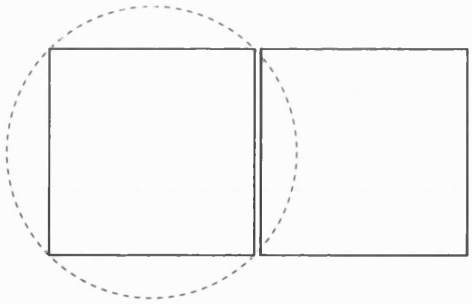

Figure 3.3: Adjacent space-filling cells, with the bounding sphere of one cell shown overlapping the other cell.

symmetry, has little effect on the preceding derivations. The cell t-matrices will no longer be diagonal with respect to angular momentum and the single cell scattering problem becomes more computationally demanding to solve, but the logic of the derivation and the form of the τ-matrix are essentially unchanged.

The second restriction, that of the confinement of the cell potentials to non-overlapping bounding spheres, is more significant. This *geometric* restriction allows use of the expansion (3.29) for the free particle Green function, in a system of space-filling cells this expansion is no longer possible and thus it is not evident that the MT form for τ is valid. In addition to this mathematical difficulty, physical arguments have also been made that question the validity of the MT form for τ in the case of space-filling cells.

If we consider the two adjacent space-filling potential cells shown in figure (3.3), it is clear that the bounding sphere for one potential overlaps with that of the adjacent potentials. This suggests that the spherical wave emanating from the centre of one cell would begin scattering from an adjacent cell before the scattering inside the original cell was completed. It was claimed [33] that this implied that the scattering from adjacent cells was coupled in some complicated fashion, which prevented the scattering from being described simply in terms of the cell t-matrices. In order to take this coupling into account it was thought necessary to include the so-called 'near-field corrections' (NFCs) in applications of MST to space-filling cell potentials.

There was considerable interest in determining whether NFCs exist, and if so in calculating them [33]. Fortunately it was found that NFCs do not exist [44][47][48], and this has since been confirmed by computational studies [34] [35].

From a physical perspective, this is an encouraging result, since one would like the solution of a problem to be independent of the manner in which space is partitioned.

Therefore while the MT form of the potentials constitutes a *sufficient* condition for the validity of MST, it turns out that it is not a necessary condition. The MT form of the τ-matrix is therefore valid in the case of non-overlapping space-filling cell potentials.

3.7 Calculation of the τ-matrix

From equation (3.38), using an undertilde to denote matrices in angular momentum space, the τ-matrix is given by

$$\underset{\sim}{\tau}^{nm} = \underset{\sim}{t}^{n}\delta_{nm} + \underset{\sim}{t}^{n} \sum_{p \neq n} \underset{\sim}{G}(\mathbf{R}_{np})\underset{\sim}{\tau}^{pm}. \tag{3.51}$$

We can introduce a supermatrix notation, whereby the matrix elements correspond to site indices with each element a matrix in angular momentum,

$$[\mathbf{t}]_{nm} = \delta_{nm}\underset{\sim}{t}^{n} \tag{3.52}$$

$$[\boldsymbol{\tau}]_{nm} = \underset{\sim}{\tau}^{nm} \tag{3.53}$$

$$[\mathbf{G}]_{nm} = (1 - \delta_{nm})\underset{\sim}{G}(\mathbf{R}_{nm}) \tag{3.54}$$

In this notation (3.51) becomes

$$\boldsymbol{\tau} = \mathbf{t} + \mathbf{t}\mathbf{G}\boldsymbol{\tau}, \tag{3.55}$$

using $\mathbf{m} = \mathbf{t}^{-1}$, we have a formal solution for the τ-matrix

$$\underset{\sim}{\tau}^{nm} = \left[(\mathbf{m} - \mathbf{G})^{-1}\right]_{nm}. \tag{3.56}$$

Both m and G are functions of the energy E, but m depends solely on the potential of a cell, while G is dependent only on the structure of the lattice. Thus (3.56) reflects the separation of the potential and structural aspects of the system.

Equation (3.56) represents the solution in real space for the scattering path operator. However the matrix which requires inversion has dimensions of $N(\ell_{\max}+1)^2$ by $N(\ell_{\max}+1)^2$, where N is the number of sites in the system. Clearly this becomes impractical for systems other than small clusters of atoms. Indeed for infinite systems (3.56) is a formal statement as the matrix to be inverted has infinite dimensions.

3.8 Periodicity

For periodic systems we can use lattice Fourier transforms to shift the problem into reciprocal space. The site dimensions of the matrix to be inverted are then restricted to the number of sites within the unit cell. This allows us to solve for the $\mathbf{K}$ resolved τ-matrix, which is related to the real space τ-matrix by an integral over the Brillouin zone of the unit cell.

If we have a system with periodicity in one, two or three dimensions, we can derive a $\mathbf{K}$ resolved τ-matrix for the periodic system. Omitting the angular momentum indices for clarity, we first multiply (3.51) by $e^{i\mathbf{K}\cdot(\mathbf{R}_n-\mathbf{R}_m)}$, where $\mathbf{K}$ is used to represent the appropriate reciprocal space variable for one (k), two ($\mathbf{k}_\parallel$) or three ($\mathbf{K}$) dimensions,

$$\underset{\sim}{\tau}^{nm}e^{i\mathbf{K}\cdot(\mathbf{R}_n-\mathbf{R}_m)} = \underset{\sim}{t}^{n}\delta_{nm}e^{i\mathbf{K}\cdot(\mathbf{R}_n-\mathbf{R}_m)} + \sum_{p\neq n}\underset{\sim}{G}^{np}\underset{\sim}{\tau}^{pm}e^{i\mathbf{K}\cdot(\mathbf{R}_n-\mathbf{R}_m)} \tag{3.57}$$

$$= \underset{\sim}{t}^{n}\delta_{nm}e^{i\mathbf{K}\cdot(\mathbf{R}_n-\mathbf{R}_m)} + \sum_{p\neq n}\underset{\sim}{G}^{np}e^{i\mathbf{K}\cdot(\mathbf{R}_n-\mathbf{R}_p)}\underset{\sim}{\tau}^{pm}e^{i\mathbf{K}\cdot(\mathbf{R}_p-\mathbf{R}_m)}. \tag{3.58}$$

If we sum the terms in this expression over n and m, where the sums over sites are restricted to the dimensions in which the system is periodic, and N is the

total number of sites, we have terms which exhibit only $\mathbf{K}$ dependence

$$\sum_{nm} \underset{\sim}{t}^{n} \delta_{nm} e^{i\mathbf{K}\cdot(\mathbf{R}_n - \mathbf{R}_m)} = N\underset{\sim}{t} \tag{3.59}$$

$$\sum_{nm} \underset{\sim}{\tau}^{nm} e^{i\mathbf{K}\cdot(\mathbf{R}_n - \mathbf{R}_m)} = \sum_{n'0} \underset{\sim}{\tau}^{n'0} e^{i\mathbf{K}\cdot\mathbf{R}_{n'}} = N\underset{\sim}{\tau}(\mathbf{K}) \tag{3.60}$$

$$\sum_{n,p\neq n} \underset{\sim}{G}^{np} e^{i\mathbf{K}\cdot(\mathbf{R}_n - \mathbf{R}_p)} = \sum_{n'} \underset{\sim}{G}^{n'0} e^{i\mathbf{K}\cdot\mathbf{R}_{n'}} (1 - \delta_{n'0}) \tag{3.61}$$

$$= N\underset{\sim}{G}(\mathbf{K}) \tag{3.62}$$

$$\sum_{nm,p\neq n} G^{np} e^{i\mathbf{K}\cdot(\mathbf{R}_n - \mathbf{R}_p)} \tau^{pm} e^{i\mathbf{K}\cdot(\mathbf{R}_p - \mathbf{R}_m)} = \sum_{n'm'} (1 - \delta_{n'0}) G^{n'0} e^{i\mathbf{K}\cdot\mathbf{R}_{n'}} \tau^{0m'} e^{-i\mathbf{K}\cdot\mathbf{R}_{m'}} \tag{3.63}$$

$$= G(\mathbf{K})\tau(\mathbf{K}) \tag{3.64}$$

Hence we have the $\mathbf{K}$ resolved EOM, analogous to (3.38)

$$\tau(\mathbf{K}) = t + tG(\mathbf{K})\tau(\mathbf{K}), \tag{3.65}$$

in terms of the $\mathbf{K}$ resolved quantities

$$\tau(\mathbf{K}) = \frac{1}{N} \sum_{n,m} e^{i\mathbf{K}\cdot(\mathbf{R}_n - \mathbf{R}_m)} \underset{\sim}{\tau}^{nm}, \tag{3.66}$$

$$G(\mathbf{K}) = \frac{1}{N} \sum_{n,m} e^{i\mathbf{K}\cdot(\mathbf{R}_n - \mathbf{R}_m)} \underset{\sim}{G}(\mathbf{R}_{nm})(1 - \delta_{nm}). \tag{3.67}$$

The form of $\tau(\mathbf{K})$ is that of a complex Fourier series, and hence we can write

$$\underset{\sim}{\tau}^{nm} = \frac{1}{\Omega_{BZ}} \int_{BZ} d\mathbf{K}\, e^{-i\mathbf{K}\cdot(\mathbf{R}_n - \mathbf{R}_m)} \tau(\mathbf{K}), \tag{3.68}$$

where the integral is over the dimensions of the Brillouin zone (BZ) consistent with the periodicity, with Ω_{BZ} its volume/area/length in 3/2/1 dimensions. These expressions are valid for those systems with one site per unit cell. For complex lattices we can introduce a new notation whereby the sites are labelled by Nn, with N labelling the unit cell and n the site within it, in which case

$$\tau^{nm}(\mathbf{K}) = \frac{1}{N} \sum_{N,M} e^{i\mathbf{K}\cdot(\mathbf{R}_N - \mathbf{R}_M)} \underset{\sim}{\tau}^{NnMm}, \tag{3.69}$$

$$\underset{\sim}{\tau}^{NnMm} = \frac{1}{\Omega_{BZ}} \int_{BZ} d\mathbf{K}\, e^{-i\mathbf{K}\cdot(\mathbf{R}_N - \mathbf{R}_M)} \tau^{nm}(\mathbf{K}), \tag{3.70}$$

and

$$G^{nm}(\mathbf{K}) = \frac{1}{N}\sum_{N,M} e^{i\mathbf{K}\cdot(\mathbf{R}_N-\mathbf{R}_M)}\underset{\sim}{G}(\mathbf{R}_{NnMm})(1-\delta_{NM}\delta_{nm}). \tag{3.71}$$

We can then obtain from (3.65), in the same manner as for (3.56), the solution

$$\underset{\sim}{\tau}^{nm}(\mathbf{K}) = \left[(\mathbf{m}-\mathbf{G}(\mathbf{K}))^{-1}\right]_{nm}. \tag{3.72}$$

The $G(\mathbf{K})$ were introduced by Korringa [71] and by Kohn and Rostoker [69] and are commonly known as the KKR structure constants. Equation (3.72) also exhibits the separation of potential and structure seen in (3.65), with $G(\mathbf{K})$ only depending on the structure of the lattice. This separation was seen as of great benefit in early calculations, since the $G(\mathbf{K})$ could be calculated once for any given lattice and stored, with only the relatively inexpensive calculation of the t-matrix needed for each iteration (for example, see [50]). As computing power has increased, this is no longer as significant, however the separation is made use of in the defect calculations detailed in later sections. In these defect calculations the τ-matrices for a substrate system are calculated and stored, then used in each iteration to find the τ-matrices for the defect system, a procedure analogous to the erstwhile practice of storing the structure constants.

Equation (3.72) represents the complete solution for the τ-matrix in a system with three-dimensional periodicity. The site indices in the matrix inversion are now restricted to sites within a single unit cell, thus we are able to solve for the τ-matrix.

For extended systems with one or two-dimensional periodicity however, we still have a unit cell which is infinite in extent. Since each site in the unit cell is unique, the unit cell index in equation (3.72) is infinite, and we again have the obstacle of an infinite matrix to invert.

The Layer-KKR method, used in this thesis for calculation of the substrate τ-matrices, allows for calculation of systems with two-dimensional periodicity, such as surfaces and interfaces. The LKKR method involves partitioning the system into layers with two-dimensional symmetry, for which the scattering can be solved, and treating the scattering between layers within a plane wave basis set. The layers of interest are then considered as being embedded between two semi-infinite half-spaces. This method will be covered in more detail in the next

section. The τ-matrices calculated using the LKKR method are stored, and used as the substrate τ-matrices for the one-dimensional defect calculations, which are detailed in section 3.13.

The LKKR method is by no means the only KKR method by which extended systems that lack full three-dimensional periodicity can be treated. As mentioned in chapter 1, supercells are one technique for treating surfaces. In a supercell calculation the surface/interface is contained within a large unit cell (the supercell) which is repeated periodically.

One recent development is the screened KKR method [135]. In this method a reference system is used such that the KKR structure constants decay exponentially. A constant repulsive potential within the muffin-tin spheres is one possibility for such a reference system – since there are no eigensolutions of the Schrödinger equation for negative energies, the structure constants decay exponentially for energies sufficiently below the top of the repulsive wells. This allows the KKR method to be transformed into a tight binding form with only short range interactions between atoms, without loss of accuracy.

3.9 Embedded layer τ

As described in the previous section, special treatment is required in extended systems with two-dimensional translational periodicity, in order to calculate the matrix elements of the τ-matrix. For such systems, we can consider them to be made up of parallel atomic planes, with the plane passing through the centre of the atoms assigned to it. A layer is made up of one or more atomic planes, assembled as is convenient. The scattering properties of a single layer may be determined from a 2D Fourier transform of the equation of motion (3.72), analogous to calculating the bulk scattering matrix in standard 3D KKR theory. The scattering due to a single layer i is thus given by

$$\underset{\sim}{T}_i(\mathbf{k}_\parallel) = \left[\underset{\sim}{m}_i - \underset{\sim}{G}_i(\mathbf{k}_\parallel)\right]^{-1}. \tag{3.73}$$

where $\mathbf{k}_\parallel$ is the 2D wave vector parallel to the layer, $\underset{\sim}{m}_i$ is the matrix of inverse t-matrices of the atoms within the unit cell of layer i, and $\underset{\sim}{G}_i(\mathbf{k}_\parallel)$ is given by (3.71).

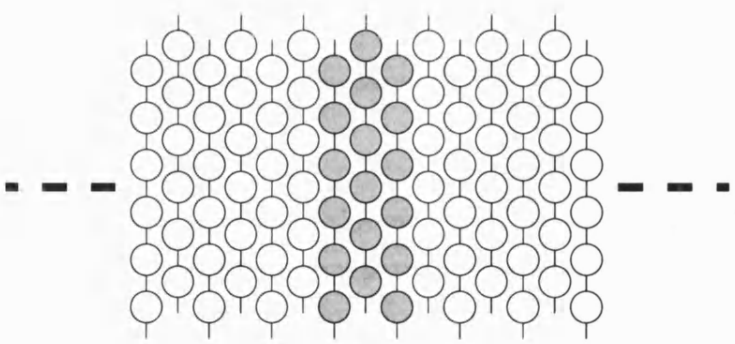

Figure 3.4: Diagram of the embedded layer problem. The shaded central layers are those treated self-consistently, while the unshaded layers represent the semi-infinite left and right half-spaces.

The matrix elements $\underset{\sim}{G}_i(\mathbf{k}_\parallel)$ are known as the 2D KKR structure constants, details of whose calculation can be found in [63], [64], [65], [66] and [97].

The embedded layer problem concerns the scattering from a layer sandwiched between two semi-infinite half-spaces, as shown in figure (3.4). The scattering properties of the half-spaces are referred to as reflectivities, as they determine the reflected wave due to the scattering from an incident wave. The calculation of the half-space reflectivities will be detailed in the next section, for the moment we will assume that they can be found. The operators in the expressions that follow have an implicit $\mathbf{k}_\parallel$ dependence which we omit for clarity. We can write the full transition matrix for a scattering series in which the first scattering event is in layer i as

$$T = \tau_L + \tau_i + \tau_R \tag{3.74}$$

where τ_i sums those paths which end with a scattering event within layer i and $\tau_L(\tau_R)$ sums those paths which end with a scattering event in the left (right) half-space. This expression is clearly valid as it accounts for all possible scattering paths. We can write the EOM for the new scattering path operators as

$$\begin{aligned} \tau_L &= \left[1 + \tau_i g + \tau_R g\right] T_L^{i-1} \\ \tau_i &= \left[\tau_L g + 1 + \tau_R g\right] T_i \\ \tau_R &= \left[\tau_L g + \tau_i g + 1\right] T_R^{i+1} \end{aligned} \tag{3.75}$$

where all propagators are denoted by g for clarity, their precise forms being determined by the quantities on either side of them. The quantities T_L^{i-1} and T_R^{i+1} are the half-space reflectivities, mentioned above. The first equation in

(3.75) is a mathematical formulation of the statement that the paths which end with a scattering event in the left half-space comprise those that are solely within the left half-space, as well as those which scatter there from layer i or the right half-space. These expressions can be manipulated to give

$$\begin{aligned} \tau_L &= (1 + T_L^i g) T_R^{i+1} (1 - g T_L^i g T_R^{i+1})^{-1}, \\ \tau_R &= (1 + T_R^i g) T_L^{i-1} (1 - g T_R^i g T_L^{i-1})^{-1}, \end{aligned} \tag{3.76}$$

where the scattering operators T_L^i and T_R^i represent the combined scattering of the isolated layer i and the respective half-space, and are given by

$$\begin{aligned} T_L^i &= T_i + (1 + T_i g) T_L^{i-1} (1 - g T_i g T_L^{i-1})^{-1} (1 + g T_i), \\ T_R^i &= T_i + (1 + T_i g) T_R^{i+1} (1 - g T_i g T_R^{i+1})^{-1} (1 + g T_i). \end{aligned} \tag{3.77}$$

Combining equations (3.75) and (3.76), we can write an expression for τ_i

$$\tau_i = T_i + T_i g R_i^{\text{eff}} g T_i, \tag{3.78}$$

where R_i^{eff}, the effective reflectivity of the solid excluding layer i is given by

$$\begin{aligned} R_i^{\text{eff}} = &\left[1 + (1 - T_R^{i+1} g T_i g)^{-1} T_R^{i+1} g (1 + T_i g)\right] \\ &\times T_L^{i-1} (1 - g T_R^i g T_L^{i-1})^{-1} \\ &+ \left[1 + (1 - T_L^{i-1} g T_i g)^{-1} T_L^{i-1} g (1 + T_i g)\right] \\ &\times T_R^{i+1} (1 - g T_L^i g T_R^{i+1})^{-1}. \end{aligned} \tag{3.79}$$

Since the scattering series was required to start in layer i, τ_i connects sites that are both within the embedded layer i. Therefore the site diagonal elements of the SPO, appearing in the expression for the full Green function (3.50) where α denotes a scattering centre in layer i, are given by

$$\tau^{\alpha\alpha} = \left[T_i + T_i g R_i^{\text{eff}} g T_i\right]^{\alpha\alpha}. \tag{3.80}$$

3.10 Half-space reflectivities

We will now turn to the calculation of the half-space reflectivities, leading to the evaluation of the effective reflectivity. As shown above, the scattering for a single layer in isolation is given by equation (3.73). In principle we can determine the scattering for a system comprising a number of layers via the subspace equation of motion [19], this being a modification of equation (3.51) where the single site t-matrices are replaced by single layer SPO's and the propagators become inter-layer terms. For an increasingly large slab of identical layers one would expect the reflection scattering properties to converge due to attenuation present when the energy has a finite imaginary damping component.

The principal drawback of this method is that the dimension of the full scattering matrix is related to the number of layers included in the slab. Thus attempting to construct the scattering for a half-space entirely within the angular momentum basis is impractical, since the matrices involved will become unfeasibly large. This difficulty is circumvented by coupling the scattering between layers within a plane wave basis set [97], using the plane wave basis vectors

$$\exp(i\mathbf{K}_{\mathbf{g}}^{\pm} \cdot \mathbf{r}), \tag{3.81}$$

where

$$\mathbf{K}_{\mathbf{g}}^{\pm} = \begin{cases} \mathbf{k}_{\parallel} + \mathbf{g} \pm \sqrt{2E - |\mathbf{k}_{\parallel} + \mathbf{g}|^2}\,\hat{\mathbf{z}}, & 2E > |\mathbf{k}_{\parallel} + \mathbf{g}|^2 \\ \mathbf{k}_{\parallel} + \mathbf{g} \pm i\sqrt{|\mathbf{k}_{\parallel} + \mathbf{g}|^2 - 2E}\,\hat{\mathbf{z}}, & 2E < |\mathbf{k}_{\parallel} + \mathbf{g}|^2, \end{cases} \tag{3.82}$$

with the $\pm$ indicating the direction of propagation in the z-axis. As more basis vectors are included, $|\mathbf{g}|$ increases, thus $\mathbf{K}_{\mathbf{g}z}$ acquires an increasing imaginary component, which means that the amplitude of the basis vector at the next layer becomes less significant. This allows truncation of the plane wave basis set after a relatively low number of vectors, typically $10-30$, depending on the separation of the layers. Within the plane wave basis one can define four scattering operators representing reflection from or transmission through either side of layer i, as

$$\begin{aligned} T_i^{-+} &= \Gamma_{gL}^{-} T_i \Gamma_{Lg}^{+} \quad , \quad T_i^{++} = 1 + \Gamma_{gL}^{+} T_i \Gamma_{Lg}^{+}, \\ T_i^{+-} &= \Gamma_{gL}^{+} T_i \Gamma_{Lg}^{-} \quad , \quad T_i^{--} = 1 + \Gamma_{gL}^{-} T_i \Gamma_{Lg}^{-}. \end{aligned} \tag{3.83}$$

Here $\Gamma_{gL}^{\pm}$ converts from the plane wave to the partial wave basis, and $\Gamma_{Lg}^{\pm}$ converts

back into plane waves,

$$\begin{aligned}\left[\Gamma^{\pm}_{igL}\right]_{\mathbf{g}L} &= 4\pi i^{\ell} e^{i\mathbf{K}^{\pm}_{\mathbf{g}}\cdot\mathbf{R}_i} Y^{*}_{L}(\mathbf{K}^{\pm}_{\mathbf{g}}),\\ \left[\Gamma^{\pm}_{iLg}\right]_{L\mathbf{g}} &= \frac{2\pi i^{-\ell}}{\kappa A(\mathbf{K}^{+}_{\mathbf{g}})_z} e^{-i\mathbf{K}^{\pm}_{\mathbf{g}}\cdot\mathbf{R}_i} Y_{L}(\mathbf{K}^{\pm}_{\mathbf{g}}).\end{aligned} \tag{3.84}$$

In terms of these matrices, we can write the scattering for a composite system of layers $1+2$ as

$$\begin{aligned}T^{++}_{1,2} &= T^{++}_{1}(1 - P^{+}_{1}T^{+-}_{2}P^{-}_{1}T^{-+}_{1})^{-1}P^{+}_{1}T^{++}_{2},\\ T^{--}_{1,2} &= T^{--}_{2}(1 - P^{-}_{1}T^{-+}_{-}P^{+}_{1}T^{+-}_{2})^{-1}P^{-}_{1}T^{--}_{1},\\ T^{+-}_{1,2} &= T^{+-}_{1} + T^{++}_{1}P^{+}_{1}T^{+-}_{2}(1 - P^{-}_{1}T^{-+}_{1}P^{+}_{1}T^{+-}_{2})^{-1}P^{-}_{1}T^{--}_{1},\\ T^{-+}_{1,2} &= T^{-+}_{2} + T^{--}_{2}P^{-}_{1}T^{-+}_{1}(1 - P^{+}_{1}T^{+-}_{2}P^{-}_{1}T^{-+}_{1})^{-1}P^{+}_{1}T^{++}_{2},\end{aligned} \tag{3.85}$$

where the propagators which shift the origin of the expansion from $\mathbf{c}_i$ to $\mathbf{c}_{i+1}$ and vice versa, denoted by $P^{\pm}_{i}$, are simply the plane wave matrix elements of the Bloch Green function

$$P^{\pm}_{i\mathbf{g}\mathbf{g}'} = \delta_{\mathbf{g}\mathbf{g}'} e^{i\mathbf{K}^{\pm}_{\mathbf{g}}\cdot(\mathbf{c}_{i+1}-\mathbf{c}_i)}, \tag{3.86}$$

so that the reflection matrices $T^{\pm\mp}$ have a single origin, while the transmission matrices $T^{\pm\pm}$ have two origins, as can be seen in figure (3.5) which shows the reflection and transmission matrices for the single layer and composite systems.

The plane wave propagator is diagonal, which has important consequences. If this procedure were to be implemented entirely within the angular momentum basis, the propagators introduced to shift the origins of the expansions would no longer be diagonal. Repeated use of (3.85) would introduce products of these propagators, leading to inconvenient internal summations. The convergence problems associated with these summations are avoided by using the plane wave basis set.

Repeated use of (3.85) allows the full solid to be assembled by adding a single layer at a time. In calculating the scattering from a semi-infinite half-space, this stacking can be accelerated using layer doubling. Since the layers to be stacked are all identical, then the scattering from 2 layers can be coupled with itself, to give the scattering from 4 layers, which is then coupled with itself to give the scattering for eight layers. Recursive application of this algorithm stacks 2^n layers, as opposed to n layers obtained by stacking individually. At real energies

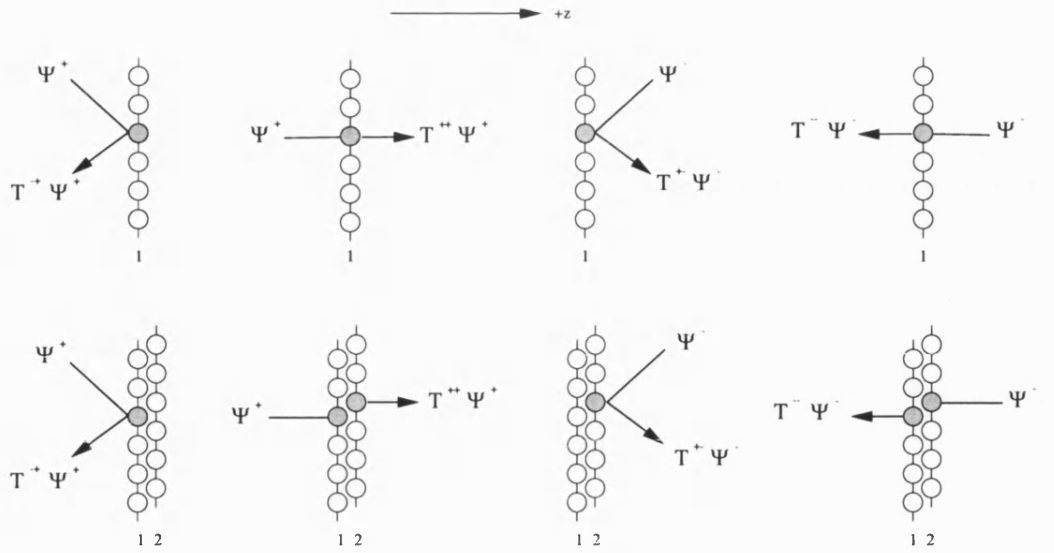

Figure 3.5: Illustration of the layer transmission and reflection matrices of equation (3.83) for a single layer, and equation (3.85) for the composite scattering system of layers 1+2. In all cases the origins of the expansions of the incident and scattered plane wave are indicated by the shaded circle.

this process is not guaranteed to converge, therefore it is necessary to include a small imaginary component into the energy, ensuring that all states decay within a finite length, and thus that the half-space reflection matrices converge after stacking a finite number of layers.

Recalling the problem of calculating the reflectivity, if $T_{i,j}^{\pm\pm}$ represents the scattering matrix for the stack of layers i to j, the the reflectivities of the left and right half-spaces, appearing in (3.79), are given by

$$T_L^i = T_{-\infty,i}^{-+} \quad T_R^i = T_{i,\infty}^{+-}, \tag{3.87}$$

where $\pm\infty$ is in practice the number of layers needed to converge the quantities to machine accuracy on the computer. This completes the derivation of the half-space reflectivities, for more details of the LKKR method see [19] [83].

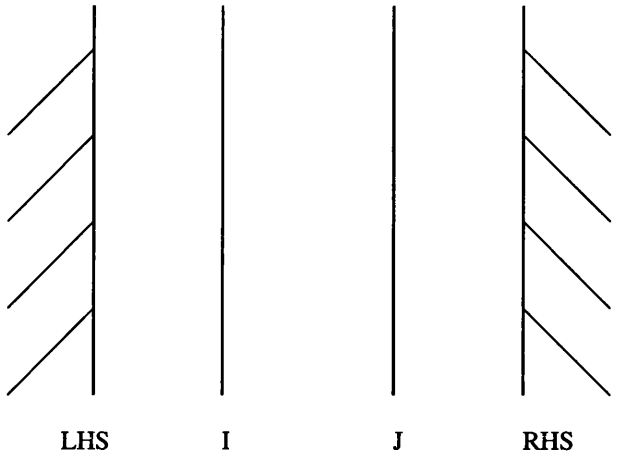

Figure 3.6: System comprising 2 layers I and J such that $I = J - 1$.

3.11 Site off-diagonal τ-matrix elements

As we shall see in the next section, calculating the scattering of a system with a defect involves matrix multiplication between τ-matrices connecting sites at which the potential is perturbed. This requires the determination of the site off-diagonal τ-matrix elements, and hence we need an expression for the τ-matrix that connects sites in different layers. If we consider a system comprising adjacent layers I and J such that $I = J - 1$, as shown in figure (3.6), then to find τ_{IJ} we need to determine all the scattering paths starting from layer I that are finally incident on layer J.

In this section we will use T for the transmission and reflection matrices of the layers, R for the reflection matrices of the half-spaces, P as the plane-wave propagators, Γ to denote conversion from partial waves to plane waves and $\tilde{\Gamma}$ for conversion from plane waves to partial waves. Subscripts indicate the layer origin, and superscripts indicate the direction of travel of the wave. In this notation the off-diagonal τ-matrix is given by [21]

$$\begin{aligned}
\tau_{IJ} = & \left[{t_I}^{-1} - g_I\right]^{-1} \\
& \times \left[\Gamma_I^- \left[1 - P_{I-1}^- R_{I-1}^{-+} P_{I-1}^+ T_I^{+-}\right]^{-1} P_{I-1}^- R_{I-1}^{-+} P_{I-1}^+ T_I^{++} + \Gamma_I^+\right] P_I^+ \\
& \times \left[1 - P_J^+ R_{J+1}^{+-} P_J^- P_{J-1}^- R_{J-1}^{-+} P_{J-1}^+\right]^{-1} \\
& \times \left[\tilde{\Gamma}_J^+ + P_J^+ R_{J+1}^{+-} P_J^- \tilde{\Gamma}_J^-\right] \\
& \times \left[{t_J}^{-1} - g_J - \Delta_J\right]^{-1},
\end{aligned} \tag{3.88}$$

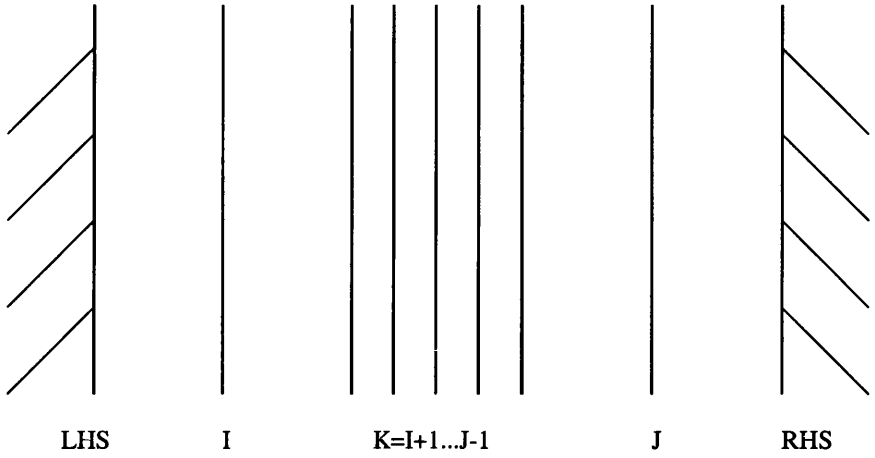

Figure 3.7: System with layers I and J separated by intermediate layers $K = I+1 \ldots J-1$.

where

$$\Delta_J = \left[\Gamma_J^- P_{J-1}^- R_{J-1}^{-+} P_{J-1}^+ + \Gamma_J^+\right] \left[1 - P_J^+ R_{J+1}^{+-} P_J^- P_{J-1}^- R_{J-1}^{-+} P_{J-1}^+\right]^{-1} \times \left[\tilde{\Gamma}_J^+ + P_J^+ R_{J+1}^{+-} P_J^- \tilde{\Gamma}_J^-\right] - \Gamma_J^+ \tilde{\Gamma}_J^+. \tag{3.89}$$

The first term in equation (3.88) represents paths which scatter solely within layer I. The second term sums paths which leave layer I and then travel right, i.e., towards layer J, for the first time, including multiple scattering with the left half-space. The third term represents multiple scattering between the left and right half-spaces, done in the absence of layer J. The fourth term is then waves that are incident on layer J, at this point the expression sums all the paths that originate in layer I and arrive at layer J, including all multiple scattering with the rest of the system except layer J. The final term includes scattering within layer J, and multiple scattering between layer J and the rest of the system. The quantity Δ_J which appears in the final term of equation (3.88) is defined in equation (3.89), where the three square bracketed terms represent scattering from layer J, multiple scattering between the half-spaces, and scattering back into layer J respectively. For scattering in the opposite direction, e.g., $I = J+1$, similar expressions apply, with transmission directions and layer origins altered .

In the case where layers I and J are separated by a number of additional layers an extra term is needed. Figure (3.7) shows a diagram of such a system. For the

system shown we need to insert an additional term

$$\prod_{K=I+1}^{J-1} \left[1 - T_K^{+-} P_{K-1}^{-} R_{K-1}^{-+} P_{K-1}^{+}\right] T_K^{++} P_K^{+}, \tag{3.90}$$

into equation (3.88), immediately before the third term which is the multiple scattering between the two half-spaces. Each factor in (3.90) advances the solution through an additional layer K, adding the scattering paths involving layer K and all those to the left.

These expressions for the site off-diagonal τ-matrix can be checked by partitioning the sites between layers in different ways. The τ-matrix connecting two sites in different planes can be determined by assigning the planes to different layers and using the above procedure, or by assigning both planes to a single layer. These two situations give two very different partitionings of the scattering events, yet result in an identical site off-diagonal τ-matrix, to within numerical error.

3.12 Defect τ-matrices

In this section we will derive expressions for the τ-matrix of a defect system, being a system in which the potential differs at a finite number of sites from some original system. The defect τ-matrices will be found to depend on the τ-matrices of the original system and the t-matrices of both the original and the defect system.

This property allows rapid calculation of the defect τ-matrices, if the τ-matrices for the original system are calculated and stored. Defect systems can be then be converged to self-consistency relatively quickly, without the need to laboriously calculate the substrate τ-matrices for each iteration.

In the following discussion the site indices and angular momentum indices are suppressed for clarity. We start from the definition of the τ-matrix (3.38),

$$\tau = t + tg\tau, \tag{3.91}$$

relating the τ-matrix with the t-matrix and the matrix elements of the free space

Green function. Multiplying through by t^{-1} from the left and τ^{-1} from the right gives

$$t^{-1} = \tau^{-1} + g. \tag{3.92}$$

Since the free space Green function is purely structural we can equate it for two systems which are structurally identical but have different potentials, such as a perfect crystal and one containing a defect potential. Hence

$$g = t^{-1} - \tau^{-1} = t_d^{-1} - \tau_d^{-1}, \tag{3.93}$$

where the d subscript distinguishes quantities relating to the defect system. Rearranging for the defect τ-matrix gives

$$\tau_d = [t_d^{-1} - t^{-1} + \tau^{-1}]^{-1}. \tag{3.94}$$

Replacing the difference between the inverse t-matrices $t^{-1} - t_d^{-1}$ with Δ, and pulling out a factor of τ gives

$$\tau_d = \tau[1 - \Delta\tau]^{-1}. \tag{3.95}$$

We can formally expand the inverted bracket as a series and rearrange,

$$\begin{aligned} \tau_d &= \tau[1 + \Delta\tau + \dots] \\ &= \tau[1 + \Delta\tau[1 - \Delta\tau]^{-1}] \\ &= \tau + \tau\Delta\tau[1 - \Delta\tau]^{-1} \\ &= \tau + \tau\Delta[1 - \tau\Delta]^{-1}\tau \end{aligned} \tag{3.96}$$

hence

$$\tau_d = \tau + \tau\Delta[1 - \tau\Delta]^{-1}\tau. \tag{3.97}$$

Equation (3.97) represents an expression for calculating the τ-matrix corresponding to a system in which the potential has changed at a finite number of sites, in terms of quantities corresponding to the original system, in particular the original t and τ-matrices, and the new t-matrices of the modified sites. The change in τ-matrices due to the presence of the defect, denoted $\delta\tau$, is thus

$$\delta\tau = \tau\Delta[1 - \tau\Delta]^{-1}\tau. \tag{3.98}$$

As Δ is non-zero only for those sites where the t-matrix, and hence the potentials, have changed, the internal sums in equation (3.98) need only be performed across those sites. In principle the perturbation due to a defect will extend beyond those sites. In practice it is usual to set $\delta\tau$ to zero for those sites with unchanged potentials. The accuracy of this approximation depends on the number of defect sites used, and on how effectively the perturbation is screened. Introducing

$$\mathcal{G} = \Delta \left[1 - \tau\Delta\right]^{-1}, \tag{3.99}$$

gives the following expression for $\delta\tau$,

$$\delta\tau = \tau\mathcal{G}\tau, \tag{3.100}$$

and the task is then reduced to calculating $\mathcal{G}$. Restricting the site summations to those sites with altered potentials allows the expression for $\mathcal{G}$ to be rearranged as follows,

$$\mathcal{G} = \Delta \left[1 - \tau\Delta\right]^{-1}, \tag{3.101}$$

$$\mathcal{G}^{-1} = \Delta^{-1} - \tau, \tag{3.102}$$

$$\Delta = \mathcal{G} - \Delta\tau\mathcal{G}, \tag{3.103}$$

$$\mathcal{G} = \Delta + \Delta\tau\mathcal{G}. \tag{3.104}$$

Equation (3.104) is particularly useful and will be used in the following section which details the calculation of defect τ-matrices for extended line defects.

Using the definition of $\delta\tau$ in equation (3.100), the full expression for the defect τ-matrices in terms of $\mathcal{G}$ is

$$\tau_d = \tau + \tau\mathcal{G}\tau, \tag{3.105}$$

where the implicit site summations in the second term are restricted to those sites at which the potential is altered. Equation (3.105) can be viewed as analogous to equation (3.14), relating the full Green function to the free space Green function and the total scattering matrix, $G = G_0 + G_0 T G_0$. In equation (3.105) therefore, τ is analogous to a free space Green function, and $\mathcal{G}$ is analogous to the scattering matrix. Thus, just as we can use T to construct a Green function, G, including the effects of scattering potentials from the free space Green function G_0, we can use $\mathcal{G}$ to construct a τ-matrix, τ_d, for a system which includes defect potentials

from the scattering properties of a periodic substrate system, τ.

We are thus able to calculate the electronic structure of an infinite periodic system with a finite number of defect potentials, by first calculating the τ-matrix for the infinite periodic system using the k-space method detailed previously, then subsequently using these τ-matrices with equation (3.105) to determine the scattering at the defect sites. It should be noted that the site off-diagonal elements of the τ-matrix are required, due to the site summations in equation (3.105)

3.13 Chain defects

In this section we will examine the calculation of τ-matrices for systems comprising extended one-dimensional defects, for example a chain of atoms on a surface. In the previous section we derived an expression for the τ-matrix of a system with a finite number of sites having potentials differing from those in some original system. This requires sums over those sites with differing potentials. For extended one-dimensional defects the number of sites with differing potentials is infinite however, so the expressions for the defect τ-matrices derived in the previous section are only valid if a lattice Fourier transform has been performed.

In this derivation, and throughout the rest of this thesis, we take the line defects to run parallel to the y-axis, hence the system is periodic in the y-direction. This periodicity allows us to solve for the k_y resolved τ-matrix, hence site summations are performed in the x-unit cell index and in the site within the unit cell index, while the troublesome infinite summation over the y-unit cell index is avoided. This necessitates an expansion of the unit cell indices to differentiate between x and y, as shown in figure (3.8).

In terms of the new site indices, the τ-matrices are given by

$$\tau^{Ii\alpha;Jj\beta} = \int \frac{d\mathbf{k}}{\Omega} \tau^{\alpha\beta}(\mathbf{k}) e^{-i\mathbf{k}\cdot(\mathbf{R}_{Ii}-\mathbf{R}_{Jj})}, \tag{3.106}$$

$$= \int \frac{dk_y}{\Omega_y} \tau^{I\alpha J\beta}(k_y) e^{-ik_y(Y_i-Y_j)}, \tag{3.107}$$

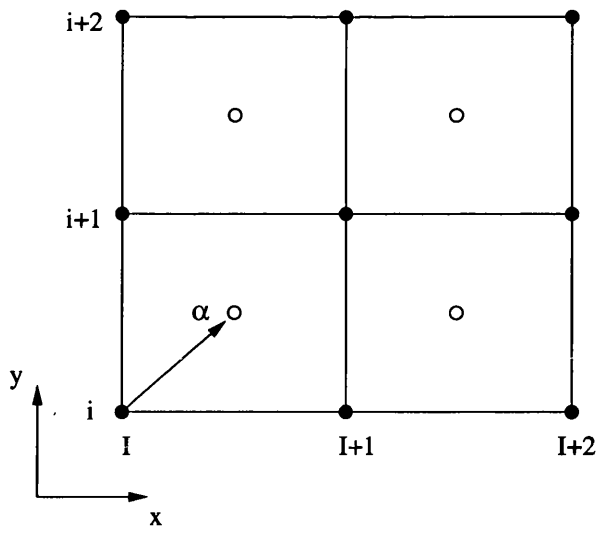

Figure 3.8: Diagram showing the unit cell indices introduced to allow the treatment of systems with one-dimensional periodicity.

where the $\tau^{I\alpha J\beta}(k_y)$ are the k_y-resolved τ-matrices, given by

$$\tau^{I\alpha;J\beta}(k_y) = \int \frac{dk_x}{\Omega_x} \tau^{\alpha\beta}(\mathbf{k}) e^{-ik_x(X_I - X_J)}. \tag{3.108}$$

In order to use the k_y-resolved τ-matrices with equation (3.105) to calculate the defect τ-matrices, we will need an expression for the quantity $\mathcal{G}$ which is also k_y resolved.

In the re-labelled index scheme, where for clarity we have replaced $I\alpha$ with μ, $\mathcal{G}$ is given by

$$\mathcal{G}^{\mu i;\mu' j} = \Delta^{\mu}\delta_{\mu\mu'}\delta_{ij} + \sum_{\mu'' k} \Delta^{\mu}\tau^{\mu i;\mu'' k}\mathcal{G}^{\mu'' k;\mu' j}, \tag{3.109}$$

where the site summation over μ'' is restricted to defect sites (as is the summation over k, but in that case the defect extends over an infinite site index). We can perform a lattice Fourier transform to obtain an expression for $\mathcal{G}(k_y)$

$$\begin{aligned}\mathcal{G}^{\mu\mu'}(k_y) =& \frac{1}{N_y}\sum_{ij}\mathcal{G}^{\mu i;\mu' j}e^{ik_y(Y_i - Y_j)} \\ =& \Delta^{\mu}\delta_{\mu\mu'} \\ &+ \frac{1}{N_y}\Delta^{\mu}\sum_{ijk\mu''}\tau^{\mu i;\mu'' k}e^{ik_y(Y_i - Y_k)}\mathcal{G}^{\mu'' k;\mu' j}e^{ik_y(Y_k - Y_j)}.\end{aligned} \tag{3.110}$$

Shifting y-unit cell indices and setting $i' = i - k$ and $k' = k - j$ allows us to write

$$\begin{aligned}\mathcal{G}^{\mu\mu'}(k_y) =& \Delta^{\mu}\delta_{\mu\mu'} \\ &+ \frac{1}{N_y}\Delta^{\mu}\sum_{i'k'\mu''}\tau^{\mu i';\mu''0}e^{ik_yY_{i'}}\mathcal{G}^{\mu''k';\mu'0}e^{ik_yY_{k'}} \\ =& \Delta^{\mu}\delta_{\mu\mu'} + \Delta^{\mu}\sum_{\mu''}\tau^{\mu\mu''}(k_y)\mathcal{G}^{\mu''\mu'}(k_y),\end{aligned} \tag{3.111}$$

where we have made use of the following relation,

$$\begin{aligned}\tau^{\mu\mu'}(k_y) &= \frac{1}{N_y}\sum_{ij}\tau^{\mu i;\mu' j}e^{ik_y(Y_i - Y_j)} \\ &= \frac{1}{N_y}\sum_{ij}\tau^{\mu i-j;\mu'0}e^{ik_yY_{i-j}} \\ &= \frac{1}{N_y}\sum_{i'}\tau^{\mu i';\mu'0}e^{ik_yY_{i'}}.\end{aligned} \tag{3.112}$$

Thus we have an expression for $\mathcal{G}(k_y)$,

$$\mathcal{G}^{\mu\mu'}(k_y) = \Delta^{\mu}\delta_{\mu\mu'} + \Delta^{\mu}\sum_{\mu''}\tau^{\mu\mu''}(k_y)\mathcal{G}^{\mu''\mu'}(k_y), \tag{3.113}$$

which can be rearranged into a form analogous to equation (3.99), hence

$$\mathcal{G}^{\mu\mu'}(k_y) = \left\{\left[\Delta^{-1} - \tau(k_y)\right]^{-1}\right\}^{\mu\mu'}. \tag{3.114}$$

Returning to the expression for the change in the τ-matrices due to the presence of defect potentials, we have

$$\delta\tau^{ij} = \sum_{nm}\tau^{in}\mathcal{G}^{nm}\tau^{mj}, \tag{3.115}$$

which, in the re-labelled index scheme becomes

$$\delta\tau^{\mu i;\mu' j} = \sum_{\mu''\mu'''kk'}\tau^{\mu i;\mu'' k}\mathcal{G}^{\mu'' k;\mu''' k'}\tau^{\mu''' k';\mu' j}. \tag{3.116}$$

Note that the site summations appearing in these expressions are restricted to those sites at which the potential is changed. From the lattice Fourier transform equations, we have expressions relating the k_y resolved τ-matrices and $\mathcal{G}$ to their

real space equivalents,

$$\tau^{\mu i;\mu' j} = \int \frac{dk_y}{\Omega_y} \tau^{\mu\mu'}(k_y) e^{-ik_y(Y_i - Y_j)}, \tag{3.117}$$

$$\mathcal{G}^{\mu i;\mu' j} = \int \frac{dk_y}{\Omega_y} \mathcal{G}^{\mu\mu'}(k_y) e^{-ik_y(Y_i - Y_j)}, \tag{3.118}$$

Substituting these expressions into (3.116), we then have an expression for $\delta\tau$ in terms of the k_y resolved quantities,

$$\delta\tau^{\mu i;\mu' j} = \sum_{\mu''\mu'''} \int \frac{dk_y}{\Omega_y} \tau^{\mu\mu''}(k_y) \mathcal{G}^{\mu''\mu'''}(k_y) \tau^{\mu'''\mu'}(k_y) e^{-ik_y(Y_i - Y_j)}, \tag{3.119}$$

where

$$\mathcal{G}^{\mu\mu'}(k_y) = \left\{ \left[\Delta^{-1} - \tau(k_y) \right]^{-1} \right\}^{\mu\mu'}. \tag{3.120}$$

Therefore the change induced in the tau matrix by one or more line defects can be expressed in terms of the k_y resolved original tau matrices, and the original and defect t-matrices. This need only be solved within one unit cell in the y-direction and is therefore ideal to treat, for example, a monatomic wire on a surface.

In conclusion then, we have a scheme for calculation the tau matrices for a system of one or more line defects, which requires only the t-matrices of the substrate and defect systems, and the k_y resolved tau matrices of the substrate system. The k_y resolved tau matrices for a given substrate system can readily be calculated using the LKKR method, and stored for future use. The stored $\tau(k_y)$ can then be read in on each iteration of a defect calculation, greatly reducing the required computing time.

Chapter 4

Poisson Solution

4.1 Introduction

To obtain self-consistent potentials within the framework of density functional theory [58, 70] it is necessary to solve an iterated cycle of Schrödinger and Poisson equations. In this process, an initial potential is used to generate a charge density, which then yields a new potential as an input for the next iteration. Clearly the solution of Poisson's equation is as important a step in the self-consistency cycle as the solution of the Schrödinger equation.

As was discussed in chapter 2, in the self-consistency process the new potential is given by

$$V(\mathbf{r}) = V_C(\mathbf{r}) + v_{xc}(\mathbf{r}) \tag{4.1}$$

where $V_C(\mathbf{r})$ is the Coulomb potential, including the contributions from the electronic and nuclear charge, and $v_{xc}(\mathbf{r})$ is the exchange-correlation potential. The Coulomb potential is found by solving Poisson's equation for the charge density of the system, which will be detailed in the following sections. The exchange-correlation potential approximates the many-body interactions between electrons for which the Perdew-Wang form has been used [99]. The potential thus obtained is mixed with the original potential and used as the new input to the self-consistency cycle, as outlined in chapter 2.

4.2 Electrostatic contribution

This section is concerned with evaluation of the electrostatic contribution to the potential, which involves the solution of Poisson's equation

$$\nabla^2 V_C(\mathbf{r}) = -4\pi\rho(\mathbf{r}), \tag{4.2}$$

where $\rho(\mathbf{r})$ is the charge density of the system. In order to perform self-consistent calculations on chain defect systems, we will need solutions of Poisson's equation for systems with one-dimensional periodicity.

The derivations in this section assume a system where space is partitioned into Wigner-Seitz (WS) cells - space-filling regions that are normally centred on atomic sites. For a general system of such cells the solution for the electrostatic potential has an expansion [45] within cell $\mathbf{R}$ of $V_C(\mathbf{r}) = V_{C,\mathbf{R}}(\mathbf{r}-\mathbf{R})$ where

$$V_{C,\mathbf{R}}(\mathbf{r}) = -\frac{Z_\mathbf{R}}{r} + \int_{\tau_\mathbf{R}} \frac{\rho_\mathbf{R}(\mathbf{r}')}{|\mathbf{r}-\mathbf{r}'|} d^3\mathbf{r}' + V_{M,\mathbf{R}}(\mathbf{r}) + \Delta V_{M,\mathbf{R}}(\mathbf{r}). \tag{4.3}$$

The first two terms arise from the nuclear charge $Z_\mathbf{R}$ and electronic charge density $\rho_\mathbf{R}$ within cell $\mathbf{R}$. These terms are relatively simple to calculate, the electronic charge density being found by direct numerical integration of the local density of states - see chapter 5. The third term $V_{\mathrm{M},\mathbf{R}}(\mathbf{r})$ is the Madelung potential that arises from the charge density in all other WS cells, which can be characterised by the multipoles

$$Q_{\mathbf{R}L} = \int_{\tau_\mathbf{R}} r^\ell Y_L^*(\mathbf{r})\rho_\mathbf{R}(\mathbf{r}) d^3\mathbf{r} - \frac{Z_\mathbf{R}}{\sqrt{4\pi}}\delta_{\ell,0}. \tag{4.4}$$

For more details on the calculation of the multipoles, see section 5.2.

The Madelung potential is given by [59]

$$V_{M,\mathbf{R}}(\mathbf{r}) = \sum_{\mathbf{R}'}{}' \sum_L \frac{4\pi}{2\ell+1} \frac{Y_L(\mathbf{r}+\mathbf{R}-\mathbf{R}')}{|\mathbf{r}+\mathbf{R}-\mathbf{R}'|^{\ell+1}} Q_L^{\mathbf{R}'}, \tag{4.5}$$

where L is the usual composite angular momentum index (ℓ, m), and the prime in (4.5) denotes the omission of the term $\mathbf{R}' = \mathbf{R}$. The final term in (4.3) is a correction to the Madelung term that arises from those cells $\mathbf{R}'$ which have a bounding sphere, the smallest sphere centred on $\mathbf{R}'$ that fully contains the WS

cell $\tau_{\mathbf{R}'}$, that overlaps with the bounding sphere of cell $\mathbf{R}$. It is not specific to one-dimensional systems and its evaluation is discussed elsewhere [45]. In the atomic sphere approximation, used elsewhere in this thesis for the defect calculations, this term is omitted.

The lattice sum which appears in equation (4.5) can be evaluated directly for large values of ℓ, but for small ℓ it is conditionally or poorly convergent. For three-dimensional lattices the Ewald technique [32] is an effective method for evaluating these sums. In the case of the chain defect calculations described in this work, we have the more complex problem of a system of one-dimensional defects to a substrate system that is periodic in two-dimensions. As the Poisson equation is linear we are able to partition the charge in the system in whichever manner is convenient, and solve the Poisson equation for each contribution separately. We therefore separate the Madelung potential into a contribution from the substrate system and a contribution from the defect system,

$$V_{M,\mathbf{R}}(\mathbf{r}) = V_{S,\mathbf{R}}(\mathbf{r}) + V_{D,\mathbf{R}}(\mathbf{r}). \tag{4.6}$$

$V_{D,\mathbf{R}}(\mathbf{r})$ is then the Madelung potential arising from the difference in electronic density between the system with and without the defect. Since the substrate system is fixed, the contribution $V_{S,\mathbf{R}}(\mathbf{r})$ can be read in along with the τ-matrices, and thus need not be recalculated for each iteration. Interest in the properties of thin-films and interfaces have previously led to the extension of the Ewald method to two-dimensional charge distributions [83, 114], and for more details concerning the evaluation of the Madelung potential for two-dimensional systems we refer the reader to these references. We concentrate our presentation on the new aspects particular to the chain-defect geometry.

We represent the defect as a cluster of chains whose potentials are permitted to vary, embedded in the infinite substrate system. The defect contribution to the Madelung potential can then be found from the multipoles of the difference charge density. In principle this contribution will not be limited to sites within the defect cluster calculation; the perturbation to the potentials due to the presence of the defect might not be wholly confined to the defect cluster of chains. However in the defect calculations we fix the potentials of the sites outside of the cluster to the substrate values, so that any contribution from the defect system to these potentials is ignored. For this assumption to be justified the perturbation extending beyond the defect should ideally be small, and for many, especially

metallic systems, the screening effect of the other sites included in the cluster will indeed tend to reduce the effects of the defect outside of the cluster. This is analogous to 2D LKKR surface calculations, in which the perturbation to the potentials due to the surface is screened by the material such that the inclusion of 4-5 layers is sufficient to recover bulk potentials. This screening, along with the tendency towards charge neutrality as the system is converged self-consistently, generally ensures that the errors from limiting the perturbation to the cluster are small. These errors can be quantified and reduced by systematically increasing the size of the cluster. This has the effect of including more chains to screen the charge on the defect, reducing the magnitude of the perturbation outside of the defect. Studies of the convergence of chain defect calculations with respect to cluster size are given in section 5.9.

The chains, and therefore the cluster, have one-dimensional periodicity, hence the Ewald method needs to be extended to deal with one-dimensional charge distributions. Previous work has touched upon one-dimensional Ewald methods [26], although not in relation to the calculation of Madelung potentials for electronic structure calculations. The following section describes the extension of the Ewald method to one-dimensional systems in detail and derives the necessary expressions for evaluating the one-dimensional lattice sums which arise [76].

4.3 One-dimensional Madelung potential

In a system with one-dimensional periodicity, the WS cells can be labelled by a chain label $\mathbf{R}$, the vector pointing to the origin of one cell of the chain, and a one-dimensional lattice vector $\mathbf{u}_\parallel$ indexing the position along the chain. Because of the periodicity quantities such as the electronic charge density and the electrostatic potential V_C satisfy e.g., $V_C(\mathbf{r}) = V_C(\mathbf{r} - \mathbf{u}_\parallel)$, and so need only be determined within the origin cell of each chain.

The Madelung contribution for a system with one-dimensional periodicity is given by

$$V_{M,\mathbf{R}}(\mathbf{r}) = \sum_{\mathbf{R}',\mathbf{u}_\parallel}{}' \sum_L \frac{4\pi}{2\ell+1} \frac{Y_L(\mathbf{r}+\mathbf{R}-\mathbf{R}'-\mathbf{u}_\parallel)}{|\mathbf{r}+\mathbf{R}-\mathbf{R}'-\mathbf{u}_\parallel|^{\ell+1}} Q_L^{\mathbf{R}'}, \tag{4.7}$$

where the prime in (4.7) denotes the omission of the term $\mathbf{R}' = \mathbf{R}$, $\mathbf{u}_{\|} = 0$. Equation (4.7) is conveniently written as [113]

$$V_{M,\mathbf{R}}(\mathbf{r}) = \sum_{LL'R'} Y_L(\mathbf{r}) r^{\ell} M_{LL'}^{\mathbf{RR}'} Q_{L'}^{\mathbf{R}'} \tag{4.8}$$

with the Madelung matrix

$$M_{LL'}^{\mathbf{RR}'} = 16\pi^2(-1)^{\ell} \frac{(2\ell''-1)!!}{(2\ell'+1)!!(2\ell+1)!!} C_{L'L''}^{L} S_{L''}^{*}(\mathbf{R}-\mathbf{R}') \tag{4.9}$$

with $\ell'' = \ell + \ell'$, $m'' = m - m'$, $C_{L'L''}^{L} = \int_{4\pi} Y_L^*(\Omega) Y_{L'}(\Omega) Y_{L''}(\Omega)\, d\Omega$ a Gaunt coefficient and

$$S_L(\mathbf{R}) = \sum_{\mathbf{u}_{\|}}{}' \frac{Y_L(\mathbf{R}-\mathbf{u}_{\|})}{|\mathbf{R}-\mathbf{u}_{\|}|^{\ell+1}}, \tag{4.10}$$

the prime denoting the omission of any singular term $\mathbf{u}_{\|} = \mathbf{R}$. For sufficiently large ℓ this sum may be evaluated practically by direct summation, but for small ℓ it is conditionally or poorly convergent, and it is here that an Ewald-type treatment is required. This Ewald treatment will be derived in the next section.

The expressions given above are valid for the general case of non-spherical potentials. In the atomic sphere approximation, used for the defect calculations in this thesis, the potential is spherically symmetric. The sum over L in equation (4.8) is therefore restricted to just the $\ell, m = 0$ term,

$$V_{M_{00},\mathbf{R}} = \sum_{L'R'} \frac{1}{\sqrt{4\pi}} M_{00,L'}^{\mathbf{RR}'} Q_{L'}^{\mathbf{R}'}. \tag{4.11}$$

This term no longer has any $\mathbf{r}$ dependence, so the Madelung potential due to the defect system for each chain is a constant term. From inspection of (4.8) it is clear that allowing $r \to 0$ results in the same expression. In the chain defect calculations described in chapter 5 of this thesis, only the multipoles up to $\ell = 1$ are considered, thus curtailing the sum over L' in (4.11).

4.4 Ewald transformation

In order to evaluate (4.10) we consider the evaluation of

$$S(\mathbf{r}) = \sum_{\mathbf{u}_\parallel}{}' \frac{1}{|\mathbf{r} - \mathbf{u}_\parallel|}, \tag{4.12}$$

from which the required sums may be obtained by differentiation, as discussed in the following section. Initially assuming $r_\perp \neq 0$, we write $S(\mathbf{r})$ as two sums, using the integral representation of the Gamma function [1]

$$\frac{1}{r^{2z}} = \frac{1}{\Gamma(z)} \int_0^\infty \frac{e^{-r^2 t}}{t^{1-z}} dt \tag{4.13}$$

for $z = 1/2$ and dividing the range of integration into $[0, \mu]$ and $[\mu, \infty]$, with $\mu > 0$ an arbitrary split parameter that is chosen for optimum performance. The contribution from the upper range decreases rapidly with increasing r, leading to a convergent real space sum

$$S^{(1)}(\mathbf{r}) = \sum_{\mathbf{u}_\parallel} \frac{1}{\sqrt{\pi}} \int_\mu^\infty e^{-|\mathbf{r}-\mathbf{u}_\parallel|^2 t} \frac{dt}{\sqrt{t}} = \frac{1}{\sqrt{\pi}} \sum_{\mathbf{u}_\parallel} \frac{\Gamma(1/2, \mu|\mathbf{r} - \mathbf{u}_\parallel|^2)}{|\mathbf{r} - \mathbf{u}_\parallel|} \tag{4.14}$$

where $\Gamma(n, z)$ is the incomplete Gamma function [1]. For the second sum arising from the lower range of the integral

$$S^{(2)}(\mathbf{r}) = \sum_{\mathbf{u}_\parallel} \frac{1}{\sqrt{\pi}} \int_0^\mu e^{-|\mathbf{r}-\mathbf{u}_\parallel|^2 t} \frac{dt}{\sqrt{t}} = \frac{1}{\sqrt{\pi}} \int_0^\mu \sum_{\mathbf{u}_\parallel} e^{-|\mathbf{r}_\parallel-\mathbf{u}_\parallel|^2 t} e^{-r_\perp^2 t} \frac{dt}{\sqrt{t}}. \tag{4.15}$$

we exploit the periodicity of the sum of Gaussians within the integrand, substituting the Fourier series representation

$$\sum_{\mathbf{u}_\parallel} e^{-|\mathbf{r}_\parallel-\mathbf{u}_\parallel|^2 t} = \frac{1}{a}\sqrt{\frac{\pi}{t}} \sum_{g_\parallel} e^{-g_\parallel^2/4t} \cos(g_\parallel r_\parallel). \tag{4.16}$$

Separating out the $g_\parallel = 0$ term gives $S^{(2)}(\mathbf{r}) = S^{(2')}(\mathbf{r}) + S^{(3)}(\mathbf{r})$ with

$$S^{(2')}(\mathbf{r}) = \frac{2}{a} \sum_{g_\parallel > 0} \cos(g_\parallel r_\parallel) I_0(g_\parallel/2, r_\perp, \mu), \tag{4.17}$$

where we introduce the integral

$$I_n(a,b,\mu) = \int_0^\mu e^{-a^2/t} e^{-b^2 t} t^{n-1} dt \quad (n = 0,1,2,\ldots; a > 0) \tag{4.18}$$

whose evaluation is considered in section 4.6 below, and

$$\begin{aligned} S^{(3)}(\mathbf{r}) &= \frac{1}{a}\int_0^\mu e^{-r_\perp^2 t}\frac{dt}{t} = \frac{1}{a}\lim_{s\to 0+}\left[E_1(sr_\perp^2) - E_1(\mu r_\perp^2)\right] \\ &= -\frac{1}{a}\left[\gamma + \ln r_\perp^2 + E_1(\mu r_\perp^2)\right] - \frac{1}{a}\lim_{s\to 0+}\ln s, \end{aligned} \tag{4.19}$$

where $E_n(t)$ is the exponential integral function [1]. We have used $\lim_{t\to 0+} E_1(t) = -\gamma - \lim_{t\to 0+}\ln t$ with γ Euler's constant.

The final singular contribution to (4.19) has no physical relevance, and may be omitted on account of charge neutrality. In terms of the lattice sums required for the Madelung matrices (4.9) it only enters for $L = L' = (00)$, vanishing under the differentiation (4.22) that generates other terms. Furthermore, in evaluating the potential the $L = L' = (00)$ terms are summed over all chains, scaled by the corresponding charges. Thus the prefactor of the singular terms includes a factor which is the sum of charges within the system, zero in a charge neutral system. We drop this term in the subsequent analysis.

Combining, we obtain the following expression for $S(\mathbf{r})$:

$$\begin{aligned} S(\mathbf{r}) &= \frac{1}{\sqrt{\pi}}\sum_{\mathbf{u}_\parallel}\frac{\Gamma(1/2,\mu|\mathbf{r}-\mathbf{u}_\parallel|^2)}{|\mathbf{r}-\mathbf{u}_\parallel|} + \frac{2}{a}\sum_{g_\parallel>0}\cos(g_\parallel r_\parallel) I_0(g_\parallel/2, r_\perp, \mu) \\ &\quad - \frac{1}{a}\left[\gamma + \ln r_\perp^2 + E_1(\mu r_\perp^2)\right] \qquad r_\perp \neq 0 \end{aligned} \tag{4.20}$$

$$\begin{aligned} &= \frac{1}{\sqrt{\pi}}{\sum_{\mathbf{u}_\parallel}}'\frac{\Gamma(1/2,\mu|\mathbf{r}-\mathbf{u}_\parallel|^2)}{|\mathbf{r}-\mathbf{u}_\parallel|} + \frac{2}{a}\sum_{g_\parallel>0}\cos(g_\parallel r_\parallel) I_0(g_\parallel/2, 0, \mu) \\ &\quad + \frac{1}{a}\ln\mu - \sum_{\mathbf{u}_\parallel}\frac{2\sqrt{\mu}}{\sqrt{\pi}}\delta_{r_\parallel,\mathbf{u}_\parallel} \qquad r_\perp = 0. \end{aligned} \tag{4.21}$$

For $r_\perp = 0$ the last two terms originate from taking the limit $r_\perp \to 0$ in the previous expressions for $S^{(3)}(\mathbf{r})$ and $S^{(1)}(\mathbf{r})$ respectively.

4.5 One-dimensional lattice sums

In terms of $S(\mathbf{r})$, the lattice sums required for the Madelung potential $S_L(\mathbf{R})$ may be obtained as [85]

$$S_L(\mathbf{R}) = \frac{1}{(2\ell-1)!!}\left[\mathcal{Y}_L(-\nabla)S(\mathbf{r})\right]_{\mathbf{r}=\mathbf{R}} \tag{4.22}$$

where

$$\mathcal{Y}_L(\mathbf{r}) = r^\ell Y_L(\mathbf{r}). \tag{4.23}$$

is a polynomial in x, y, z and the differential operator in (4.22) understood to be the result of substituting $x \rightarrow -\partial_x$, etc. Due to the cylindrical symmetry of the system taking the z-axis to coincide with $\mathbf{e}_\parallel$ results in more elegant expressions for the $S_L(\mathbf{R})$ terms, hence these are the expressions given in this section. In order to remain compatible with the 2D LKKR method, described in chapter 3, a practical implementation of this 1D Ewald technique has been realised in which the chains are parallel to the y-axis, with the z-axis normal to the 2D layers. Thus the $S_L(\mathbf{R})$ expressions used in this code take the y-axis to coincide with $\mathbf{e}_\parallel$, and the corresponding expressions can be found in Appendix A.

Applying (4.22) to (4.20,4.21) and taking the z-axis to coincide with $\mathbf{e}_\parallel$, we obtain

$$S_{00}(\mathbf{R}) = \frac{S(\mathbf{R})}{\sqrt{4\pi}} \tag{4.24}$$

$$\begin{aligned} S_{10}(\mathbf{R}) = {} & \frac{2}{\sqrt{\pi}}{\sum_{\mathbf{u}_\parallel}}' \frac{\Gamma(3/2, \mu|\mathbf{R}-\mathbf{u}_\parallel|^2)}{|\mathbf{R}-\mathbf{u}_\parallel|^2} Y_{10}(\mathbf{R}-\mathbf{u}_\parallel) \\ & + \frac{\sqrt{3}}{a\sqrt{\pi}} \sum_{g_\parallel>0} g_\parallel \sin(g_\parallel R_\parallel) I_0(g_\parallel/2, R_\perp, \mu) \end{aligned} \tag{4.25}$$

$$\begin{aligned} S_{11}(\mathbf{R}) = {} & \frac{2}{\sqrt{\pi}}{\sum_{\mathbf{u}_\parallel}}' \frac{\Gamma(3/2, \mu|\mathbf{R}-\mathbf{u}_\parallel|^2)}{|\mathbf{R}-\mathbf{u}_\parallel|^2} Y_{11}(\mathbf{R}-\mathbf{u}_\parallel) \\ & - \frac{\sqrt{3}}{a\sqrt{2\pi}} R_\perp e^{i\phi_\mathbf{R}} \sum_{g_\parallel} \cos(g_\parallel R_\parallel) I_1(g_\parallel/2, R_\perp, \mu) \end{aligned} \tag{4.26}$$

$$\begin{aligned} S_{20}(\mathbf{R}) = {} & \frac{4}{3\sqrt{\pi}}{\sum_{\mathbf{u}_\parallel}}' \frac{\Gamma(5/2, \mu|\mathbf{R}-\mathbf{u}_\parallel|^2)}{|\mathbf{R}-\mathbf{u}_\parallel|^3} Y_{20}(\mathbf{R}-\mathbf{u}_\parallel) \\ & - \frac{\sqrt{5}}{3a\sqrt{\pi}} \sum_{g_\parallel>0} \cos(g_\parallel R_\parallel) \left[g_\parallel^2 I_0(g_\parallel/2, R_\perp, \mu) - 2I_1(g_\parallel/2, R_\perp, \mu) + 2R_\perp^2 I_2(g_\parallel/2, R_\perp, \mu) \right] \\ & + \frac{\mu\sqrt{5}}{3a\sqrt{\pi}} e^{-\mu R_\perp^2} \end{aligned} \tag{4.27}$$

$$\begin{aligned} S_{21}(\mathbf{R}) = {} & \frac{4}{3\sqrt{\pi}}{\sum_{\mathbf{u}_\parallel}}' \frac{\Gamma(5/2, \mu|\mathbf{R}-\mathbf{u}_\parallel|^2)}{|\mathbf{R}-\mathbf{u}_\parallel|^3} Y_{21}(\mathbf{R}-\mathbf{u}_\parallel) \\ & - \frac{2\sqrt{5}}{a\sqrt{6\pi}} R_\perp e^{i\phi_\mathbf{R}} \sum_{g_\parallel>0} g_\parallel \sin(g_\parallel R_\parallel) I_1(g_\parallel/2, R_\perp, \mu) \end{aligned} \tag{4.28}$$

$$\begin{aligned} S_{22}(\mathbf{R}) = {} & \frac{4}{3\sqrt{\pi}}{\sum_{\mathbf{u}_\parallel}}' \frac{\Gamma(5/2, \mu|\mathbf{R}-\mathbf{u}_\parallel|^2)}{|\mathbf{R}-\mathbf{u}_\parallel|^3} Y_{22}(\mathbf{R}-\mathbf{u}_\parallel) \\ & + \frac{\sqrt{5}}{a\sqrt{6\pi}} R_\perp^2 e^{2i\phi_\mathbf{R}} \sum_{g_\parallel} \cos(g_\parallel R_\parallel) I_2(g_\parallel/2, R_\perp, \mu) \end{aligned} \tag{4.29}$$

For $\ell > 2$ direct summation is sufficiently rapid, and terms for $m < 0$ may be found from $S_{\ell m}(\mathbf{R}) = (-1)^m S^*_{\ell -m}(\mathbf{R})$. The incomplete Gamma functions are readily obtained through recursion, using $\Gamma(n+1, z) = n\Gamma(n, z) + z^n e^{-z}$ starting with $\Gamma(1/2, z) = \sqrt{\pi}\ \mathrm{erfc}(\sqrt{z})$.

4.6 Evaluation of $I_n(a, b, \mu)$

The integrals (4.18) that appear in the expressions for $S_L(\mathbf{R})$ appear to be a time consuming element of the calculation, but numerically they are readily evaluated. Initially considering $n = 0$ and changing variables to $y = \mu/t$

$$\begin{aligned} I_0(a, b, \mu) &= \int_1^\infty e^{-a^2 y/\mu} e^{-b^2 \mu/y} \frac{dy}{y} \qquad (a > 0) \\ &= \sum_{m=0}^{\infty} \frac{(-b^2\mu)^m}{m!} E_{m+1}(a^2/\mu) \end{aligned} \tag{4.30}$$

where the series expansion of the second exponential factor has been made, and the exponential integral function recognised. Since $E_{m+1}(x) \leq \exp(-x)/(x+m)$, the series is convergent. The corresponding series for $I_n(a, b, \mu)$ may be found by differentiation:

$$I_n(a, b, \mu) = \frac{\partial^n}{\partial(-b^2)^n} I_0(a, b, \mu). \tag{4.31}$$

The exponential integral function satisfies $E_{m+1}(z) = [\exp(-z) - zE_m(z)]/m$, enabling the integrals to be evaluated in the series form

$$I_n(a, b, \mu) = \frac{1}{(-b^2)^n} \sum_{m=0}^{\infty} c_{n,m} \tag{4.32}$$

with the coefficients determined by one step recursion relations in either index

$$c_{0,0} = E_1(a^2/\mu) \tag{4.33}$$

$$c_{0,m} = \frac{a^2 b^2}{m^2} c_{0,m-1} + \frac{(-b^2\mu)^2}{mm!} e^{-a^2/\mu} \tag{4.34}$$

$$c_{n,m} = (m - n + 1) c_{n-1,m} \tag{4.35}$$

Algorithms and code for evaluating $E_1(x)$ are widely available [1, 104]. There are two special cases. If $b = 0$, then

$$I_n(a, 0, \mu) = \mu^n E_{n+1}(a^2/\mu) \tag{4.36}$$

$$= -\frac{a^2}{n} I_{n-1}(a, 0, \mu) + \frac{\mu^n}{n} e^{-a^2/\mu} \tag{4.37}$$

with $I_0(a,0,\mu) = E_1(a^2/\mu)$, and if $a = 0$ (and $n > 0$)

$$I_1(0,b,\mu) = \frac{1 - e^{-b^2\mu}}{b^2} \tag{4.38}$$

$$I_{n+1}(0,b,\mu) = \frac{n}{b^2} I_n(0,b,\mu) - \frac{\mu^n}{b^2} e^{-b^2\mu}. \tag{4.39}$$

Numerical investigations indicate $\mu \approx 0.1$ gives most efficient evaluation of the lattice sums, although a smaller value becomes necessary for large $r_\perp$. Examining equation (4.30) it is clear that while the series is convergent, the rate of convergence will be controlled by the size of $b^2\mu$. In evaluating the $S_L(\mathbf{R})$ terms b is replaced by $r_\perp$, therefore for large values of $r_\perp$ the factor $r_\perp^2\mu$ becomes large and the rate of convergence suffers. As μ is an arbitrary split parameter this problem can be avoided by simply reducing μ in proportion to $1/r_\perp^2$.

It is worth noting that the integrals $I_n(a,b,\mu)$ (4.18) can be expressed as

$$I_n(a,b,\mu) = \mu^n W_n(\mu^{-1}a^2, \mu b^2), \tag{4.40}$$

where

$$W_n(x,y) = \int_1^\infty \frac{e^{-x\mu} e^{-y/\mu}}{\mu^{n+1}}\, d\mu. \tag{4.41}$$

The function W_n defined in equation (4.41) is known (for $n = 0$) as the leaky aquifer function [51]. More sophisticated methods to evaluate this function have been developed than those above, in order to ensure a convergent expression for all ranges of the parameters. As mentioned above however, due to the arbitrary nature of the split parameter μ the simple recursion method can be guaranteed to converge.

In terms of computational costs, calculation of the Madelung matrix for a system with $\mathbf{R}, \mathbf{R}' = 1, 2, 3, \ldots 37$ unique sites and all angular momenta L, L' up to $\ell = 8$ takes of the order of 1 second on a modest desktop workstation. Furthermore, the Madelung matrix need only be evaluated once for a given system, stored, and then read in during the iterations to self-consistency. In comparison with other parts of the calculation these costs are negligible.

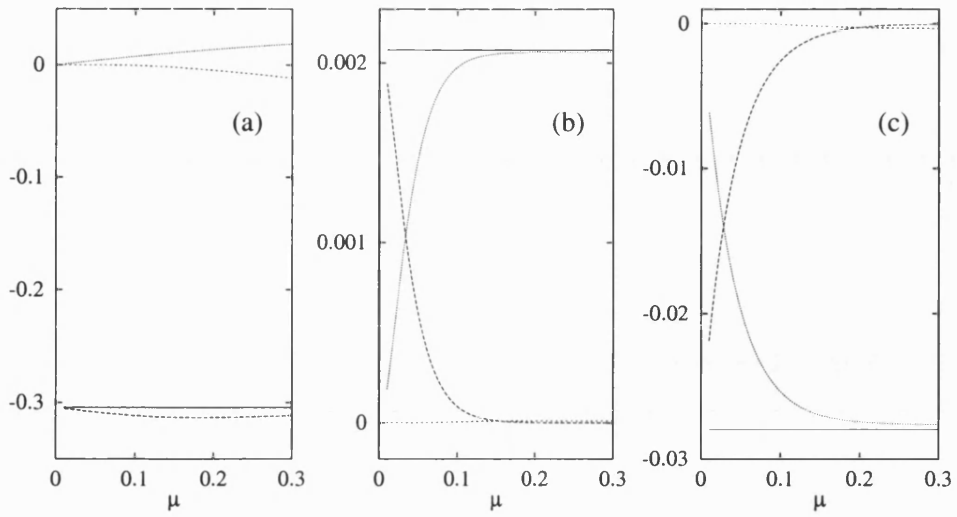

Figure 4.1: Examples of the breakdown of the lattice sums $S_L(\mathbf{R})$ into contributions from the real space sum (long dash), reciprocal space sum (short dash), and $g_{\|} = 0$ term (dots), as a function of the Ewald split parameter μ. The results illustrate behaviour for various L and $\mathbf{R}$, (a) $\ell m = 20$, $\mathbf{R} = (1, 0, 0)$ (b) $\ell m = 22$, $\mathbf{R} = (5, 5, 0)$ (c) $\ell m = 11$, $\mathbf{R} = (5, 0, 0)$. In each case the sum is shown as the solid line.

4.7 Results and discussion

There are a number of methods by which the validity of the expressions derived in the previous sections can be checked. Firstly the value of the lattice sum components $S_L(\mathbf{R})$ should be independent of the choice of split parameter μ. Figure (4.1) shows calculations of the lattice sums for a chain with spacing $a = 5$. As can be seen from the figures the total sum of the three terms is independent of μ.

Table (4.1) shows calculated values of $S(\mathbf{R})$ and the real, reciprocal and correction terms for differing chain geometries and values of the split parameter μ. Again the value of the lattice sum $S(\mathbf{R})$ is independent of the split parameter μ. The higher ℓ terms can also be checked by direct comparison to brute force summations of the corresponding $Y_L(r)/r^{\ell+1}$. This confirms that the $S_L(\mathbf{R})$ expressions give the correct results.

$\mathbf{r}$	a	μ	$S^{(1)}(\mathbf{r})$	$S^{(2')}(\mathbf{r})$	$S^{(3)}(\mathbf{r})$	$S(\mathbf{r})$
(0,0,0)	5	0.05	-2.06461372E-01	1.69228244E-05	-5.99146455E-01	-8.05590904E-01
(0,0,0)	5	0.15	-4.34551404E-01	8.38449663E-03	-3.79423997E-01	-8.05590904E-01
(0,0,5)	10	0.05	4.55387994E-02	-1.01315880E-02	-2.99573227E-01	-2.64166016E-01
(0,0,5)	10	0.15	2.46795973E-03	-7.69219772E-02	-1.89711998E-01	-2.64166016E-01
(1,0,0)	5	0.05	7.94040364E-01	1.61739544E-05	-6.09022831E-01	1.85033707E-01
(1,0,0)	5	0.15	5.85931694E-01	7.43748029E-03	-4.08335467E-01	1.85033707E-01

Table 4.1: Values for the real space sum ($S^{(1)}$), reciprocal space sum ($S^{(2')}$) and $g_{\|} = 0$ term ($S^{(3)}$) arising in the Ewald treatment of the lattice sum $S(\mathbf{r})$ for a periodic one-dimensional lattice $\mathbf{u}_{\|} = (0, 0, na)$, $n = \ldots, -2, -1, 0, 1, 2, \ldots$, for different vectors $\mathbf{r}$ and values of the Ewald split parameter μ.

Secondly for certain systems we are able to compare the Madelung potential directly to one calculated using alternative methods. In figure (4.2) we show a direct comparison between the electrostatic potential above a layer of charges calculated using the expressions here, treating the layer as a number of parallel chains of atoms, and with previous expressions [114] explicitly derived for two-dimensional charge distributions. The two methods give comparable results except near the edges of the array of chains, where the potential found from summing chain contributions fails to reproduce that of an infinite layer. The agreement within the body of the chains demonstrates that both methods give the correct potential where expected.

Figure (4.3) shows a similar calculation, in this case a direct comparison between the electrostatic potential above a layer of dipoles. Again the potential is calculated using the expressions here, treating the layer as a number of parallel chains of atoms, and with expressions [114] derived for two-dimensional charge distributions. As is the case with the point charge comparison, the two methods give comparable results within the array of chains. Indeed the similarity between the point charge and the dipole plots is striking. This similarity is not especially surprising, since with constant z the contributions for point charges and dipoles behave as $1/r$ and $1/r^3$ respectively, thus the dipole contribution drops off faster outside the region of the chains.

The agreement between the surface and chain arrays for both the point charge and dipole terms confirms that the expressions for one-dimensional charge distributions derived in this chapter give the correct electrostatic potential.

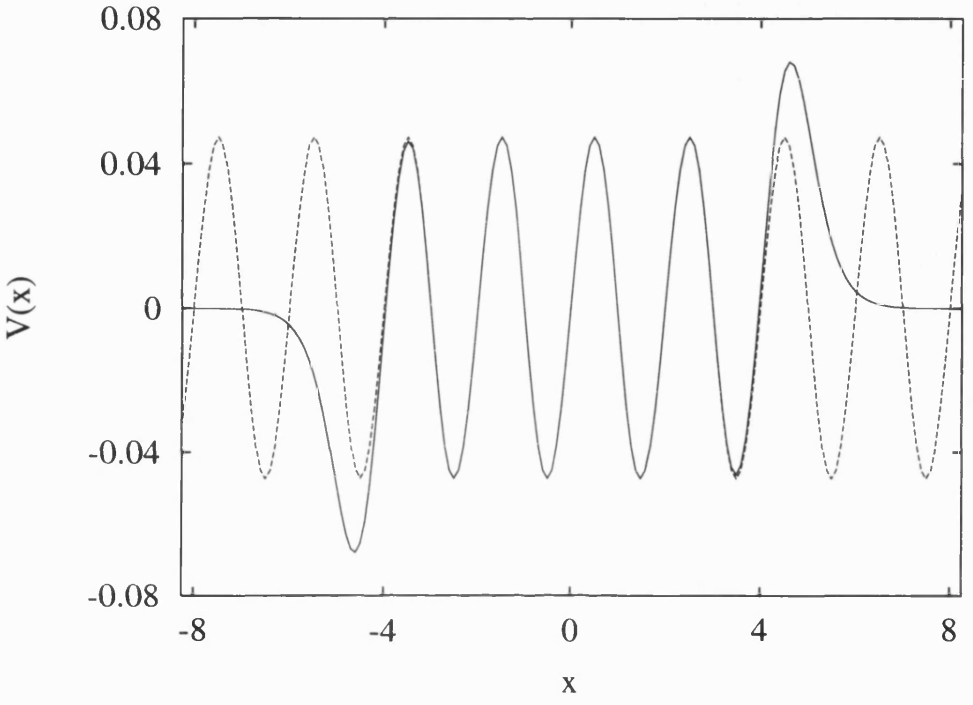

Figure 4.2: The electrostatic potential evaluated along a line $\mathbf{r} = 5(x, 0, 1)$, above a layer consisting of alternating charges arranged on a square lattice, with lattice sites $\mathbf{R}_{nm} = 5(n + 0.5, m, 0)$. Positive charges occupy sites with $n + m$ even. Dotted line: The potential is calculated using independent expressions [114] for two-dimensional charge distributions. Solid line: The potential is calculated for an array of 10 parallel monatomic chains (oriented along $\mathbf{y}$) modelling the same system, using the expressions derived in this chapter. The two methods agree except towards the edges of the array of chains, where the number of chains used to represent the layer becomes insufficient.

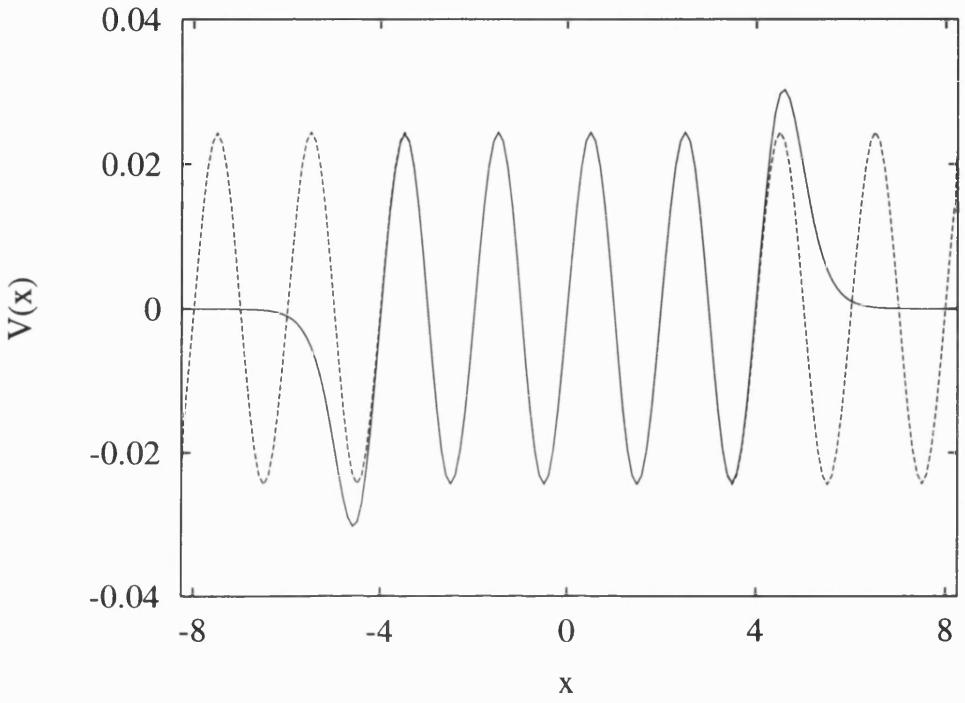

Figure 4.3: The electrostatic potential evaluated along a line $\mathbf{r} = 5(x, 0, 1)$, above a layer consisting of alternating dipoles arranged on a square lattice, with lattice sites $\mathbf{R}_{nm} = 5(n + 0.5, m, 0)$. Positive dipoles occupy sites with $n + m$ even. Dotted line: The potential is calculated using independent expressions [114] for two-dimensional charge distributions. Solid line: The potential is calculated for an array of 10 parallel monatomic chains (oriented along $\mathbf{y}$) modelling the same system, using the expressions derived in this chapter. The two methods agree except towards the edges of the array of chains, where the number of chains used to represent the layer becomes insufficient.

4.8 Laplace charge rebalancing scheme

In principle the Madelung potential derived in the preceding sections is valid only in charge neutral systems. That this is true can be seen by considering a sum of an infinite chain of atoms with non-zero net charge, which will clearly result in an infinite potential. As in the calculations described in the rest of this thesis the Fermi level is pinned to the value of the infinite substrate system, the defect system is not guaranteed to be charge neutral. Instead charge flows into and out of the defect region during the self-consistency iterations, with the eventual self-consistent system typically exhibiting charge neutrality to a good degree.

A similar situation exists in the 2D substrate calculations, where for surface calculations the Fermi level is pinned to the bulk value, resulting in charge neutrality not being guaranteed but emerging naturally. In the surface case the boundary condition used for the 2D Poisson solution is that the potential should be constant in vacuum and should match in amplitude on a surface between the interface region and the bulk half-space. Using this boundary condition, the solution of Poisson's equation has proved to be stable for small excesses/deficits of charge, and as the system is converged the potentials tend to minimise the charge imbalance. The discontinuity in derivative on the matching surface corresponds to a delta function sheet of charge, whose magnitude gives some measure of the adequacy of the surface region treated self-consistently. For the 1D defect calculations it is not necessarily the case that the system should be so well behaved with respect to charge imbalance. With this in mind several methods were developed to take into account any charge imbalance and improve the stability of the solution.

The method implemented was to match the amplitude of the potentials for the defect and substrate systems around some boundary enclosing the defect system. This is a similar boundary condition to that imposed in the 2D solution. The boundary is periodic in y with the same repeat unit as the chains, and is chosen to intersect with the next shell of atoms outside of the defect system, as shown in figure (4.4) for a 7 chain defect system.

For this boundary condition to be satisfied the potential due to the defect system (i.e., the potential due to the difference charge density between the system with and without the defect) must be equal to zero around the boundary. To determine

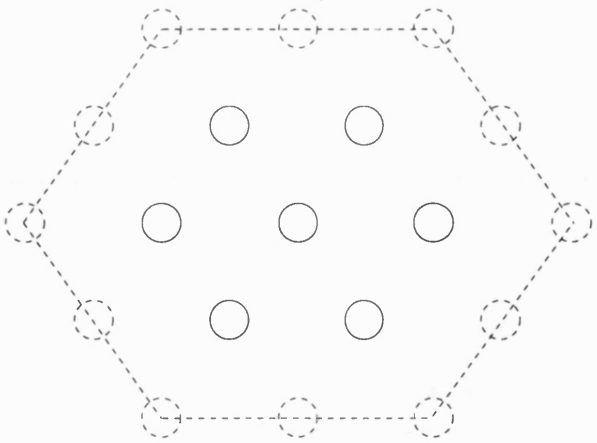

Figure 4.4: Diagram of 7 chain defect system showing the next shell of sites and the boundary used in the Laplace correction method. The cross-section is in the $x - z$ axes, with the chains parallel to the y-axis. The y-displacement of the boundary is chosen to coincide with the central layer of chains.

the necessary corrections to the potentials, we apply the following procedure:

1. Calculate the Madelung potential $V_{M,\mathbf{R}}$ due to the defect chains, for $\mathbf{R}$ spanning a set of points around the periodic boundary

2. Solve the Laplace equation subject to the same periodic boundary condition as the chains. Fit the coefficients of the Laplace solution to the Madelung potential around the boundary due to the defect system. Thus the solution of the Laplace equation corresponds to a potential around the boundary that matches the Madelung potential around the boundary due to the defect chains.

3. Calculate the potential from the Laplace solution at the centre of each defect site. Since the ASA Madelung contribution is equivalent to allowing the displacement within the defect sphere to go to zero (e.g., $\mathbf{r} \rightarrow 0$), we calculate the potential from the Laplace solution at the centre of each defect site.

4. For each defect site, subtract the potential from the Laplace solution at the centre of the site from the total electrostatic potential at that site, e.g.,

$$V_{M,\mathbf{R}} = V_{S,\mathbf{R}} + V_{D,\mathbf{R}} - V_{L,\mathbf{R}}, \tag{4.42}$$

   where $V_{S,\mathbf{R}}$, $V_{D,\mathbf{R}}$ and $V_{L,\mathbf{R}}$ are the substrate, defect and Laplace contributions to the potential at site $\mathbf{R}$.

For the second stage above we need to solve the Laplace equation

$$\nabla^2 V(\mathbf{r}) = 0 \tag{4.43}$$

subject to a boundary condition which is periodic in the y direction, so that $V(\mathbf{r}) = V(\mathbf{r}_\parallel + a\mathbf{y})$. Expanding the potential as

$$V(\mathbf{r}) = \sum_g V_g(\mathbf{r}_\parallel) e^{igy}, \qquad g = \frac{2\pi}{a} \tag{4.44}$$

we then have for all $\mathbf{r}$

$$\left(\nabla_\parallel^2 - g^2\right) V_g(\mathbf{r}_\parallel) = 0. \tag{4.45}$$

Converting to cylindrical polar coordinates we can expand the coefficients of the Fourier series as

$$V_g(\mathbf{r}_\parallel) = \sum_m V_{gm}(\rho) e^{im\phi}, \tag{4.46}$$

in which case the radial functions satisfy

$$\rho^2 V''_{gm}(\rho) + \rho V'_{gm}(\rho) - \left(\rho^2 g^2 + m^2\right) V_{gm}(\rho) = 0, \tag{4.47}$$

where the primes indicate differentiation with respect to ρ. With the condition that we require the potential to be regular at the origin we have the general solution

$$V(\mathbf{r}) = A_{00} + \sum_m{}' \left\{ A_{0m} \rho^m e^{im\phi} + \sum_g{}' A_{gm} I_m(gr) e^{im\phi} e^{igy} \right\}, \tag{4.48}$$

where the $I_m(gr)$ are incomplete Bessel functions [1].

The coefficients A_{gm} are determined by a least-squares fit to the potential on the boundary due to the defect chains. In calculations to date the contribution from the $g \neq 0$ terms has been found to be negligible, with the potential varying little with y along the boundary, so that only the $g = 0$ terms are significant.

Once the coefficients have been determined the value of the potential at the defect sites can be calculated. The Laplace potential at each defect site is then subtracted from the electrostatic potential at that site, as per step 4 above.

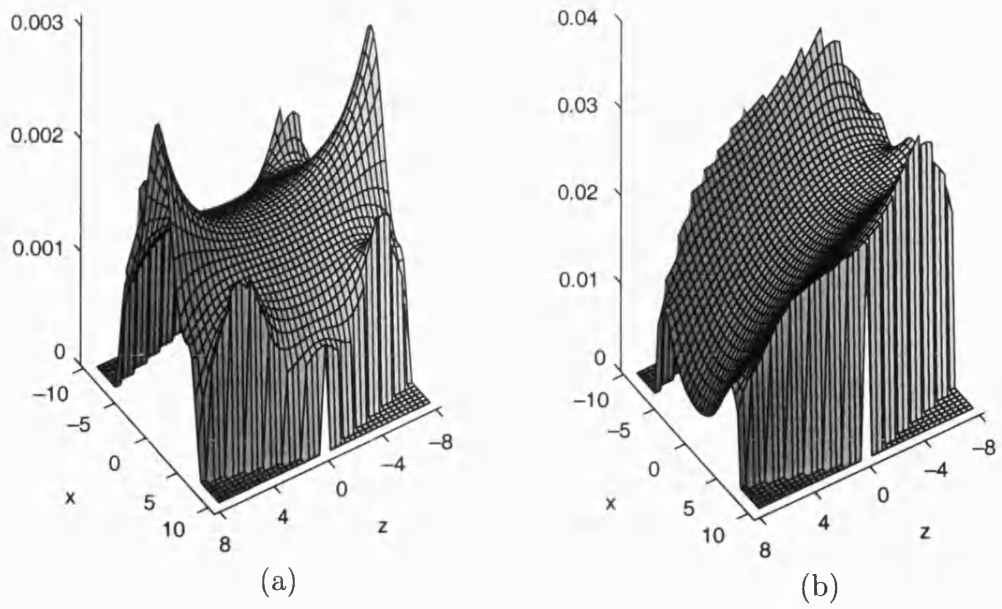

Figure 4.5: Plot of the potential correction term due to the Laplace boundary condition, V_L, over an $x-z$ cross-section up to the boundary for (a): a 7 chain Fe in bulk Cu defect calculation, and (b): a 7 chain Cu chain on Cu surface defect calculation. Positive z is pointing out of the surface in these plots.

Subtracting the Laplace term ensures that the substrate and defect potentials match on the boundary.

Figure (4.5) shows the Laplace potential over an $x-z$ cross-section up to the boundary for two 7 chain systems; Fe in bulk Cu and a Cu chain on a Cu surface respectively. These are calculated for fully converged potentials, and as expected exhibit the symmetry of the system.

We can examine the effect that this correction scheme has by comparing the convergence properties of defect chain calculations with and without the correction. This test considers a 7 chain defect calculation using 256 **k**-points and $\ell_{\max} = 3$. The system is a Cu chain on a Cu surface, with the initial potentials being identical to the clean surface case, excepting the central potential where the vacuum site is replaced by another Cu surface potential to give the chain on the surface. A mixing factor of 0.01 was used to generate the new potentials, and the Broyden scheme was employed, using up to 10 previous sets of potentials to accelerate the process. See chapter 2 for more details on the mixing parameters used in the self-consistency cycle.

Figure (4.6) shows the rate of convergence of the calculations, the difference

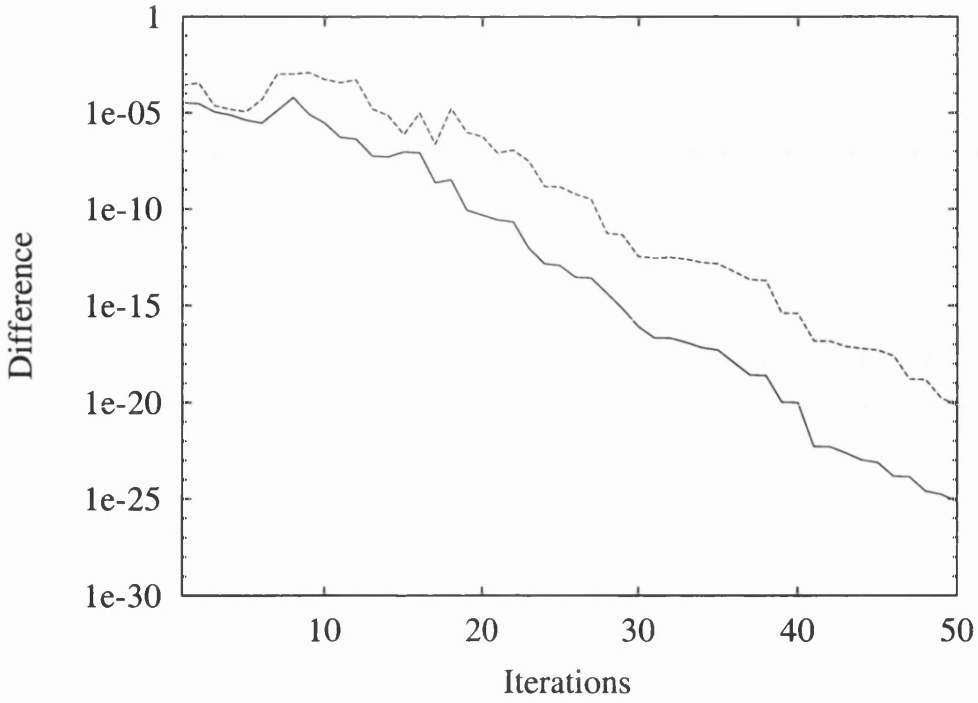

Figure 4.6: Plot of difference versus number of iterations for a Cu chain on Cu surface defect calculation. The solid line is from a calculation with the Laplace boundary condition implemented, the dashed line from one without.

being a measure of the change between the old and new potentials as defined in section 2.1. This clearly shows that the calculation with the Laplacian boundary condition converges at a faster rate, and experience has shown that in general the speed and stability of convergence is improved when using the Laplace boundary condition (LBC).

It should be noted that while the LBC speeds convergence, the converged potentials which are obtained will differ from those which would result if the condition is not used. It would therefore be desirable to examine the difference between the potentials obtained with and without the LBC, hopefully demonstrating that use of the LBC leads to more realistic converged potentials.

In order to do this we will compare the total charges on the defect sites for 7 and 19 chain systems converged with and without the LBC. As above, the system used is a Cu chain on a Cu surface, with 256 **k**-points and $\ell_{\text{max}} = 3$. The 7 chain system is illustrated schematically in figure (4.7), with the site indexing for the 19 chain system taken as referring to equivalent sites.

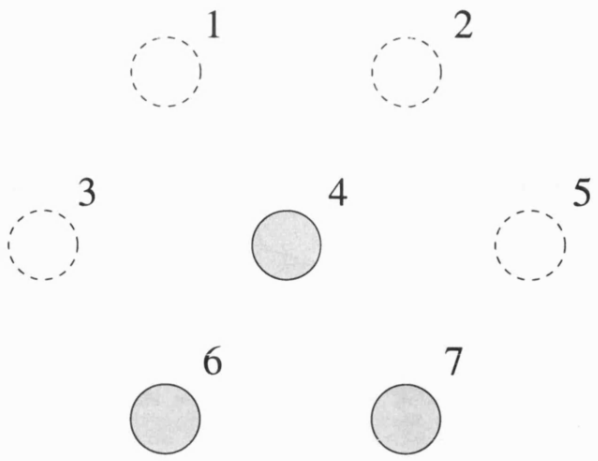

Figure 4.7: Diagram of a 7 chain Cu chain on Cu surface system, the Cu sites are shaded while the vacuum sites are indicated by broken lines. The numerical tags are used to refer to the sites in the charge comparison.

Table (4.2) compares the charge difference from the clean surface of the unique defect sites for the system converged with and without the LBC, for 7 and 19 chain clusters. Looking at the total charge error for the 7 chain systems, we see that the system converged without the LBC has a smaller charge error, the LBC system having lost charge as compared to the non-LBC system. Indeed, comparing the charge differences it is apparent that the system converged with the LBC has less charge on all sites than the system converged without the LBC. These results are to be expected, since if we were to increase the cluster size we would expect the charge around the outer shell of sites to give a positive contribution. The LBC system is effectively taking into account that some of the charge would escape from the defect cluster, while the non-LBC case simply minimises the charge error within the defect cluster.

If we examine the charge differences for the same sites in the 19 chain systems, we

	Charge difference from substrate			
	7 chain LBC	7 chain no LBC	19 chain LBC	19 chain no LBC
Site 1	0.11525	0.12026	0.11742	0.11921
Site 3	0.08662	0.08972	0.08549	0.08658
Site 4	-0.68434	-0.68052	-0.68366	-0.68248
Site 6	0.13080	0.13431	0.12740	0.12718
Total	-0.01901	0.00806	-0.01682	0.00415

Table 4.2: Comparison of the charge difference from the substrate for a Cu chain on Cu surface system, both with and without the LBC. Due to symmetry there are only four unique sites.

see broadly the same general behaviour. However in these systems the difference between the LBC and non-LBC systems is much reduced. This should not be surprising since with a larger chain cluster the perturbation due to the defect will be contained within the chain cluster to a greater extent. The potential due to the defect around the boundary would thus be smaller, resulting in a smaller LBC correction to the potentials on the defect sites. If we were to continue increasing the cluster size, we would expect the LBC and non-LBC potentials to converge.

Comparing between the 7 and 19 chain systems, we can see that in general the 7 chain LBC system gives charge differences that are closer to the 19 chain systems (both LBC and non-LBC). As we expect the larger chain system to give a more accurate treatment of the defect, this similarity suggests that use of the LBC not only improves convergence, but leads to converged potentials that represent a more realistic description of the defect system.

Chapter 5

Calculation and Convergence

5.1 Introduction

This chapter examines the details of applying the methods developed previously to perform calculations on one-dimensionally periodic defect systems, with the aim of demonstrating the viability of the method described in chapter 3 for electronic structure calculations.

We first consider calculation of the charge density from the Green function. This is important both as a necessary step in the self-consistency iteration and as a calculation of the electronic structure of converged potentials. We then examine the Brillouin zone integration, which involves integrating the $\mathbf{k}_\parallel$-resolved τ-matrices over the 2D Brillouin zone (BZ) to determine the real space τ-matrices.

The convergence of the substrate system with respect to the number of energy points used in the contour integral, n_E, is considered. Finally the convergence of chain calculations with respect to the choice of values for the various parameters is examined. Calculations are performed for Fe chains in bulk Cu, and Fe chains on a Cu surface, while the parameters examined are

- $n_{\mathbf{k}}$, the number of $\mathbf{k}$-points used in the BZ integral.
- $\ell_{\max}$, the maximum size of the partial wave basis set.

- n_{ch}, the number of chains included in the defect calculation.

5.2 Calculation of the charge density

The charge density is a closely related quantity to the Green function, and its evaluation is a necessary step in the self-consistency cycle. In order to obtain an expression for the charge density we use the standard relation [52]

$$\rho(\mathbf{r}; E) = -\frac{1}{\pi}\mathrm{Im}\, G(\mathbf{r}, \mathbf{r}; E) \tag{5.1}$$

where $\rho(\mathbf{r}; E)$ is the local density of states at $\mathbf{r}$ for energy E. From this quantity we can calculate the density of states at energy E via an integral over $\mathbf{r}$,

$$n(E) = \int \rho(\mathbf{r}; E)\, d\mathbf{r}, \tag{5.2}$$

and the charge density via an integral over the energy

$$\rho(\mathbf{r}) = \int^{E_f} \rho(\mathbf{r}; E)\, dE, \tag{5.3}$$

where E_f is the Fermi level. The above expressions are valid irrespective of the form of the potential and geometry of the system. Equation (5.2) allows us to define spatially partitioned densities of states – e.g., atom resolved, chain resolved, etc.– by varying the volume of integration. We will now consider in more detail the calculation of the charge density for ASA potentials, being those used in the calculations in this thesis.

From the expression for the Green function in (3.50) and the relation for the local density of states (5.1), and using $\rho^n(\mathbf{r}; E) = \rho(\mathbf{r}_n; E)$ where $\mathbf{r}_n = \mathbf{r} - \mathbf{R}_n$, we have

$$\begin{aligned}\rho^n(\mathbf{r}; E) =& \frac{2}{\pi}\mathrm{Im}\, i\kappa \sum_L Y_L(\mathbf{r}) Z^n_\ell(r) S^n_\ell(r') Y^*_L(\mathbf{r}') \\ &+ \frac{2}{\pi}\mathrm{Im}\, i\kappa \sum_{LL'} Y_L(\mathbf{r}) Z^n_\ell(r) \tau^{nn}_{LL'} Z^n_{\ell'}(r') Y^*_{L'}(\mathbf{r}').\end{aligned} \tag{5.4}$$

We can expand the charge density in spherical harmonics,

$$\rho^n(\mathbf{r};E) = \sum_L \rho_L^n(r) Y_L(\mathbf{r};E), \quad \rho_L^n(r;E) = \int Y_L^*(\mathbf{r})\rho^n(\mathbf{r};E)\,d\Omega, \tag{5.5}$$

which leads to an expression for the angular momentum components of the charge density [19]

$$\begin{aligned}\rho_L^n(r;E) =& \frac{2}{\pi}\sum_{L'} C_{LL'}^{L'} \mathrm{Re}\left[\kappa Z_{\ell'}^n(r) S_{\ell'}^n(r)\right] \\ &+ \frac{1}{\pi}\sum_{L'L''}\left(C_{LL'}^{L''} + C_{LL''}^{L'}\right)\mathrm{Re}\left[\kappa Z_{\ell'}^n(r)\tau_{L'L''}^{nn} Z_{\ell''}^n(r)\right] \\ &+ \frac{i}{\pi}\sum_{L'L''}\left(C_{LL'}^{L''} - C_{LL''}^{L'}\right)\mathrm{Im}\left[\kappa Z_{\ell'}^n(r)\tau_{L'L''}^{nn} Z_{\ell''}^n(r)\right]\end{aligned} \tag{5.6}$$

where the $C_{LL'}^{L''} = \int Y_L Y_{L'} Y_{L''}^*\,d\Omega$ are the Gaunt coefficients [97]. Note that equation (5.6) assumes a spin polarised system; for a spin degenerate system multiplication by a factor of 2 is necessary. The spherically symmetric contribution to the charge density is given by

$$\rho_{\mathrm{sph}}^n(r;E) = \frac{1}{\sqrt{4\pi}}\rho_{00}^n(r;E), \tag{5.7}$$

from which the total charge associated with site n at energy E, the density of states for site n, is found by integrating over the volume of the ASA sphere

$$n^n(E) = 4\pi\int_0^R r^2 \rho_{\mathrm{sph}}^n(r;E)\,dr. \tag{5.8}$$

The total charge density is found from the energy resolved charge density by integrating over occupied energies

$$\rho^n(\mathbf{r}) = \int_{-\infty}^{E_f} \rho^n(\mathbf{r};E)\,dE, \tag{5.9}$$

where E_f if the Fermi level. The Fermi level is determined in bulk calculations by charge neutrality, which requires that,

$$\sum_n \left(Z^n - \int_{-\infty}^{E_f} n^n(E)\,dE\right) = 0. \tag{5.10}$$

The Fermi level is found by repeated evaluation of the integral in equation (5.10) until charge neutrality is obtained to the required degree of accuracy.

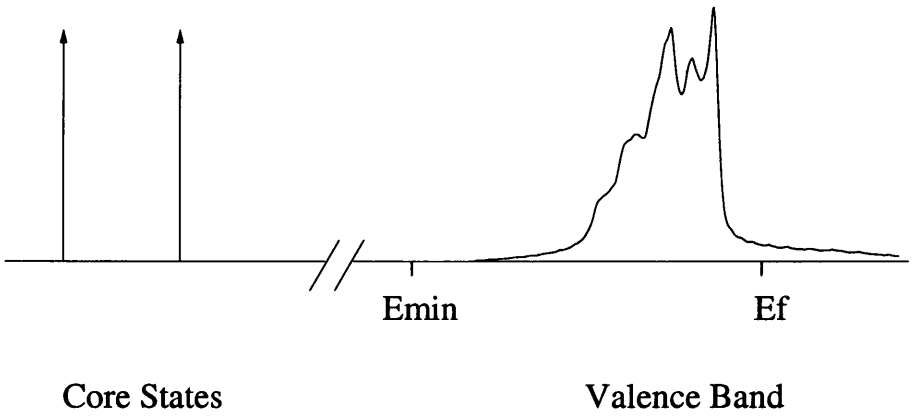

Figure 5.1: Diagram showing schematically the contributions to the energy integral from the core states and the valence band.

For practical reasons, the integral over occupied states is split into core and valence contributions, as shown in figure (5.1). The core levels are states with negligible dispersion, and can be treated as an atomic calculation. The contributions from these states can thus be calculated rapidly and the integral over the energy need only be calculated across the valence band. The valence contribution is found from an integral from the bottom of the valence band up to the Fermi level. For some materials the higher energy core states also exhibit significant dispersion. In these cases the valence band can be extended to include these states, or alternatively they can be treated by separate integrals over appropriate energy ranges.

As was discussed in section 3.10 describing the calculation of the half-space reflectivities, the layer doubling algorithm is not guaranteed to converge for real energies, necessitating a small imaginary component to the energy. This is not in practice a significant restriction, since the imaginary component can be arbitrarily small. There are, however, numerical advantages in including a significant imaginary component in the energy, as we will see below.

For the valence band integral the energy contour is deformed into the upper half of the complex energy plane, where the Green function is analytic. Cauchy's theorem shows the contribution from this contour is the same as that calculated along the real energy axis, providing the initial and final points are the same. Since the Green function is smoother as a function of energy for higher imaginary components of the energy, this allows accurate calculation of the integral with far fewer energy points required. This smoothing effect is illustrated in figure (5.2),

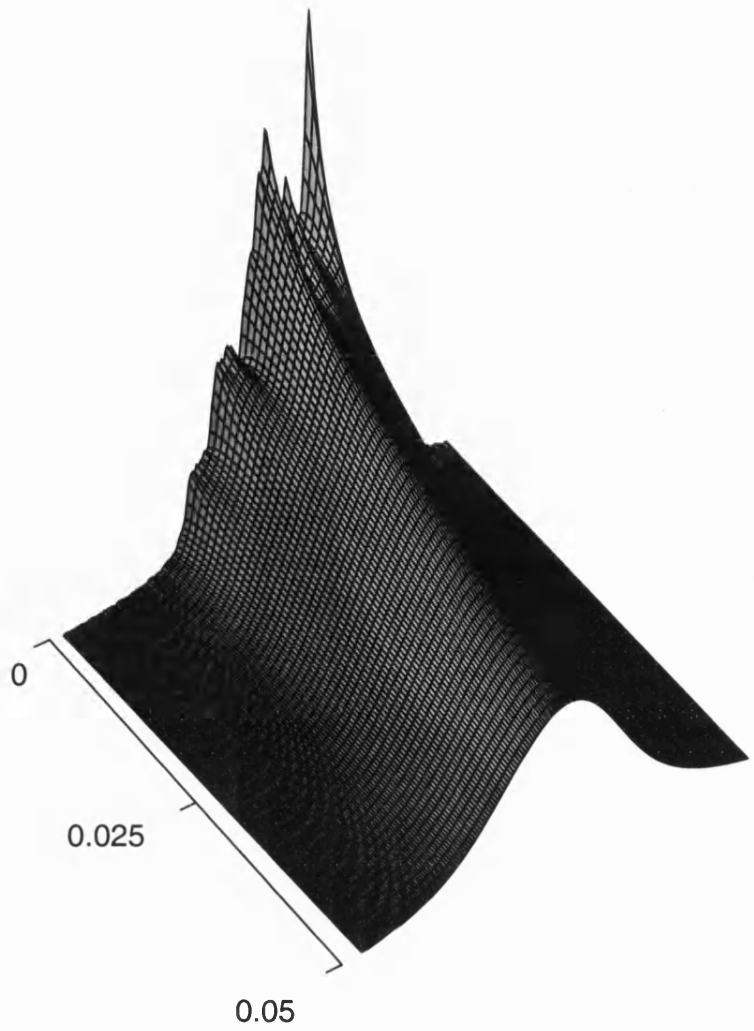

Figure 5.2: Density of states of bulk Cu as a function of complex energy, evaluated over an imaginary energy range between 0.001 Ha and 0.05 Ha, and a real energy range between 0.0 Ha and 0.4 Ha

showing the density of states as a continuous function of the imaginary energy component. As the density of states is directly related to the imaginary part of the Green function (from equation (5.1)), this demonstrates the smoothing of the Green function.

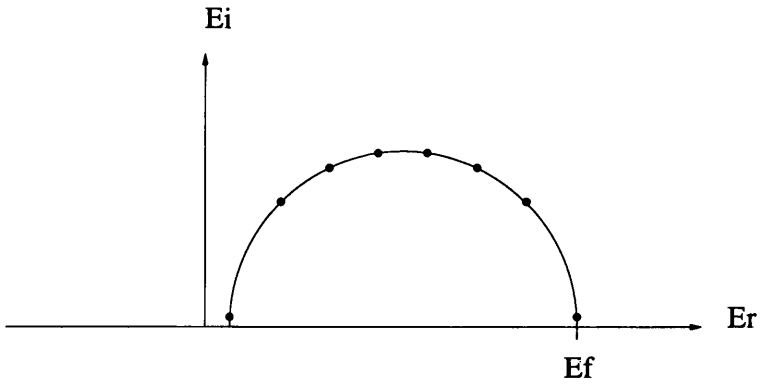

Figure 5.3: Diagram of the semi-circular energy contour used to evaluate the integral over the energy, with eight energy sampling points shown.

The contour is sampled with a Gaussian integration scheme, which avoids sampling the end points of the contour (where Im(E) = 0). A schematic diagram of the semi-circular contour used in the energy integration is shown in figure (5.3). This technique gives a fast and accurate integration scheme, with 16 energy sampling points used for the calculations in this work. Table (5.1) demonstrates the convergence of the energy integral, with Fermi levels for bulk Cu calculated using $\ell_{\max} = 3$ and 256 **k**-points. Since the Fermi level is determined by iteration of the energy integral until charge neutrality is obtained, this gives an indication of the accuracy of the energy integral. As can be seen from the table, 16 energy points samples the energy integral to a good degree of accuracy.

For surface/interface calculations, and defect calculations, the Fermi level is fixed to the bulk value. This is in contrast to supercell/slab methods, where the Fermi level is a floating variable. The same set of energy points is used in both the convergence of the substrate potentials as well as in the iterations of the defect system. This avoids any unwanted numerical effects by ensuring that the reference potentials are fully converged with respect to the parameters used in the defect calculation.

N_E	Bulk Cu E_f
8	0.314743
16	0.314987
32	0.314938
64	0.314939

Table 5.1: Fermi level calculated for bulk Cu, for varying numbers of energy points used to sample the integral. In each case the other parameters were $\ell_{\max} = 3$, 256 **k**-points and 25 **g**-vectors.

The multipole moments of the charge for site n, used in the Poisson solution, are defined as [59]

$$Q_L^n = \int_{\text{Cell}} r^\ell Y_L^*(\mathbf{r}) \rho^n(\mathbf{r})\, d\mathbf{r}, \tag{5.11}$$

where the integral is over the volume associated with site n. Hence for an ASA calculation, the multipoles are related to the angular momentum components of the charge density (5.6) by

$$Q_L^n = \int_0^R r^{\ell+2} \rho_L^n(r)\, dr, \tag{5.12}$$

where R is the sphere radius. The $\ell = 1$ multipoles, used in the Poisson solution, are obtained from (5.6), the first term of which is zero for $\ell = 1$, due to the vanishing Gaunt coefficient.

5.3 Brillouin zone integral

From (3.73), the $\mathbf{k}_\parallel$-resolved τ-matrix for an isolated layer can be written

$$\underset{\sim}{\tau}(\mathbf{k}_\parallel) = \left[\underset{\sim}{m} - \underset{\sim}{G}(\mathbf{k}_\parallel)\right]^{-1}. \tag{5.13}$$

This is related to the real space τ-matrix via equation (3.68), hence for the τ-matrix connecting sites n and m we have (omitting the undertilde for clarity)

$$\tau^{nm} = \frac{1}{\Omega_{2\text{D}}} \int \tau(\mathbf{k}_\parallel) e^{-i\mathbf{k}_\parallel \cdot (\mathbf{R}_n - \mathbf{R}_m)} d\,\mathbf{k}_\parallel, \tag{5.14}$$

where the integral is over the 2D Brillouin zone. This integral is numerically approximated by a weighted sum over a set of $n_\mathbf{k}$ $\mathbf{k}_\parallel$-points that span the first BZ,

$$\tau^{nm} \approx \sum_{i=1}^{n_\mathbf{k}} \alpha_i \tau(\mathbf{k}_{\parallel_i}), \tag{5.15}$$

hence we need only calculate the τ-matrix at this set of points over the 2D Brillouin zone. Increasing $n_\mathbf{k}$ results in a more accurate approximation. The same $\mathbf{k}_\parallel$-point set is used in both the substrate and defect calculations to avoid numerical effects (see later), as with the energy integral.

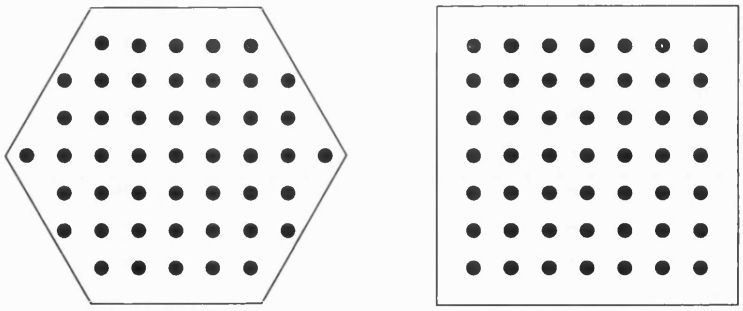

Figure 5.4: Examples of **k**-point sampling sets that could be used for hexagonal and square 2D Brillouin zones. The sampling set used for the square BZ has k_x independent of k_y, while the sampling set for the hexagonal BZ clearly has k_x dependent on k_y.

For one-dimensional defect calculations it is necessary to calculate and store the τ-matrices resolved in the direction of the defects, so for line defects parallel to the y-axis we need to calculate the k_y-resolved τ-matrices of the substrate system, which, for a general set of $\mathbf{k}_\parallel$-points, are given by

$$\tau^{nm}(k_y) = \int_{k_{\min}(k_y)}^{k_{\max}(k_y)} \frac{dk_x}{\Omega_x(k_y)} \tau(k_x, k_y) e^{-ik_x(X_I - X_J)}. \tag{5.16}$$

Note that for a general set of points, the range of the integral over x and the x-dimension of the 2D BZ will depend upon the value of k_y. Hence each $\tau(k_y)$ will be given by a sum of the contributions over the k_x points associated with that k_y. This is illustrated in figure (5.4), where possible sampling sets for a hexagonal and a square 2D Brillouin zone are shown. The hexagonal set clearly has k_x dependent on k_y, while the square set does not.

In order to reduce the number of points at which $\tau(\mathbf{k}_\parallel)$ need be calculated, and thus reduce computing time, symmetry is used to relate the τ-matrix contribution from one part of the 2D BZ to the rest. In the case of a square lattice, the τ-matrix need only be calculated for 1/8th of the 2D BZ, known as the irreducible wedge, which is related via mirror plane symmetries to the full τ-matrix.

For the standard LKKR calculations in this thesis, e.g., convergence of the substrate potentials, Cunningham's algorithm [23] is used to determine the set of **k**-points. Figures (5.5) and (5.6) show the first few of these sets for the square lattice (e.g., FCC(100) and BCC(100)) and the hexagonal lattice (e.g., FCC(111)) respectively.

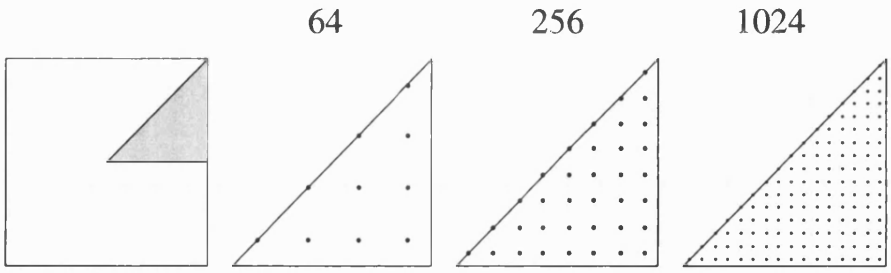

Figure 5.5: **k**-point sampling sets used for the irreducible 1/8th wedge of the square 2D Brillouin zone. The sets shown are for 64, 256 and 1024 **k**-points sampling the full Brillouin zone.

As mentioned above, for the defect calculations we need to calculate the k_y-resolved τ-matrix. Since the xy mirror plane relates different k_y points by symmetry, it is not possible to simply step through the k_y index accumulating $\tau(k_y)$ when using the 1/8th wedge **k**-point set. It is necessary to store in memory the contributions to the τ-matrix for each k_y value. This requirement increases the memory usage of the code by a factor of ikym/2, where ikym is the number of unique k_y values used.

With this in mind, for the square lattice two versions of the code were implemented, one using the 1/8th wedge **k**-point set and one that uses a 1/4th wedge **k**-point set, the first few of which are shown in figure (5.7). The 1/8th wedge code samples less points in the 2D BZ, and hence runs faster, however for large cluster sizes and high values of $\ell_{\max}$ the memory requirements become prohibitive, and necessitate using the slower 1/4th code. Both sets used match the points given by Cunningham's algorithm [23].

The substrate potentials are converged self-consistently with a given set of **k**-points. The same set of **k**-points are then used to calculate and store the τ-matrices, hence the defect calculation uses the same **k**-point set. This ensures

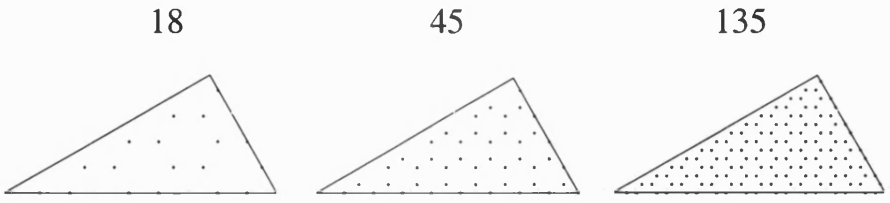

Figure 5.6: **k**-point sampling sets used for the irreducible 1/12th wedge of the hexagonal 2D Brillouin zone. The sets shown are for 18, 45 and 135 **k**-points within the 1/12th wedge.

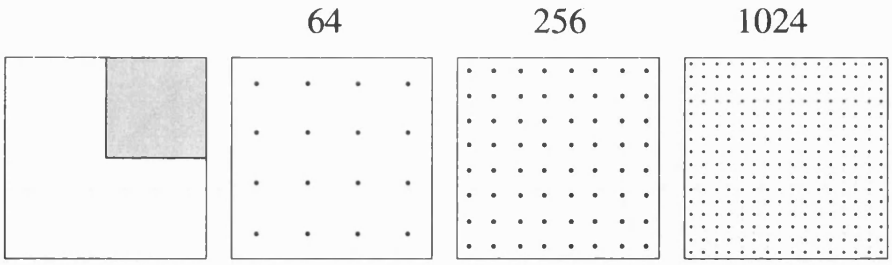

Figure 5.7: **k**-point sampling sets used for the 1/4th wedge of the square 2D Brillouin zone. The sets shown are for 64, 256 and 1024 **k**-points sampling the full Brillouin zone.

that the reference potentials used in the defect calculation are converged with respect to the **k**-point set, thus for a null defect test (e.g., inserting a Cu chain in bulk Cu) the potentials will converge to match the substrate potentials.

The integral over k_x is performed in the substrate calculation, hence the τ-matrices that are calculated and stored are k_y-resolved. This means that for each iteration of the defect system, it is only necessary to integrate over k_y, hence the computing time scales linearly with the number of k_y points included.

As mentioned in the previous section, as the magnitude of the imaginary component of the energy increases the charge density becomes smoother as a function of energy, and thus requires less energy points to sample effectively. This effect is also significant in the Brillouin zone integration, as the charge density, and therefore the τ-matrix, is smoothed across the 2D BZ (note that the only contribution to the charge density which varies with $\mathbf{k}_{\|}$ is the τ-matrix). Hence less **k**-points are required to accurately sample the 2D BZ for higher values of the imaginary component of the energy. For systems where very large **k**-point sets are needed near the real energy axis it becomes convenient to vary the **k**-point set with energy (see e.g., [4]).

5.3.1 τ-matrix symmetry

Due to the mirror plane symmetries present in the 2D lattice we can relate the τ-matrix contributions from one segment of the 2D BZ to the others. For a square 2D lattice we have x, y and xy mirror planes. From the definition of the angular momentum matrix elements of the τ-matrix [46],

$$\tau_{LL'}^{nm} = \iint j_\ell(\kappa r) Y_L(\mathbf{r}) \tau^{nm}(\mathbf{r}, \mathbf{r}') j_\ell(\kappa r') Y_L^*(\mathbf{r}') \, d\mathbf{r} \, d\mathbf{r}', \tag{5.17}$$

we can determine the symmetry relations for the real space τ-matrix elements due to the x, y and xy mirror planes respectively:

$$\tau_{LL'}^{nm} = \tau_{\ell -m \; \ell' -m'}^{nm}, \tag{5.18}$$

$$\tau_{LL'}^{nm} = \tau_{\ell -m \; \ell' -m'}^{nm} (-1)^{m+m'}, \tag{5.19}$$

$$\tau_{LL'}^{nm} = \tau_{\ell -m \; \ell' -m'}^{nm} (-1)^{m+m'} i^{m'-m}. \tag{5.20}$$

The reciprocal space contributions to the τ-matrix are related to the real space τ-matrix by equation (5.14), hence the symmetry relations connecting contributions in the 2D BZ will include phase factors due to the exponential term. Thus we have the following symmetry relations for the τ-matrix contributions from points in the 2D BZ of a square lattice:

$$\tau_{LL'}^{nm}(-k_x, k_y) = \tau_{\ell -m \; \ell' -m'}^{nm}(k_x, k_y) e^{-2ik_x X_{nm}}, \tag{5.21}$$

$$\tau_{LL'}^{nm}(k_x, -k_y) = \tau_{\ell -m \; \ell' -m'}^{nm}(k_x, k_y) (-1)^{m+m'} e^{-2ik_y Y_{nm}}, \tag{5.22}$$

$$\tau_{LL'}^{nm}(k_y, k_x) = \tau_{\ell -m \; \ell' -m'}^{nm}(k_x, k_y) (-1)^{m+m'} i^{m'-m} e^{-i(k_x - k_y)(X_{nm} - Y_{nm})}. \tag{5.23}$$

These relations allow the contribution from the full 2D BZ to be assembled from that of the 1/8th wedge.

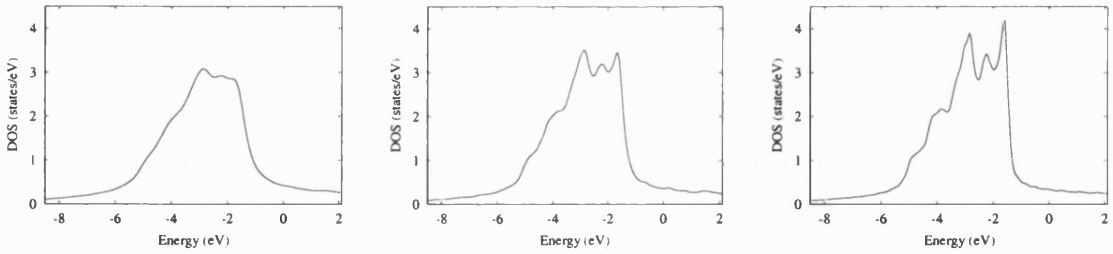

Figure 5.8: Bulk Cu DOS calculated using (a) Im(E) = 0.01 Ha, (b) Im(E) = 0.005 Ha, and (c) Im(E) = 0.0025 Ha. The same bulk potential was used in each case, converged with $\ell_{\max} = 3$ and 256 **k** points. 1024 **k**-points and 200 energy points were used in the DOS calculation.

5.4 Density of states calculations

In calculating the density of states we need to evaluate equation (5.8) over the desired energy range. The value of the imaginary component of the energy used will determine the level of smoothing in the density of states. For energy $E + i\Gamma$ the density of states is given by the convolution of the real energy density of states and a Lorentzian of half width Γ. Thus structure in the density of states smaller than Γ is lost. However decreasing Γ requires more energy points to sample the integral accurately, and a larger **k**-point set for the integral over the 2D BZ. Note that the **k**-point set used in DOS calculations need not be the same as that used in converging the potentials, since the size of **k**-point set required is dependent on the magnitude of the imaginary energy.

Figure (5.8) demonstrates the effect of the choice of Im(E) upon the calculated DOS of bulk Cu. In the first plot, with Im(E) = 0.01 Ha, the DOS is nearly featureless. Increasing amounts of structure can be observed in the DOS as Im(E) is reduced to 0.005 Ha in the second plot, and then to 0.0025 Ha in the third, which is clearly recognisable as a Cu density of states.

For defect DOS calculations the substrate τ-matrices are not stored, since the resulting files become unmanageably large due to the number of energy points and the generally higher **k**-point set used. The τ-matrices are instead calculated for each energy point and used to calculate the DOS of the defect system at that energy. Since DOS calculations are not iterated in the same manner as the self-consistency calculations, storage of the τ-matrices is less significant.

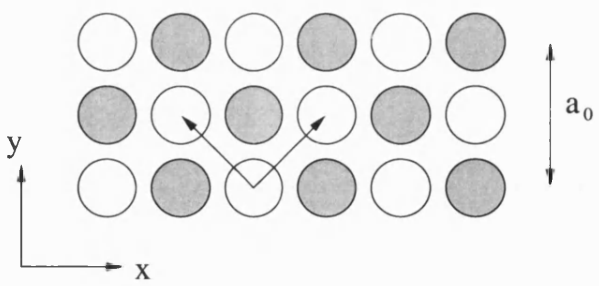

Figure 5.9: Diagram of the FCC(100) structure. The shaded atoms are displaced by a0/2 into the z-plane. As the arrows illustrate, this structure can be viewed as stacks of square lattices mapped out by the vectors $\mathbf{a}_1 = -1/\sqrt{2}\mathbf{x} + 1/\sqrt{2}\mathbf{y}$ and $\mathbf{a}_2 = 1/\sqrt{2}\mathbf{x} + 1/\sqrt{2}\mathbf{y}$.

5.5 Substrate calculations

The substrate system used in these demonstration calculations is Cu. The structure of Cu is FCC, and within the LKKR calculations is viewed as made up of stacked layers of square 2D lattices, as shown in figure (5.9). Figure (5.10) shows a three-dimensional view of a FCC(100) slab, with the central of the three z-layers shaded for clarity.

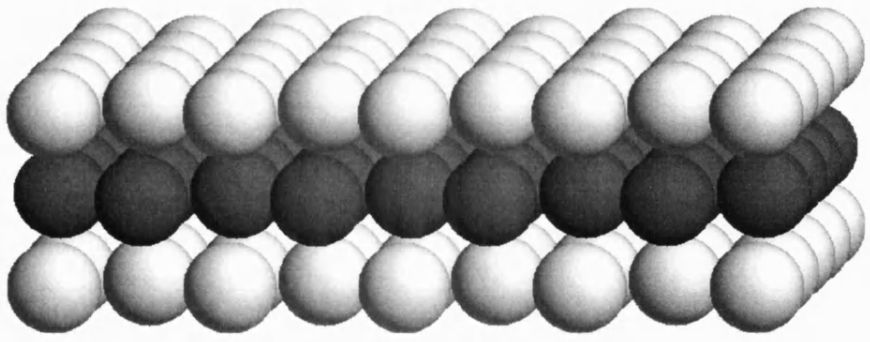

Figure 5.10: FCC(100) structure, the central layer is shaded to emphasise the partitioning of the system into a stack of square 2D lattices.

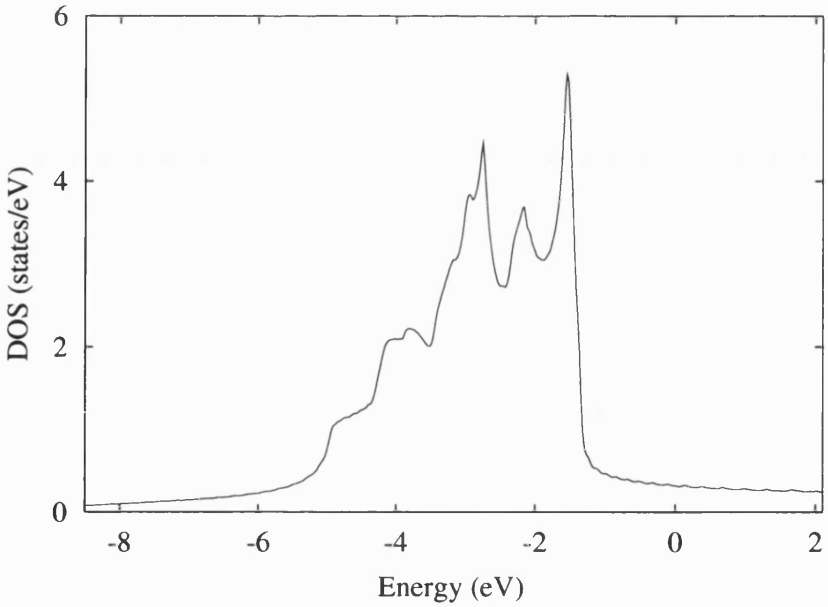

Figure 5.11: Density of states for bulk Cu. Converged with $\ell_{\max} = 3$, $n_{\mathrm{k}} = 256$. In the DOS calculation 500 energy points and 4096 **k**-points were used, with Im(E) = 0.001 Ha.

The x/y and z axes correspond to the $\langle 110 \rangle$ and $\langle 001 \rangle$ directions respectively. For the surface calculations the Cu(001) surface was used, with the z-axis normal to the surface and positive z pointing out of the surface. The substrate surface systems were converged with 3 vacuum layers and 4 Cu layers in which the potentials were permitted to relax. The potentials for both bulk and surface systems were converged self-consistently using the LKKR method, with 16 energy points in the contour integral, and 25 g-vectors in the plane wave basis set. Potentials were converged with values of n_{k} and $\ell_{\max}$ corresponding to those used in the defect calculations. Figure (5.11) shows a calculation of the density of states for bulk Cu, showing good agreement with the literature [87]. For further details of LKKR calculations see [19].

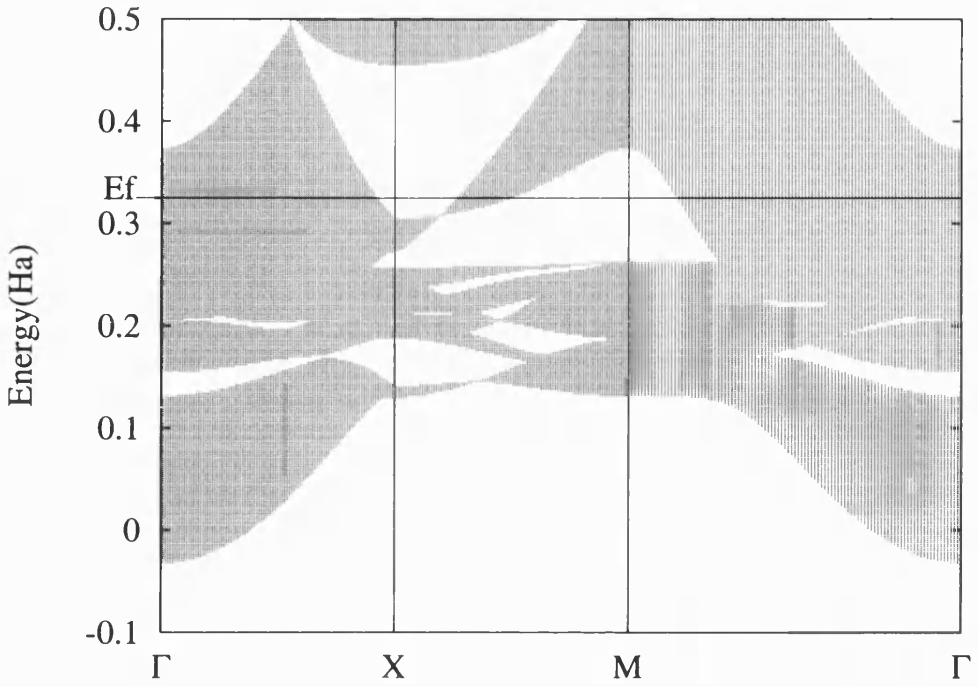

Figure 5.12: Projected band structure of bulk Cu. Converged with $\ell_{\max} = 2$, $n_{\mathrm{k}} = 64$.

5.5.1 Projected band structure

For systems with 2D symmetry, e.g., surfaces, we can view the system as having a unit cell which is infinitely large in the direction normal to the surface. This results in a surface Brillouin zone (SBZ), characterised by 2D wave vectors $\mathbf{k}_{\|}$. For every value of $\mathbf{k}_{\|}$ we have a rod of $k_{\perp}$ extending through the infinite 3D Brillouin zone, the band structure along this rod can then be projected onto the SBZ. This allows the identification of those values of E and $\mathbf{k}_{\|}$ for which extended states are permitted. States which occur outside of these regions will be unable to couple to solutions in the bulk, and therefore represent localised states [132].

The projected band structure for bulk Cu is shown in figure (5.12). This was calculated by evaluating the DOS along the high symmetry lines in the 2D Brillouin zone. The values of E and $\mathbf{k}_{\|}$ for which the DOS was equal to zero correspond to regions where there are no extended states. Figure (5.12) shows good agreement with the projected band structure of bulk Cu calculated elsewhere [100, 15].

5.6 Chain systems

In a chain defect calculation the potentials are permitted to vary over a finite number of 1D unit cells, or chains. Physically, one expects the important perturbations due to a chain defect to be localised in the vicinity of the defect. Hence we expect that the chains closest to the defect will experience the greatest perturbation, and that as we add more distant chains to the cluster, these will exhibit smaller changes in their potentials. This localisation of the perturbation due to a defect chain justifies the use of a finite cluster of varying chains in the defect calculation. In bulk calculations one would expect the effects of the defect to decay uniformly irrespective of the direction through the solid, hence a cylindrical cluster of chains would be best to model the system. In the case of a chain on a surface however, perturbations are likely to be more significant parallel and into the surface, rather than extending into vacuum, where there are relatively few electrons.

The system can thus be thought of as being constructed from a cluster of such chains embedded in a substrate system, as shown in figure (5.13). The chains are taken to be parallel to the y-axis, thus run along the $\langle 110 \rangle$ direction. Chains on the (001) surface are taken to occupy the ideal adatom sites along the $\langle 110 \rangle$ direction, i.e., there is no lattice distortion considered. Cluster geometries are chosen to include various shells of nearest and next nearest neighbour chains; clusters of 7, 19 and 37 chains are compared later in this chapter. For systems with even numbers of central chains, e.g., 2 chains on a surface, clusters of 10 and 24 chains were used to preserve $\pm x$ symmetry. Figure (5.14) shows a cross-section view of the geometries used. Note that alternate layers in the z-direction are offset by $a_0/\sqrt{2}$ in the x and y directions, in order to model the FCC structure.

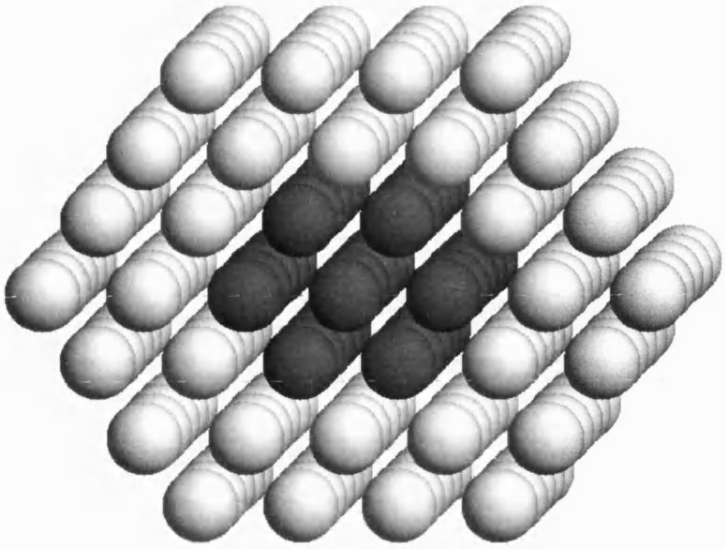

Figure 5.13: FCC(100) structure, viewed as being made up of clusters of chains in the $\langle 110 \rangle$ direction. The shaded central cluster represents those chains whose potentials are permitted to vary in a 7 chain defect calculation.

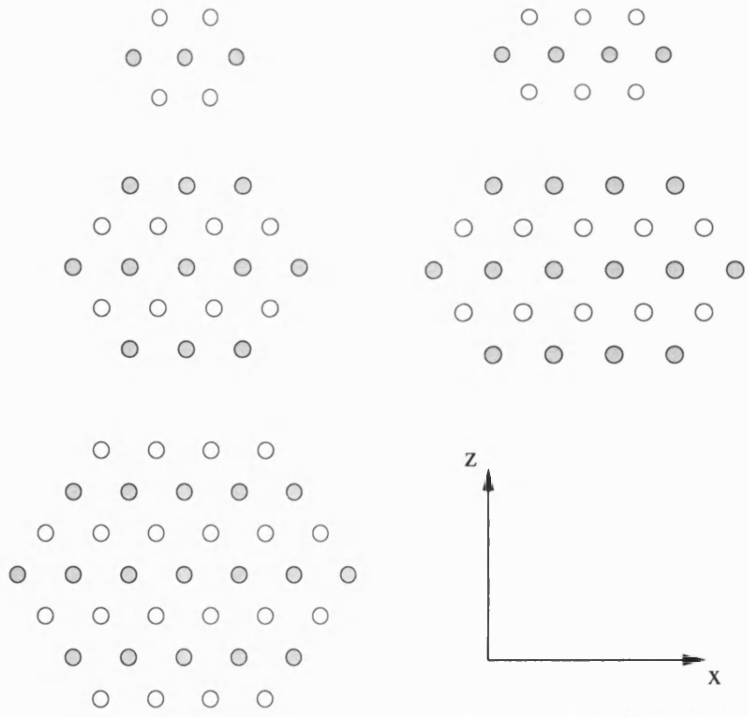

Figure 5.14: Cross-sectional schematic of the cluster geometries used, with chains taken to be running parallel to the y-axis. Clusters of 7, 19, 37, 10 and 24 chains are shown. The shaded sites are offset $a_0/\sqrt{2}$ into the y-plane.

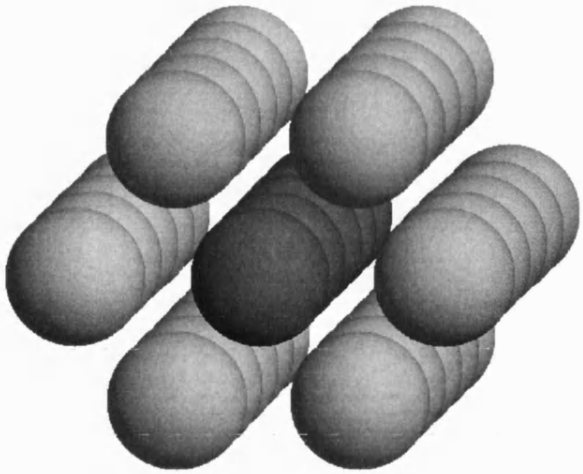

Figure 5.15: 7 chain Fe in bulk Cu system. The lighter spheres indicate Cu potentials, while the darker central chain is Fe.

5.7 k-point set convergence

This section deals with the convergence of the calculations with respect to the number of **k**-points used in the Brillouin zone integral. Note that this refers to the BZ integral performed for each iteration in order to obtain converged self-consistent potentials. For the DOS calculations in this section 1024 **k**-points were found to give sufficiently accurate results, with Im(E) = 0.0025 Ha and 200 energy points. For smaller values of Im(E) the resolution of structure in the DOS would improve, at the cost of requiring more **k**-points and energy points. In order to examine the convergence with respect to the **k**-point set, we will examine DOS calculations of 1D defect systems converged using 64, 256 and 1024 **k**-points. The other parameters in the convergence calculations are kept constant, with $\ell_{\text{max}} = 3$ and 16 energy points in the contour.

The first system we will examine is a 7 chain bulk Cu cluster, where the central chain has been replaced with Fe. This system is illustrated in figure (5.15). In this figure only those potentials which are permitted to vary are shown, the cluster of chains is embedded in an infinite substrate of bulk Cu chains which are not shown.

Figure (5.16) shows the LDOS of the central chain in a 7 chain bulk Cu cluster, where the central chain has been replaced with Fe. Both majority and minority spins are shown, with the upper panel showing the majority spin DOS. As can be

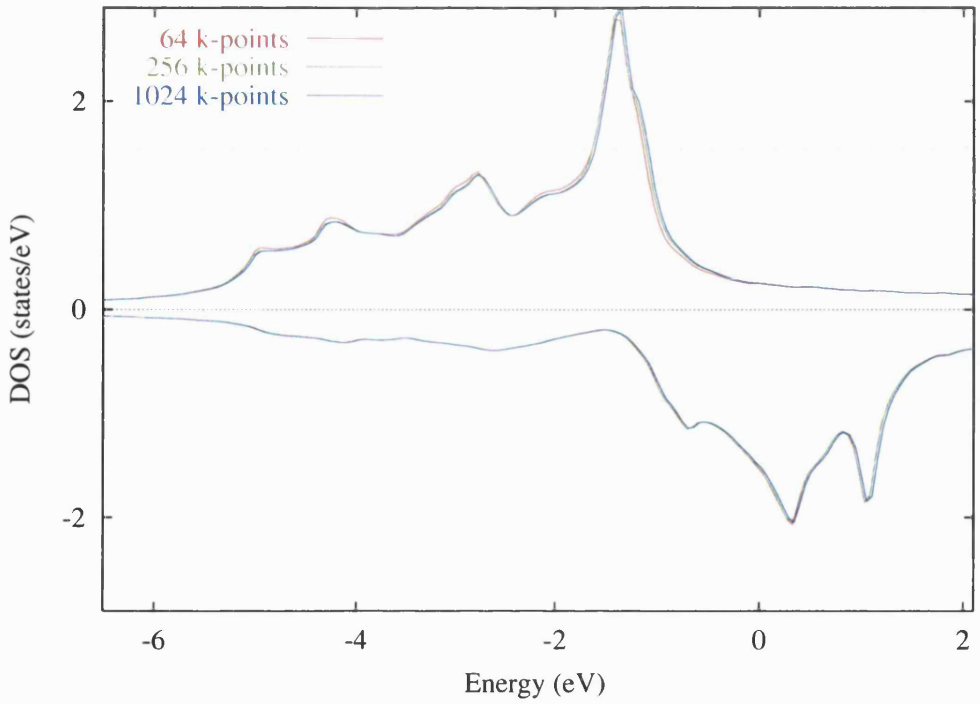

Figure 5.16: Spin polarised DOS for an Fe chain embedded in bulk Cu, comparing calculations with 64, 256 and 1024 **k**-points. The upper panel shows the majority spin DOS and the lower panel the minority spin DOS.

seen in figure (5.16), there are noticeable differences in the DOS in going from 64 to 256 **k**-points. In the comparison between 256 and 1024 **k**-points however, there is little change. This is taken to indicate that the 256 **k**-point set is sufficiently converged to produce accurate results in the density of states.

In order to verify this we will also consider a surface chain calculation. In this case the background system is a Cu surface, while the central chain, originally vacuum, has been replaced with Fe to give an Fe adchain on a Cu surface, this system is illustrated in figure (5.17). Again only those potentials which are permitted to vary are shown, the cluster of chains is embedded in a surface which extends to infinity in the $x-y$ plane. Figure (5.18) shows the LDOS of the central chain of this 7 chain system, the central chain being the Fe adchain on the surface. From figure (5.18), the same general behaviour as before can be seen with respect to variation of the **k**-point set, supporting the conclusion that 256 **k**-points are sufficient to converge the DOS. The density of states provides a good measure of **k**-point convergence, being more sensitive than integrated quantities like total charges and magnetic moments.

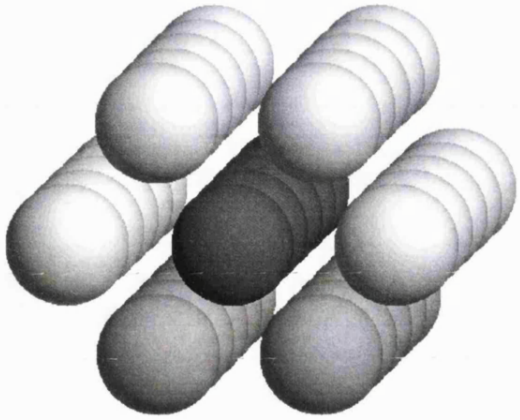

Figure 5.17: 7 chain Fe adchain on Cu surface system. White spheres indicate vacuum sites, with the light grey sites as Cu and the dark grey central chain as the Fe adchain.

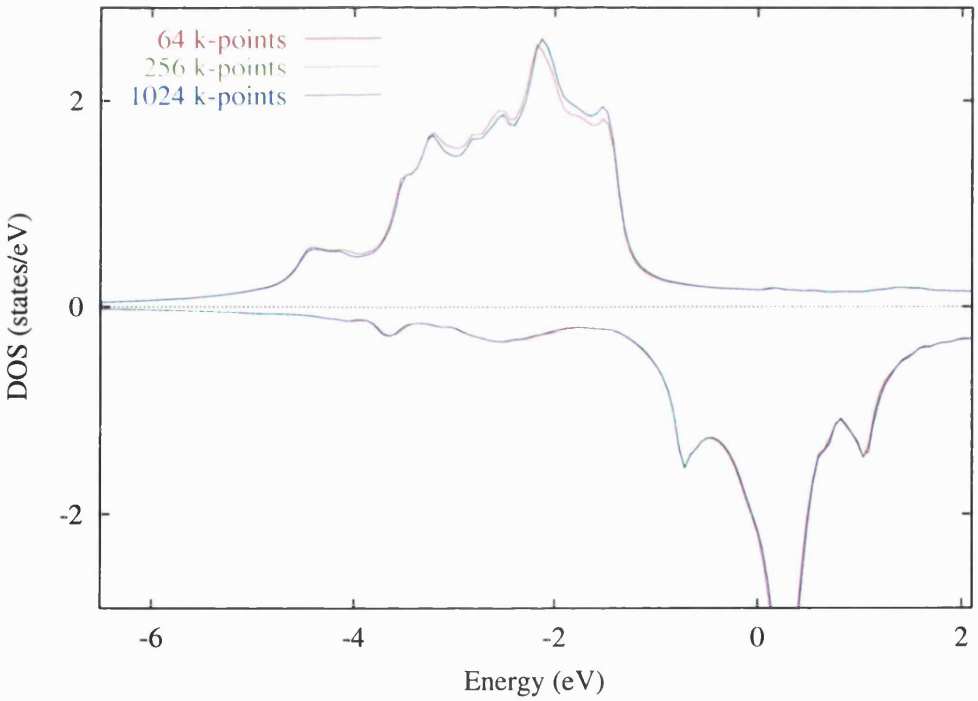

Figure 5.18: DOS for an Fe adchain on a Cu surface, comparing calculations with 64, 256 and 1024 **k**-points. The upper panel shows the majority spin DOS and the lower panel the minority spin DOS.

5.8 $\ell_{\max}$ convergence

We now consider convergence of the calculations with respect to the partial wave basis set. In principle, the angular momentum expansions are infinite, however in practice the terms become less significant with increasing ℓ, hence the expansions can be curtailed at some cut-off value, allowing the practical use of the expressions.

That the contributions from higher ℓ terms become less significant can be understood from considering the radial Schrödinger equation (3.3). For a given r the $\ell(\ell+1)/r^2$ term becomes increasingly repulsive with increasing ℓ. This acts as a centrifugal barrier with the result that the single site t-matrices become less significant for higher ℓ. As the multiple scattering terms are constructed using the t-matrices, this leads to the convergence of the angular momentum expansions.

The convergence with respect to the angular momentum cut-off is examined in this section, with calculations using values of $\ell_{\max} = 2, 3, 4$ being compared. The other parameters are kept constant, with all potentials converged using 256 **k**-points and 16 energy points in the contour. The DOS calculations were performed using 1024 **k**-points, 200 energy points and Im(E) = 0.0025 Ha.

We will first examine the 7 chain Fe in bulk Cu system referred to above and illustrated in figure (5.15). This is a 7 chain bulk Cu cluster, with the central chain replaced by Fe. Figure (5.19) shows the LDOS of the Fe central chain for differing values of $\ell_{\max}$. It is clear from figure (5.19) that the DOS calculations are converging with respect to the value of $\ell_{\max}$, the difference between the calculations for $\ell_{\max} = 2$ and $\ell_{\max} = 3$ is considerably more pronounced than that between the $\ell_{\max} = 3$ and $\ell_{\max} = 4$ calculations. As expected, the higher $\ell_{\max}$ components become increasingly less significant.

We will also consider $\ell_{\max}$ convergence in a surface chain calculation. For this calculation the background system is a Cu surface, while the central chain, originally vacuum, has been replaced with Fe to give an Fe chain on a Cu surface, as illustrated previously in figure (5.17).

Figure (5.20) shows the LDOS of the Fe adchain in this surface system for differing values of $\ell_{\max}$. The behaviour with respect to $\ell_{\max}$ for the Fe surface chain in figure

ℓ_{max}	Magnetic moment (μ_B) Fe in bulk Cu	Fe on Cu surface
2	2.492	2.922
3	2.604	2.989
4	2.645	3.013

Table 5.2: Magnetic moments for an Fe chain in bulk Cu and an Fe chain on Cu surface systems, for varying values of ℓ_{max}.

(5.20) is similar to that for the Fe chain in bulk in figure (5.19); demonstrating that the calculations are converging with increasing ℓ_{max}.

As further evidence of this behaviour, table (5.2) shows the magnetic moment of the central chain in the two systems described above, for differing values of ℓ_{max}. The behaviour of the moment with ℓ_{max} is consistent with that described above for the DOS, showing a tendency to converge with increasing ℓ_{max}.

In light of these results we take $\ell_{max} = 3$ as sufficiently converged, and used as the standard throughout the rest of this thesis. The relatively minor improvements in going to $\ell_{max} = 4$ need to be offset against the considerable increase in computing resources required, in particular with the size of the stored τ-matrices scaling as $(\ell_{max} + 1)^4$.

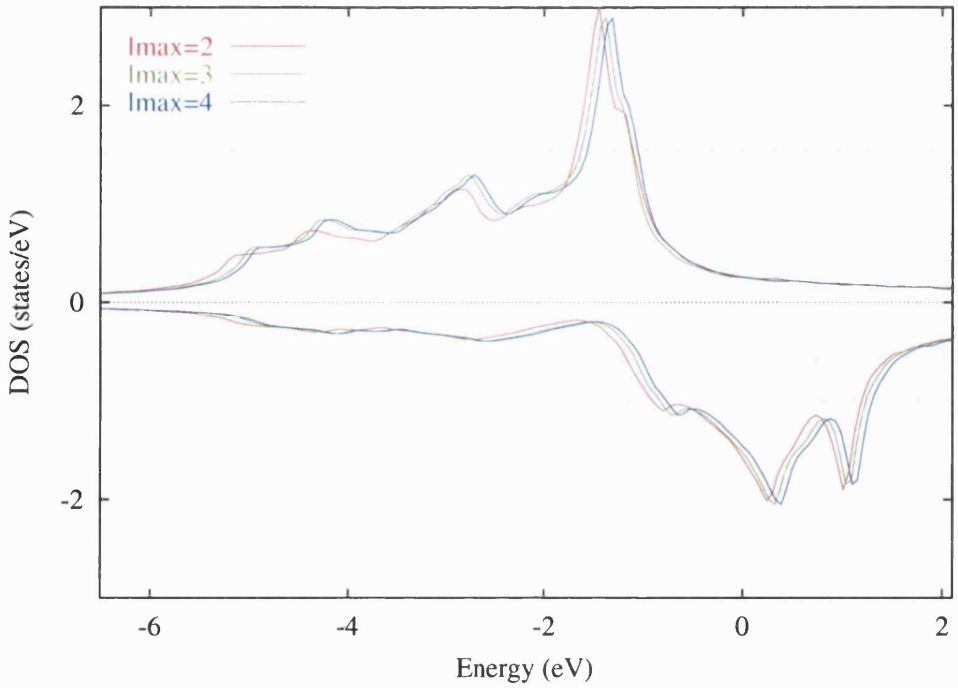

Figure 5.19: Spin polarised DOS for an Fe chain embedded in bulk Cu, comparing calculations with $\ell_{\max} = 2, 3$ and 4. The upper panel shows the majority spin DOS and the lower panel the minority spin DOS.

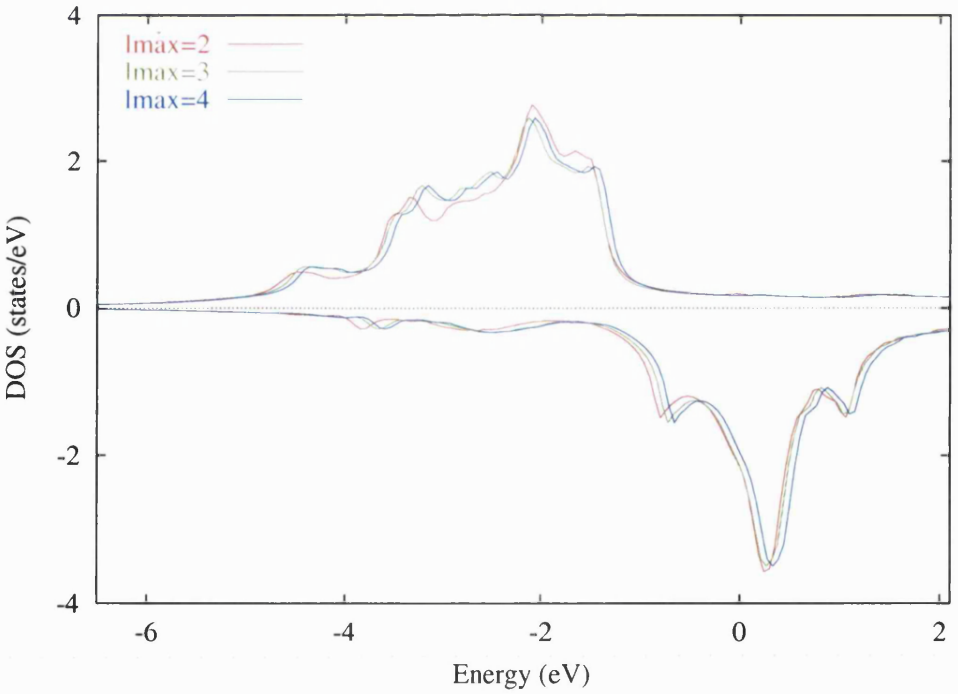

Figure 5.20: Spin polarised DOS for an Fe chain on a Cu surface, comparing calculations with $\ell_{\max} = 2, 3$ and 4. The upper panel shows the majority spin DOS and the lower panel the minority spin DOS.

5.9 Cluster size convergence

The number of chains whose potentials are allowed to vary in the defect calculation, n_{ch}, is the final parameter we consider. The chain systems are made up of a cluster of chains whose potentials can vary, embedded in an unvarying substrate system. Ideally we would include sufficient chains in the cluster such that the outermost chain potentials match to the substrate potentials. The perturbation to the potentials caused by the defect would then be wholly contained in the cluster. However, for many systems this would require an unfeasibly large cluster of chains, given that calculation time and memory usage scale as ${n_{\mathrm{ch}}}^2$.

This section will examine the convergence of the defect potentials for systems of 7, 19 and 37 chain clusters. To determine convergence we will examine DOS calculations, total charges and magnetic moments. The other parameters in the calculations are fixed, with potentials converged using 256 **k**-points, $\ell_{\mathrm{max}} = 3$ and 16 energy points in the contour. In the density of states calculations 1024 **k**-points were used, with 200 energy points and Im(E) = 0.0025 Ha.

Whilst convergence with respect to cluster size is in principle system dependent, the results in this section give an indication of convergence for similar metal systems. For calculations on significantly different systems the convergence properties would need reverifying.

5.9.1 Fe chain in bulk Cu

In this section we will examine the convergence with respect to cluster size in a bulk defect calculation. As above, the system used is a bulk Cu cluster with the central chain replaced with Fe. In order to establish the convergence behaviour with respect to cluster size, we will compare the charge difference from the substrate system and the magnetic moment for clusters of 7, 19 and 37 chains.

Across these three systems we can make two types of comparison. If we compare the same sites across the systems, e.g., the central chain, then for convergence we expect these sites not to vary significantly between systems. We can also compare similar sites on the borders of the clusters, in this case we are examining how close

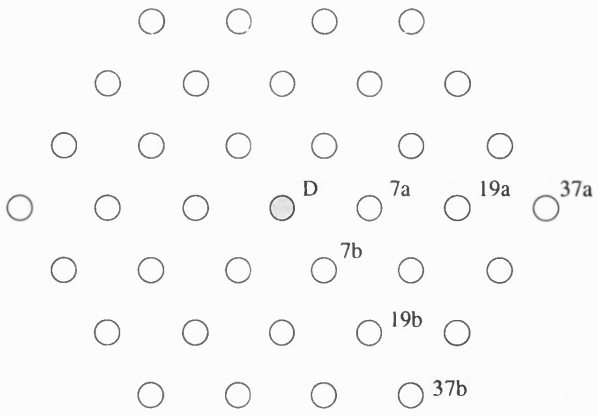

Figure 5.21: Cross-sectional schematic of the cluster geometry used for up to a 37 chain bulk cluster with a central defect chain. The labels used to denote the required unique sites are shown.

the system is to the substrate, i.e., how effective the cluster is at screening the perturbation. Figure (5.21) shows the labels we will use to index the necessary unique sites for the Fe chain in bulk Cu clusters.

First we will examine the charge difference and magnetic moment of the three unique sites that are present in all the clusters. Tables (5.3) and (5.4) show the charge difference from the substrate and magnetic moment for these sites.

Examining these results, we can see that the central site is consistent across all three clusters, with the charge difference from the substrate varying by only 0.0003 electrons between the 7 and 19 chain clusters. Likewise the magnetic moment varies by $0.0003\mu_B$ between the 7 and 19 chain clusters. The other two sites show larger differences between the 7 and 19 chain clusters, which is unsurprising as these are perimeter sites in the 7 chain cluster. Even so, the charge difference is converged to within 0.001 electrons, and the moments to within $0.0002\mu_B$. The differences between the 19 and 37 chain clusters are small for all three sites, less than 0.0001 electrons for the charge difference and $0.0001\mu_B$ for the moments.

	Charge difference		
n_{ch}	D	7a	7b
7	-0.1900	0.0148	0.0397
19	-0.1896	0.0139	0.0392
37	-0.1896	0.0139	0.0391

Table 5.3: Charge difference from the substrate for the unique sites present in 7, 19 and 37 chain cluster calculations for an Fe defect chain in bulk Cu.

n_{ch}	Magnetic moment (μ_B) D	7a	7b
7	2.6043	0.0010	0.0247
19	2.6046	0.0101	0.0249
37	2.6046	0.0101	0.0249

Table 5.4: Magnetic moment on the unique sites present in 7, 19 and 37 chain cluster calculations for an Fe defect chain in bulk Cu.

Table (5.5) shows the charge difference from the substrate at the similar outer sites for the three clusters. Therefore we are comparing sites 7a, 19a and 37a, and also sites 7b, 19b and 37b. We would expect these sites to tend towards the substrate values as the cluster size increases, due to the increased screening of the defect. As can be seen, the charge difference from the substrate decreases steadily across the three systems, reflecting the increasing screening of the defect from the more distant sites. Even for the 7 chain defect the charge difference is only of the order of 0.01 electrons.

These results suggest that for a single defect chain in bulk Cu, a 7 chain cluster is sufficient to do a good job of screening the perturbation. This suggests that a single 'shell' of chains round any bulk defect system is sufficient, e.g., a 19 chain cluster to describe a 3 chain defect. This conclusion is based upon inspection of total charges and moments. Other quantities, e.g., local densities of states, could require use of larger clusters.

n_{ch}	Charge difference outer site a	outer site b
7	0.0397	0.0148
19	0.0023	0.0013
37	0.0003	0.0003

Table 5.5: Charge difference from the substrate for the comparable outer sites present in 7, 19 and 37 chain cluster calculations for an Fe defect chain in bulk Cu.

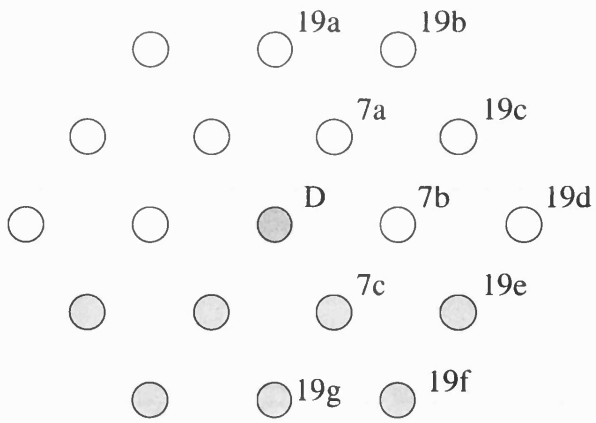

Figure 5.22: Cross-sectional schematic of the geometry for up to a 19 chain cluster surface with defect chain calculation. The labels used to denote the required unique sites are shown.

5.9.2 Fe chain on Cu surface

We now examine the convergence with respect to cluster size in a surface defect calculation, with a single Fe chain on the Cu surface. For this comparison, we will only be comparing 7 and 19 chain clusters, with the structure as determined in the previous sections, the central chain being Fe. Again we will compare the charge difference from the substrate and the magnetic moments on the sites, and also the LDOS on the defect and nearby Cu sites.

As before we can make two types of comparison. If we compare the same sites across the systems, e.g., the central chain, then for convergence we expect these sites not to vary significantly between systems. We can also compare similar sites on the borders of the clusters, in this case we are examining how close the system is to the substrate, i.e., how effective the cluster is at screening the perturbation. Figure (5.22) shows the labels we will use to index the necessary unique sites for the Fe chain in bulk Cu clusters.

We will initially examine the charge difference and magnetic moment of the unique defect and substrate sites that are present in both the clusters. Tables (5.6) and (5.7) show the charge difference from the substrate and magnetic moment for these sites. Examining these results, we can see that for both sites the change in charge difference and magnetic moment between the cluster sizes is small, of the order of 0.002 electrons and $0.002\mu_B$ respectively.

To assess how the properties of the external sites approach those of the substrate values, table (5.8) shows the charge difference and moments for the 3 unique external sites of the 7 chain cluster, and the 7 unique external sites of the 19 chain cluster. As expected, the external sites of the 19 chain cluster are significantly closer to the substrate values of the charge and moment, showing a similar magnitude of decrease as in the bulk chain calculation.

Figures (5.23-5.24) show the DOS for the central Fe chain and the closest Cu surface chain in both 7 and 19 chain cluster calculations. As suggested by the charge difference and moment results, there is very little change in the DOS between the two systems.

These results for the surface chain calculation suggest that the conclusions from the bulk chain calculations are still valid, i.e., that one 'shell' of chains surrounding the defect are sufficient to give accurate values for the charge, magnetic moment and DOS on the defect sites.

n_{ch}	Charge difference D	7c
7	-0.8961	0.1776
19	-0.8942	0.1736

Table 5.6: Charge difference from the substrate for the unique non-vacuum sites present in 7 and 19 chain cluster calculations for an Fe adchain on a Cu surface.

n_{ch}	Magnetic moment (μ_B) D	7c
7	2.9886	0.0187
19	2.9866	0.0193

Table 5.7: Magnetic moments on the unique non-vacuum sites present in 7 and 19 chain cluster calculations for an Fe adchain on a Cu surface.

site	Charge difference	Magnetic moment (μ_B)
7a	0.12719	0.03687
7b	0.11409	0.00050
7c	0.17760	0.01873
19a	0.00561	0.00243
19b	0.00105	0.00033
19c	0.00271	0.00023
19d	0.00115	-0.00005
19e	-0.01157	-0.00070
19f	0.01263	-0.00487
19g	-0.00395	-0.00976

Table 5.8: Charge difference and magnetic moment on the outer sites of a 7 and a 19 chain cluster calculation for an Fe adchain on a Cu surface.

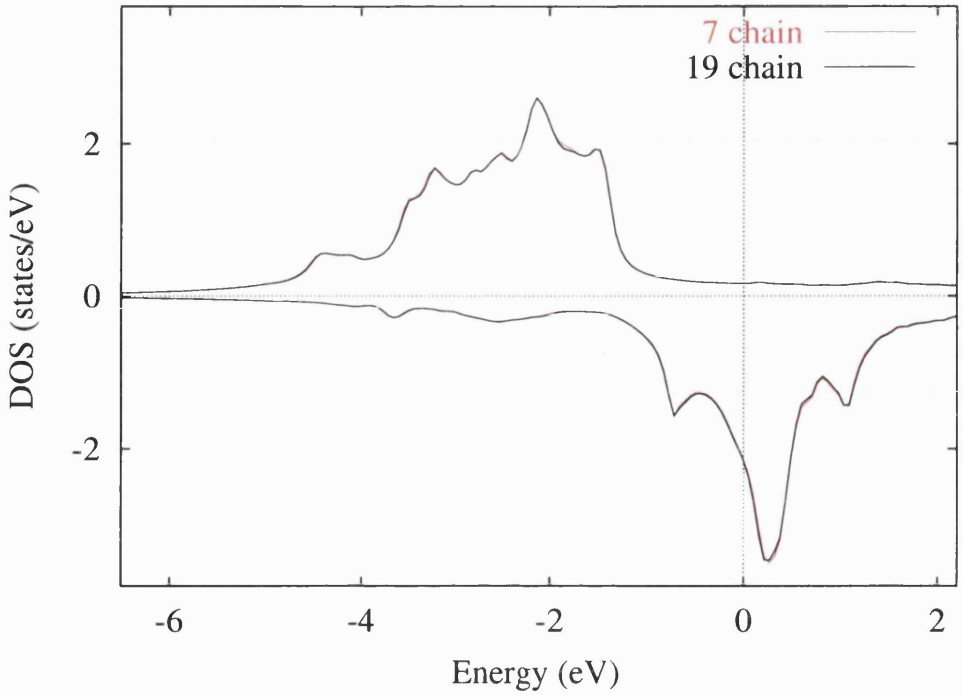

Figure 5.23: Comparison of the densities of states calculated using 7 and 19 chain clusters for an Fe adchain on Cu surface calculation, for the Fe adchain site.

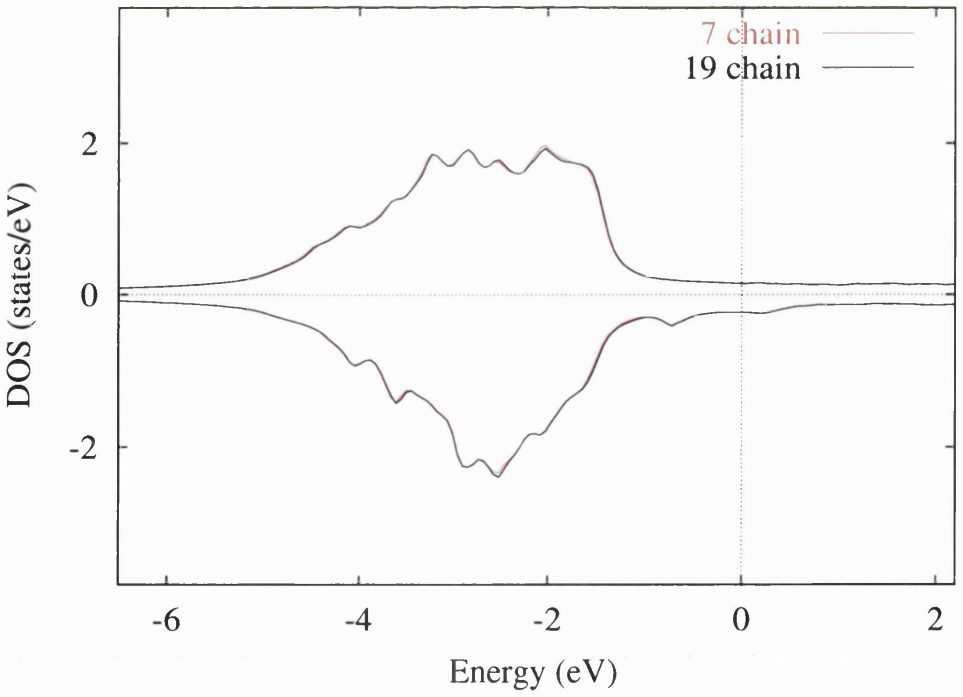

Figure 5.24: Comparison of the densities of states calculated using 7 and 19 chain clusters for an Fe adchain on Cu surface calculation, for the closest Cu surface site.

Chapter 6

Monatomic chains of $3d$ metals on Cu$(00\bar{1})$

6.1 Introduction

In this chapter we will use the chain defect method introduced and described in previous chapters in self-consistent electronic structure calculations of $3d$ chains on the Cu(001) surface. The initial calculations will be for the clean Cu surface, and for Cu chains on the Cu surface, we will then move on to various systems of $3d$ chains, including embedded chains and multiple chains. Calculations of $3d$ monolayers on the Cu surface will be used for comparison.

For magnetic systems, only ferromagnetic chains and monolayers are considered in this work. While some of the $3d$ elements may favour antiferromagnetic spin configurations, without accurate total energy calculations, which are not included here, it is not possible to determine the ground state magnetic configuration. In addition, antiferromagnetic chain calculations require considerably greater computational resources, necessitating twice as many sites in the chain cluster.

On the basis of the convergence tests reported in chapter 5, unless otherwise indicated, the potentials within this chapter are all converged using 256 **k**-points, $\ell_{\max} = 3$ and 16 energy points in the contour. Densities of states calculations are performed using 4096 **k**-points, 500 energy points and Im(E) = 0.001 Ha.

6.2 Clean Cu(001) surface

The substrate system to be used in the chain defect calculations is the clean Cu(001) surface. It is therefore important to demonstrate that the results for this substrate system are consistent with previous work, before attempting to calculate chain defects on the surface. There are numerous theoretical studies of the electronic structure of the Cu(001) surface in the literature [116, 42, 115, 100, 15]. As was the case for the convergence results, for the calculations of the Cu(001) surface the z-axis was taken normal to the surface with positive z pointing out of the surface. The substrate surface system was converged with 3 vacuum layers and 4 Cu layers in which the potentials were permitted to relax. The potentials were converged self-consistently using the LKKR method, with 16 energy points in the contour integral, 25 g-vectors in the plane wave basis set, 256 $\mathbf{k}$-points and $\ell_{\max} = 3$.

Figure (6.1) shows the DOS for the surface (S) and three subsurface (S-1, S-2, S-3) layers of the Cu(001) surface, in comparison to the bulk Cu DOS converged with the same parameter set. The general form and features of the densities of states agree with prior calculations [116, 42, 115].

The upper edge of the Cu d-band is 1.5 ± 0.1 eV below the Fermi level for the surface sites as well as in the bulk. This explains the non-magnetic nature of Cu, and is the reason for the relatively weak hybridisation between Cu and the transition metals, whose d-bands tend to be higher in energy, straddling the Fermi level. This provides some justification for considering transition metal structures on Cu surfaces as quasifree systems. From figure (6.1) we see that significant alterations in the shape and structure of the DOS are limited to the surface layer, due to the screening effects. The surface layer DOS is narrower than the bulk DOS, due to the reduction in the number of nearest neighbours: 8 as opposed to 12 in the bulk. The subsurface layers become increasingly bulk like as they get further from the surface, with the S-3 layer showing very little deviation from the bulk.

The results for the Cu(001) surface are sensible, and consistent with previous calculations in the literature. Therefore we can use the potentials from the Cu surface as the substrate for calculations of chain defects on the surface.

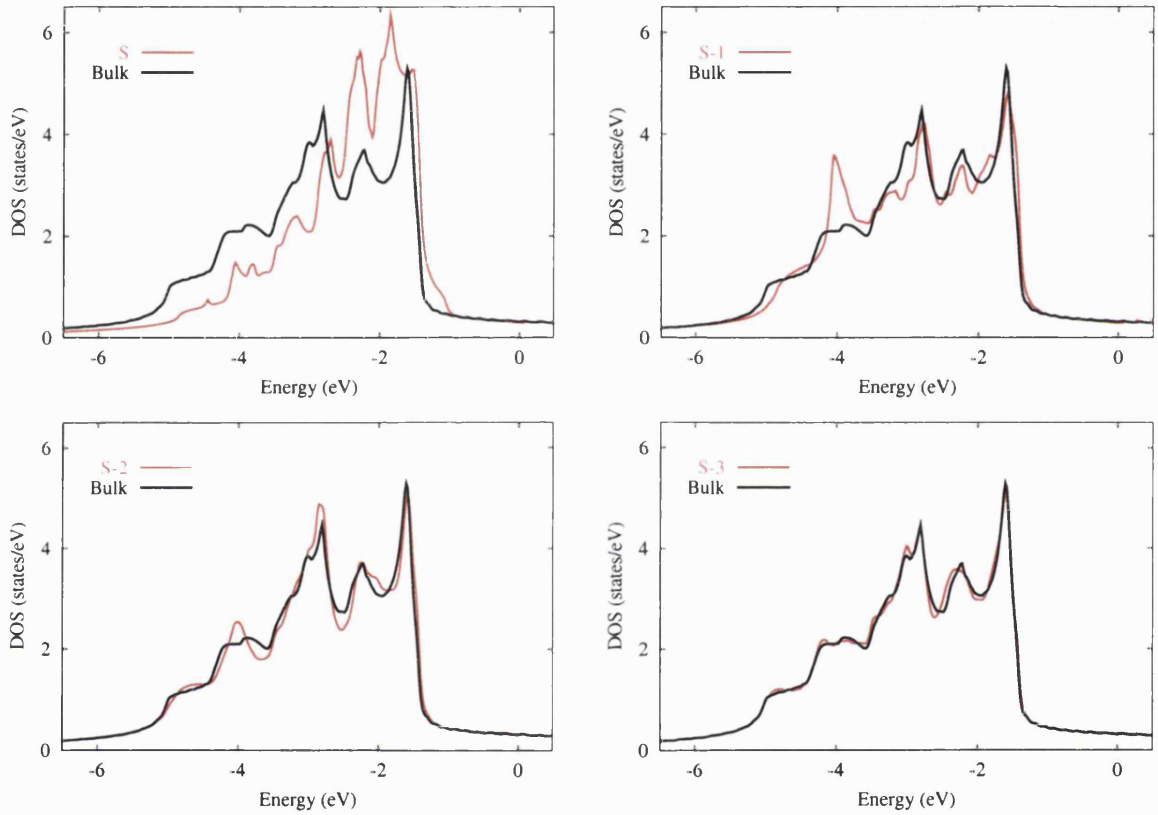

Figure 6.1: Densities of states for the first four layers of a Cu(001) surface, as compared with bulk Cu. S denotes the surface layer, with S-1 to S-3 the subsurface layers.

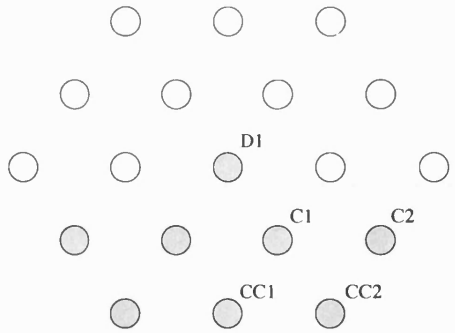

Figure 6.2: Cross-sectional schematic of the cluster geometry for a 19 chain surface with a single defect chain on the surface. The labels used to denote the unique sites are shown.

6.3 Cu chains on the Cu surface

We now consider defect calculations for systems of Cu chains on the Cu surface. As was the case in the convergence results chapter, the chains are taken to occupy the ideal adatom sites along the $\langle 110 \rangle$ direction. Figure (6.2) demonstrates the unique site labels used for a 19 chain cluster describing a single Cu chain on a Cu surface. This labelling scheme will be used throughout this results chapter.

The densities of states for the Cu chain site (D1), and the unique surface and subsurface sites (C1, C2, CC1 and CC2), are shown in figure (6.3), compared with clean surface and subsurface densities of states as calculated above. The chain site has fewer nearest neighbour Cu atoms than the surface sites, 6 as opposed to 8, hence as expected the DOS is narrower than the clean surface DOS. This reflects the reduction in hybridisation of the adchain *d*-states with substrate orbitals compared to surface atoms. The surface site nearest the chain (C1) actually has more nearest neighbours than a clean surface site, 9 as opposed to 8, hence we see that the DOS for this site is broader than a clean surface site, in effect becoming more bulk-like. Beyond these sites the other surface site (C2) and the subsurface sites (CC1 and CC2) show little significant deviation in their DOS from the surface and subsurface sites respectively in a clean surface calculation. From these results we can see that the DOS tends to reflect the local environment, being largely determined by the configuration and species of nearest neighbour atoms.

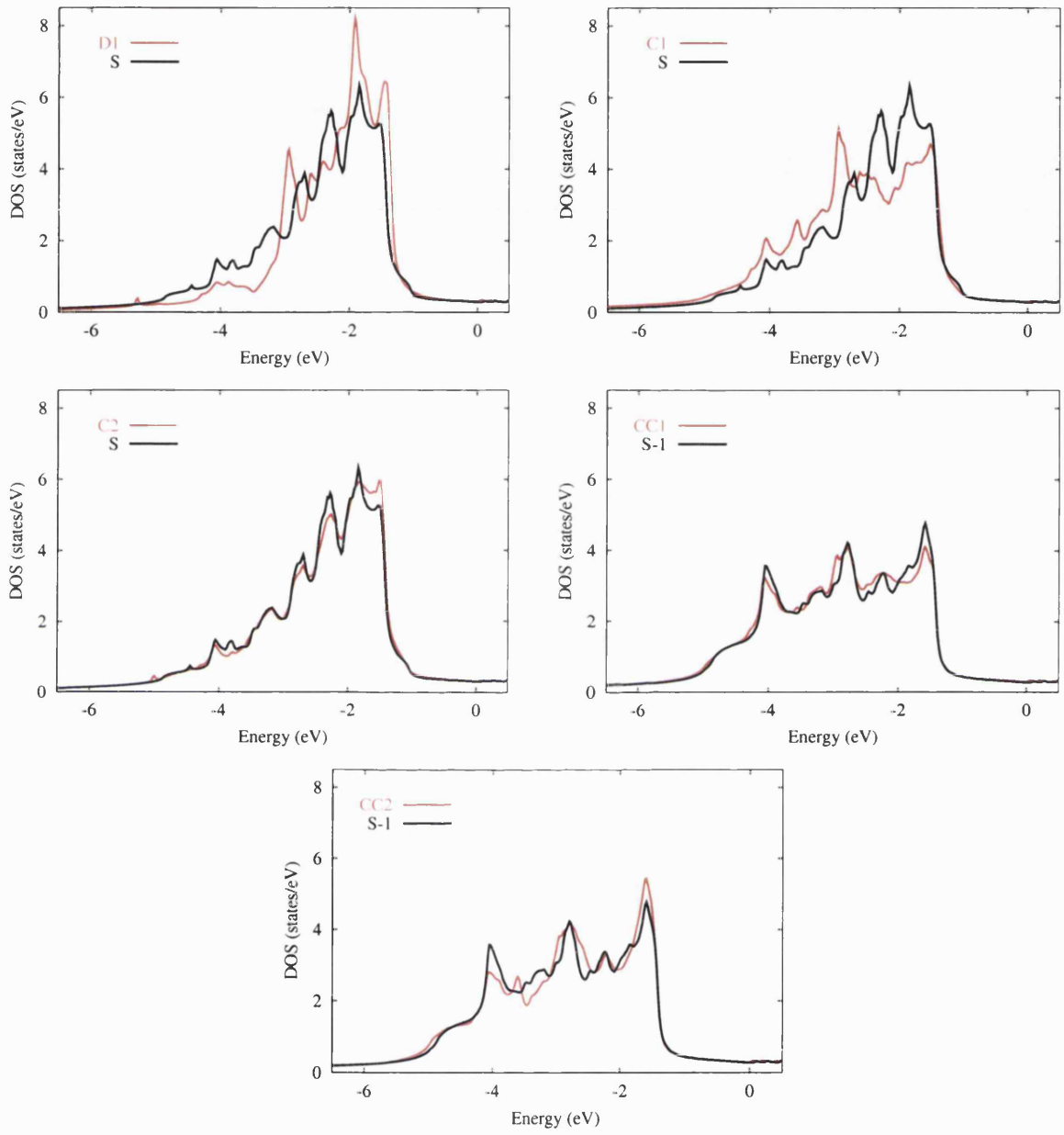

Figure 6.3: Densities of states for the unique sites in a Cu chain on Cu surface calculation, as compared with the S and S-1 layers in a clean Cu surface calculation.

6.4 Single chains

In this section we will examine the electronic structure of various $3d$ defect chains on the Cu(001) surface. Results shown include calculations of the magnetic moments of the chain sites, and the induced moments in the Cu substrate, and both paramagnetic and spin-resolved DOS plots for the chain systems. Results are also shown for $3d$ monolayers on the Cu surface, allowing comparison between the chain and monolayer behaviour.

The trends seen in the magnetic moments for the chains can be explained in terms of a relatively simple itinerant magnetism model, with the Stoner criterion able to predict which systems will exhibit ferromagnetic solutions. The behaviour of the moments can be understood in terms of the hybridisation between the $3d$ atoms themselves, and between the $3d$ atoms and the Cu substrate.

As demonstrated in the previous sections, reduction of the coordination number results in a narrowing of the DOS. Hence the DOS of a surface site will be narrower than the corresponding bulk DOS, and the DOS of an isolated chain on a surface will be narrower still.

We can use a simple Stoner type argument to account for the increased tendency towards ferromagnetism that is often seen in low-dimensional systems. The Stoner criteria for ferromagnetism [120, 121] is

$$I(E_f)n(E_f) > 1, \tag{6.1}$$

where $n(E_f)$ is the density of states at the Fermi level, and $I(E_f)$ is the Stoner parameter. For most transition metals a narrowing of the density of states will generally result in an increase of the density of states at the Fermi level, and hence an increased tendency towards ferromagnetism. In addition to predicting a ferromagnetic solution, an increase in the magnitude of the product $I(E_f)n(E_f)$ for a given system indicates an increase in the magnetic moment. Thus we observe the general trend in transition metals that reducing the dimensionality results in increased magnetic moments.

We can demonstrate this effect by considering $3d$ monolayers and chains. In their normal bulk phases Fe, Co and Ni exhibit ferromagnetism. Mn monolayers on

Cu(001) are also predicted to have ferromagnetic order [5], while as adatoms on Cu all the elements V through Ni are predicted to exhibit significant moments [75]. We can perform paramagnetic DOS calculations for monolayer and single chain defect systems, and combine the results with calculated values for the Stoner parameter [92, 60] to predict which systems will have a ferromagnetic solution.

Figure (6.4) shows the self-consistent paramagnetic DOS for the $3d$ elements V through Ni as both monolayers and isolated chains on the Cu(001) surface. The chain calculations were performed with 19 chain clusters, with the central chain in the cluster being the adchain. The monolayer calculations were standard LKKR calculations, with 3 vacuum and 4 surface layer potentials allowed to vary, and the same parameter set as the chain calculations.

Examining the DOS plots, for Cr, Mn, Fe, Co and Ni the chain DOS exhibits a significant narrowing effect compared to the monolayer, with a large central peak to the DOS, although the triple peak structure is still visible. For the V chain the narrowing of the DOS is less clear, and no significant peak is seen. In the case of Cr, Mn and Fe the central peak is sufficiently close to the Fermi level that $n(E_f)$ for the chain system is larger than for the monolayer system. For the Co chain DOS, the Fermi level falls between the central peak and one of the lesser peaks. This results in no enhancement of $n(E_f)$ for the chain system, indeed $n(E_f)$ is actually higher in the monolayer system. For the Ni chain DOS the central peak is located below the Fermi level, although in this case the structure of the chain and monolayer densities of states leads to a small increase in $n(E_f)$ for the chain system. The V chain and monolayer DOS are broadly similar, with the DOS at the Fermi level slightly lower for the chain as compared with the monolayer.

We can combine the values of $n(E_f)$ from the paramagnetic densities of states with calculated values for the Stoner parameter [60] to determine in which systems the Stoner criteria is satisfied. Table (6.1) displays this data for the $3d$ monolayers and chains. From these results we see that the Stoner criteria is satisfied for Cr chains, and for Mn, Fe, Co and Ni monolayers and chains. Therefore we would expect to find ferromagnetic solutions for these systems. As can be seen from the paramagnetic DOS plots and in the table, $n(E_f)$ is higher for the Fe and Mn chain than the monolayer, hence in these systems we would expect the moments to be larger for the chain than the monolayer. For Co we have the opposite situation, and would thus expect the chain moment to be reduced compared to

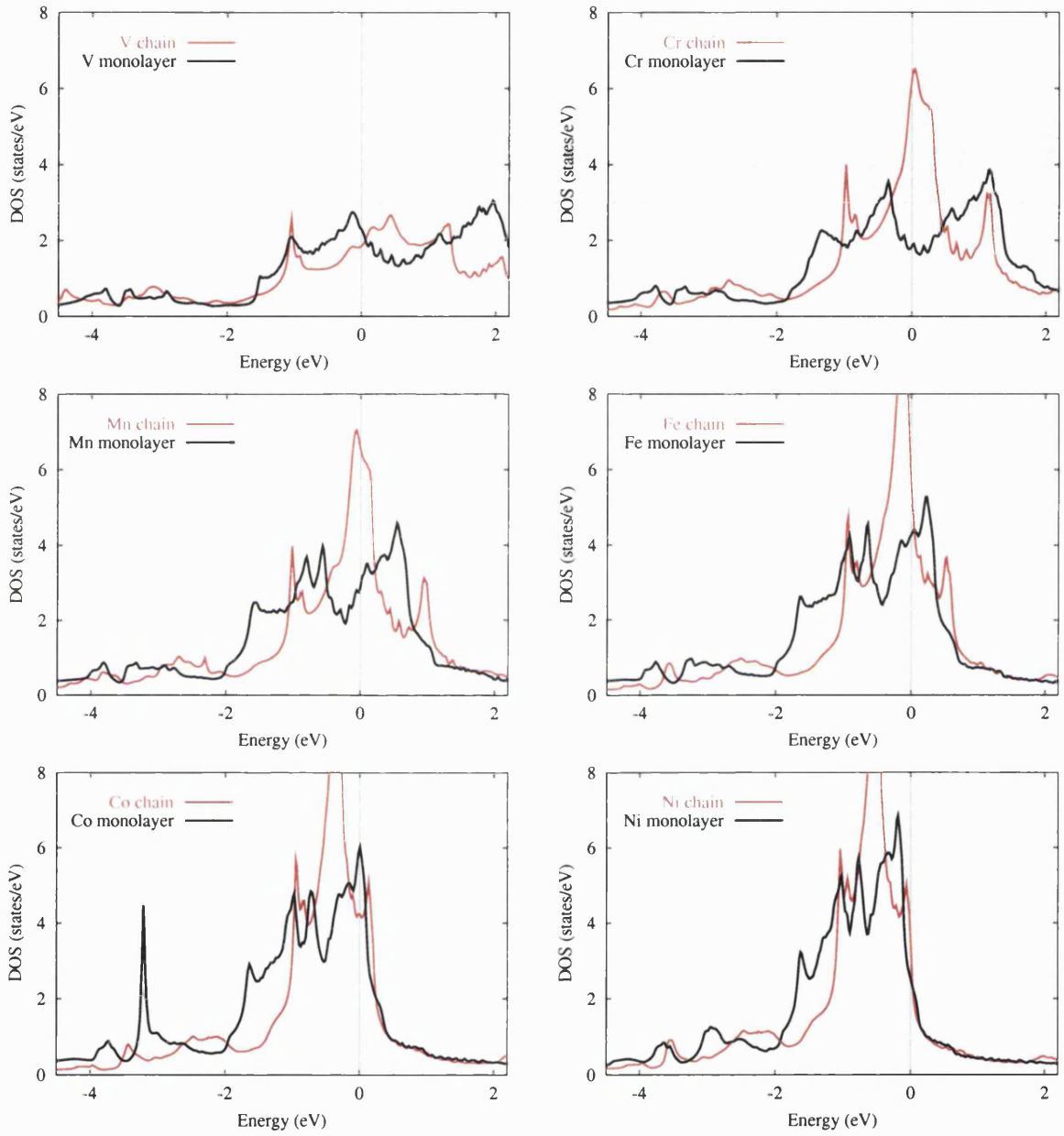

Figure 6.4: Paramagnetic densities of states for single chains and monolayers of V, Cr, Mn, Fe, Co and Ni on the Cu(001) surface.

		Monolayer		Chain	
Metal	$I(E_f)$	$n(E_f)$	$I(E_f) \times n(E_f)$	$n(E_f)$	$I(E_f) \times n(E_f)$
V	0.35	2.3	0.81	1.8	0.63
Cr	0.38	1.8	0.68	6.2	2.36
Mn	0.41	2.9	1.19	6.5	2.67
Fe	0.46	4.2	1.93	5.5	2.53
Co	0.49	6.0	2.94	4.2	1.93
Ni	0.50	2.5	1.25	3.6	1.80

Table 6.1: Comparison of the Stoner criteria for V, Cr, Mn, Fe and Co monolayers and chains on Cu(001). Values for the Stoner parameter were taken from [60].

the monolayer. For Ni $n(E_f)$ is slightly higher for the chain than the monolayer, thus we would expect a slight increase in the moment for the chain system.

Previous calculations for $3d$ monolayers on Cu(001) predicted Mn to have a ferromagnetic solution, and V and Cr to be paramagnetic [5], in agreement with the above predictions. As noted in the introduction antiferromagnetic solutions are not considered here, although calculations for $3d$ monolayers on Ag(001) indicate that V, Cr and Mn monolayers tend to favour this spin configuration [9, 5].

We now consider spin-polarised calculations, and begin by examining the calculated moments for the $3d$ chain and monolayer systems. Figure (6.5) compares the moments on a single defect chain with the moments for a monolayer, as a function of the adchain element. These moments are also displayed in table (6.2). As in the paramagnetic calculations above, the chain calculations were performed with 19 chain clusters, with the central chain in the cluster being the adchain. The monolayer calculations were standard LKKR calculations, with 3 vacuum and 4 surface layer potentials allowed to vary, and the same parameter set as the chain calculation.

The calculated chain moments behave broadly as expected, while the monolayer moments are consistent with previous calculations for these systems [5]. As was predicted using the Stoner criteria, V is paramagnetic as both a monolayer and a

	V	Cr	Mn	Fe	Co
Monolayer	0.00	0.00	3.47	2.80	1.82
Single chain	0.02	2.56	3.85	2.99	1.69

Table 6.2: Magnetic moments in μ_B for $3d$ monolayers and single chains on the Cu(001) surface.

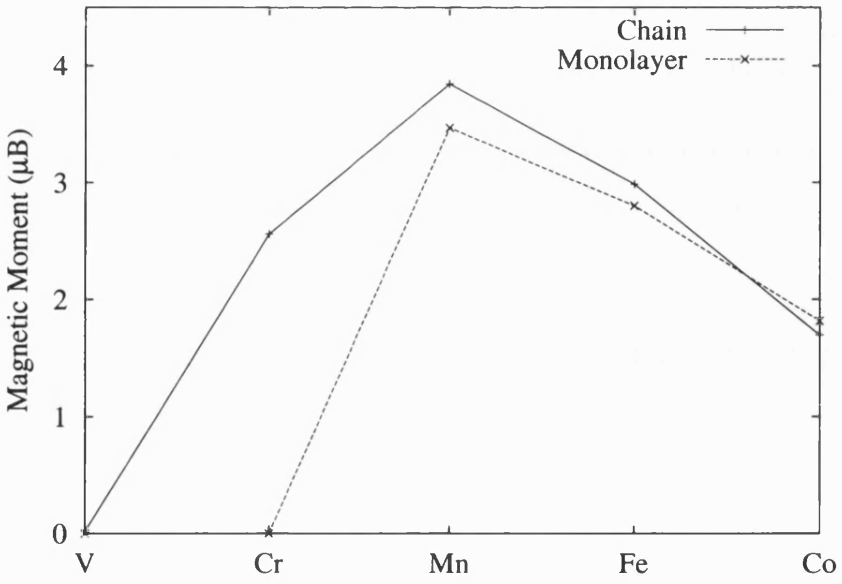

Figure 6.5: Magnetic moments for $3d$ single chains and monolayers on the Cu(001) surface.

chain. Cr chains are ferromagnetic, while the Cr monolayer is paramagnetic. For Mn and Fe both the chain and monolayer systems are ferromagnetic, with the chain exhibiting an enhanced moment over the monolayer. Co is ferromagnetic both as a chain and a monolayer, with the chain moment slightly lower than the monolayer moment.

No results are given for spin-polarised Ni chain or monolayer calculations. This was due to difficulties in converging the Ni systems as magnetic solutions. The analysis of the Stoner criteria suggests that magnetic solutions should be present, and that the chain should exhibit a slight increase in the moment as compared to the monolayer. Previous calculations for a Ni monolayer on Cu(001) found a moment of $0.32\mu_B$ [5].

The differences between the monolayer and chain results are due to the *d-d* interactions between the adsorbate atoms, as the monolayer atoms have 4 nearest neighbours of the same species, while the chain atoms have only 2. This interaction tends to broaden the DOS. The $3d$-orbitals are more extended at the beginning of the $3d$ series. This leads to increased hybridisation between these elements, making them more sensitive to environmental changes. For example, V has a moment of about $3\mu_B$ as an adatom [75], which is entirely quenched as a chain or a monolayer, while the moment for Fe varies from just over $3\mu_B$

for an adatom to just under $3\mu_B$ for a monolayer. At the end of the $3d$ series the d-d interaction tends to enhance the moment, e.g., Ni where the adatom is nonmagnetic [75] while the monolayer on Cu has a moment of $0.32\mu_B$ [5]. This is due to the position of the main DOS peak relative to the Fermi level. For the later elements the peak in the DOS falls below the Fermi level, thus broadening of the DOS can result in an increase of $n(E_f)$. This effect is seen in the Co chain having a slightly lower moment than the Co monolayer.

To understand the behaviour of the magnetic moments, we can analyse the spin-polarised densities of states for the single chain systems, shown in figure (6.6), and for the monolayer systems, shown in figure (6.7). As is the case for the bulk elemental ferromagnets we see an exchange splitting between the majority and minority spin DOS, except in the case of the V chain which is paramagnetic. The exchange-splitting between spins is larger than one sees in the bulk, reflecting the increased moments. For the Mn, Fe and Co chains the majority spin d-band is completely filled. Hence these chains can be considered as strong ferromagnets, with the moments from Mn to Co decreasing in steps of approximately $1\mu_B$, following Hund's first rule. The monolayers of Mn, Fe and Co display similar behaviour, having nearly full majority d-bands, although the moments of the Mn and Fe monolayers are lower than for the chains due to the increased d-d hybridisation.

One notable feature of the spin-resolved chain DOS is the difference in structure of the majority and minority spin DOS. This is due to the large exchange splitting allowing the majority d-band to hybridise with the d-band of the Cu substrate. Figure (6.8) illustrates this effect, showing the DOS for a spin-polarised and a paramagnetic Mn chain, as well as the C1 Cu surface site immediately below the chain. In the paramagnetic calculation there is minimal overlap between the d-band DOS contributions. However in the spin-polarised calculation, the exchange-splitting shifts the majority spin d-band down in energy so as to overlap with the Cu d-band, allowing hybridisation.

The hybridisation with the Cu d-band has little effect on the moments, as the Cu d-band edge is approximately 1.5eV below the Fermi level. Hybridisation between the chain $3d$ and the Cu sp states will have some broadening effect on the DOS, leading to some reduction in the moments. This is likely to be more significant for the early elements in the series, e.g., V and Cr, due to the larger

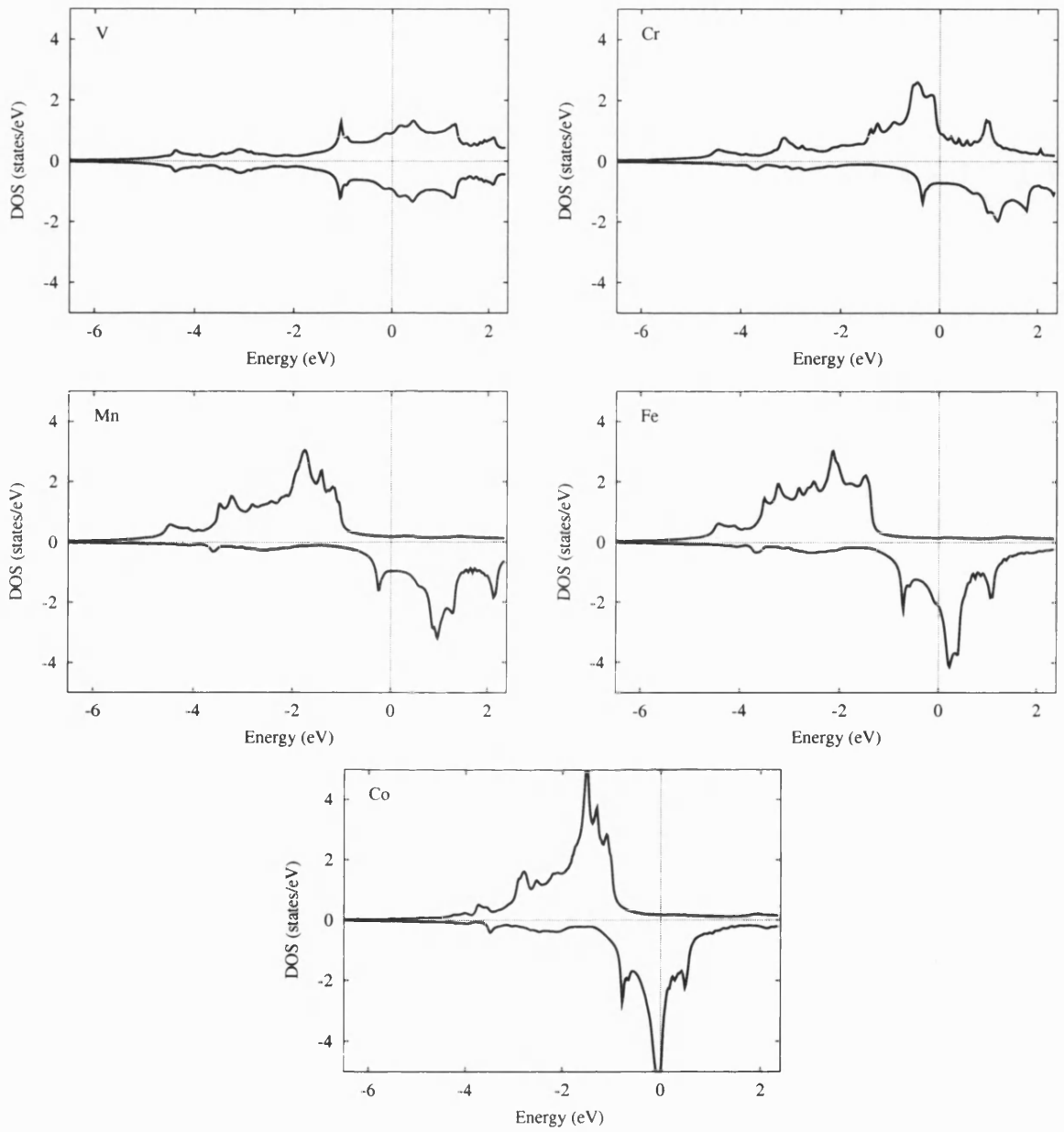

Figure 6.6: Spin-polarised densities of states for V, Cr, Mn, Fe and Co single chains on the Cu(001) surface. In each case the upper panel shows the majority spin DOS and the lower panel the minority spin DOS.

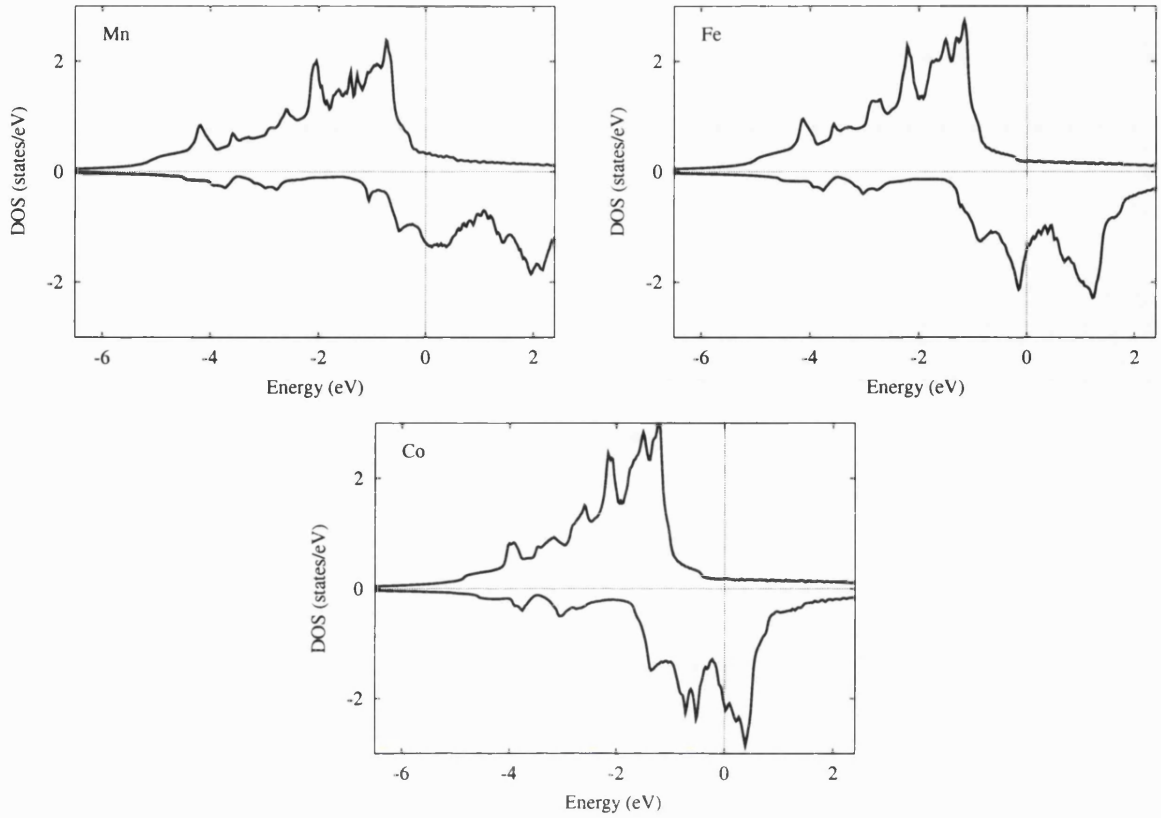

Figure 6.7: Spin-polarised densities of states for Mn, Fe and Co monolayers on the Cu(001) surface. In each case the upper panel shows the majority spin DOS and the lower panel the minority spin DOS.

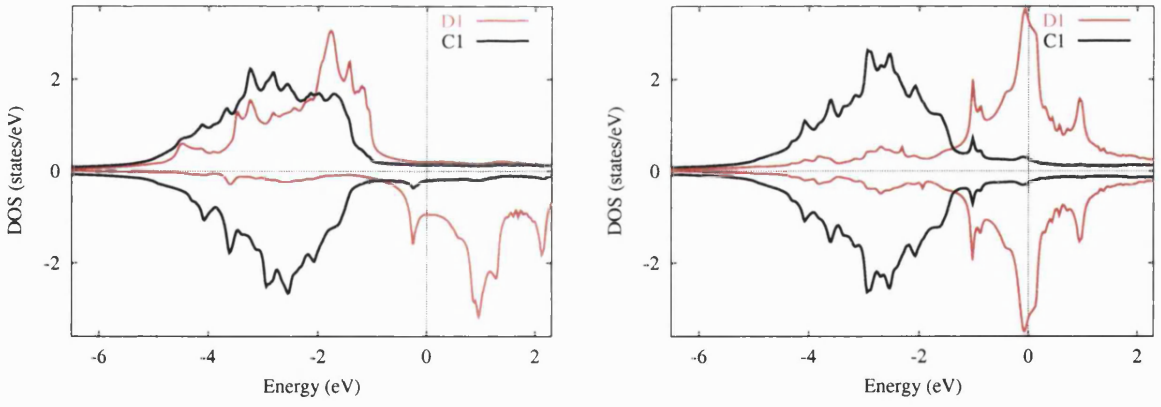

Figure 6.8: Densities of states for spin-resolved and paramagnetic Mn chains on a Cu surface. The large exchange-split in the magnetic system allows hybridisation between the majority *d*-bands of the Mn chain (D1) and the Cu surface (C1). As above the upper panel shows the majority spin DOS and the lower panel the minority spin DOS.

	Cr	Mn	Fe	Co
Single chain C1 site	0.06	0.04	0.02	0.002
Monolayer C1 site	-	0.08	0.03	0.01

Table 6.3: Magnetic moments in μ_B on the nearest Cu site for $3d$ single chains and monolayers on the Cu(001) surface.

extent of the $3d$-orbitals and absence of strong ferromagnetism. It is likely that an unsupported V chain would exhibit ferromagnetism, given that calculations predict ferromagnetism for unsupported V monolayers [13]. Calculations of $3d$ monolayers on the Ag(001) surface exhibit this behaviour, with the moments of Ti, V and Cr monolayers on Ag being significantly reduced when compared to unsupported monolayers [13]. With the lattice reduction in going to a Cu(001) substrate, this quenching effect is likely to be increased.

The hybridisation between the chain $3d$-orbitals and the Cu substrate can lead to small induced moments in the Cu substrate. This effect is seen in monolayer calculations, e.g., a monolayer of Fe on Cu(001) is predicted to induce a $0.04\mu_B$ moment in the nearest Cu site [38]. Table (6.3) shows the nearest Cu moments (i.e., the C1 site in a 19 chain cluster, and the subsurface site in a monolayer system) for Cr, Mn, Fe and Co single chain and monolayer systems. These moments are all ferromagnetic, i.e., aligned with the spin of the $3d$ defect. We can see that the monolayer moments are generally higher, with the exception of Cr where there is no ferromagnetic monolayer solution. This is to be expected, as although the chain sites generally have a slightly enhanced moment over the monolayer, the C1 chain site has only 2 $3d$ nearest neighbours, while the monolayer Cu site has 4. Also noticeable is the trend towards lower induced moments with increasing atomic number of the defect species. As was mentioned above the d-orbitals are larger for the elements earlier in the series. This leads to greater hybridisation with the Cu substrate, hence larger induced moments. Calculations for Co chains on a Pd(110) surface predict considerably larger induced moments of $0.23\mu_B$ for the nearest Cu site [105]. As Pd is not a noble metal we would expect greater hybridisation between Co chains and a Pd substrate than with a Cu substrate, hence the higher induced moments.

We can now compare the moments for $3d$ adatoms [75], chains and monolayers on Cu(001), shown in figure (6.9), with $4d$ adatoms [75], chains [4] and monolayers [10] on the Ag(001) surface, shown in figure (6.10). Although dealing with different elements on different substrates, the general behaviour of chains compared

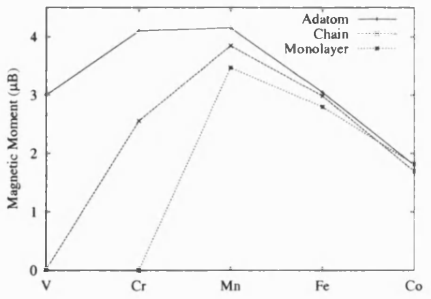

Figure 6.9: Local moments for adatoms [75], infinite chains and monolayers of the $3d$ elements on the Cu(001) surface.

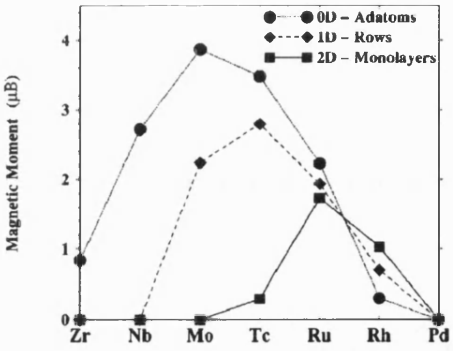

Figure 6.10: Local moments for adatoms [75], infinite close packed rows [4] and monolayers [10] of the $4d$ elements on the Ag(001) surface. From [4].

with adatoms and monolayers can be seen in both cases. In general the chain moments fall between the adatom and the monolayer moments, as expected.

To summarise then, the magnetic moments of the $3d$ chains on the Cu(001) surface are principally determined by two interactions, the *d-d* interaction within the chains, and the *d-sp* hybridisation between the chain atoms and the Cu substrate atoms. The first mechanism tends to decrease the moments at the start of the series, and to enhance the moments at the end of the series, e.g., Co and to a greater extent Ni. The second mechanism consistently tends to decrease the moments, with the moments of the elements earlier in the series experiencing greater reduction due to the lack of strong ferromagnetism and the more extended nature of the $3d$ orbitals.

With these two mechanisms in mind, we can move onto examining other systems of $3d$ chains on the Cu(001) surface. The first we will consider is the chain embedded in the surface.

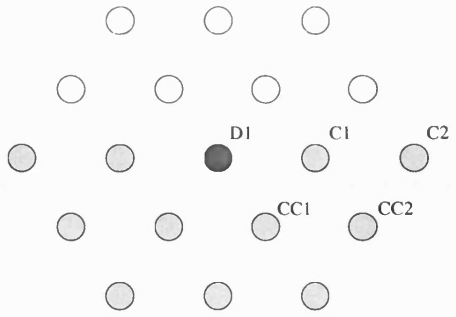

Figure 6.11: Cross-sectional schematic of the 19-chain cluster geometry for a surface with a single embedded defect chain. The labels used to denote the unique sites are shown.

6.5 Embedded chains

We now consider the moments of an embedded chain, that is a chain that has replaced one of the Cu sites in the surface. The site geometry and labelling used in this calculation is shown in figure (6.11) for a 19 chain cluster, as used in these calculations. The moments for the embedded chains of the $3d$ elements in the Cu(001) surface are shown in figure (6.12), compared with the moments for the chains on the surface. These moments are also shown in table (6.4).

The moments show a general slight reduction for the embedded chains, with a significant reduction in the Cr chain moment, from $2.56\mu_B$ to $1.52\mu_B$. These results are consistent with the analysis of the moments of the chains on the surface. The embedded chain has more nearest neighbour Cu atoms than the chain on the surface, 6 as opposed to 4. This means that the $3d$-sp hybridisation between the chain and the substrate will be increased. For Mn through to Co this has only a minor effect, due to the filled majority d-bands in these chains. The effect on the Cr chain moment is more dramatic due both to the lack of strong ferromagnetism, and the greater spatial extent of the $3d$-orbitals for the

	V	Cr	Mn	Fe	Co
Surface chain	0.018	2.56	3.85	2.99	1.69
Embedded chain	0.012	1.52	3.71	2.91	1.62
Bulk chain				2.60	
Bulk impurity				2.51	

Table 6.4: Magnetic moments in μ_B for $3d$ single chains on and embedded in the Cu(001) surface. Also shown are the moments for an Fe chain in bulk Cu, and for an Fe impurity atom in bulk Cu [13].

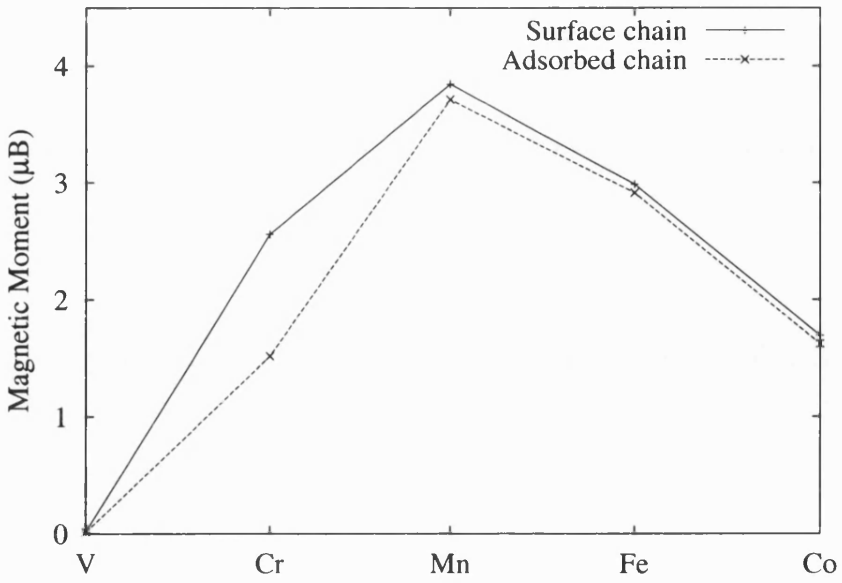

Figure 6.12: Magnetic moments for $3d$ single chains and embedded chains on the Cu(001) surface.

lower valence elements. To illustrate this effect still further, table (6.4) also shows the moments for an Fe chain in bulk Cu, and for a single Fe atom in bulk Cu. The increase in Cu nearest neighbours (10 and 12 respectively) leads to further reduction in the moment.

6.6 Multiple chains

We now consider systems of multiple chains on the surface. As more chains are added, one would expect the moments to approach the monolayer values. We will consider systems with 2, 3 and 4 chains on the surface, with clusters of 10, 19 and 24 chains used in the respective calculations. Figure (6.13) shows the geometries of the clusters used, along with the unique site labels. The justification for the cluster sizes used was demonstrated in chapter 5. It was found that a single shell of chains around the defect was sufficient to obtain converged values for the moments on the defect chain. Additional calculations were performed using 24 chain clusters to describe 2 chain defects, for comparison with results from 10 chain clusters. The moments were found to be consistent to within $0.001\mu_B$ between the two cluster sizes, justifying the above choice of clusters for use in

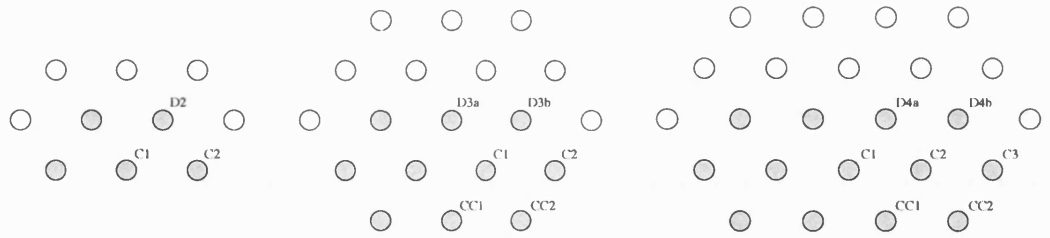

Figure 6.13: Cross-sectional schematic of the geometry for the 10, 19 and 24 chain clusters used for the 2, 3 and 4 chain on surface calculations. The labels used to denote the unique sites are shown.

multiple chain calculations.

We now examine the calculated moments for the multi-chain $3d$ defects on the Cu(001) surface. Figures (6.14-6.16) show the moments for the 2, 3 and 4 chain defect systems compared with single chains and monolayers, for the $3d$ elements. The moments for the unique defect sites of the various chain systems and the monolayers are also shown in table (6.5).

As expected, the moments for the multiple chain systems generally fall between the single chain and monolayer values. Thus the moments for the Cr, Mn and Fe chains are reduced for the multiple chain systems in comparison to the single chain, while the Co moment generally shows a slight increase. The magnitude of the changes is greatest for the Cr chains, as is expected from the arguments in section 6.4 relating to the increased sensitivity of the elements earlier in the $3d$ series to their local environment. For the 3 and 4 chain systems, the central chains are closer to the monolayer values than the edge chains. This reflects the increased similarity of their local environment to a monolayer, having 4 nearest neighbours of the same species as opposed to 2 for the edge sites.

	V	Cr	Mn	Fe	Co
1	0.02	2.56	3.85	2.99	1.69
2	0.01	1.13	3.70	2.85	1.73
3a	0.00	0.70	3.54	2.79	1.76
3b	0.01	1.41	3.70	2.88	1.68
4a	0.01	0.55	3.46	2.78	1.74
4b	0.01	0.94	3.66	2.87	1.70
ML	0.00	0.00	3.47	2.80	1.82

Table 6.5: Magnetic moments in μ_B for multiple $3d$ chains on the Cu(001) surface. Included for comparison are the moments for the monolayer on the Cu(001) surface.

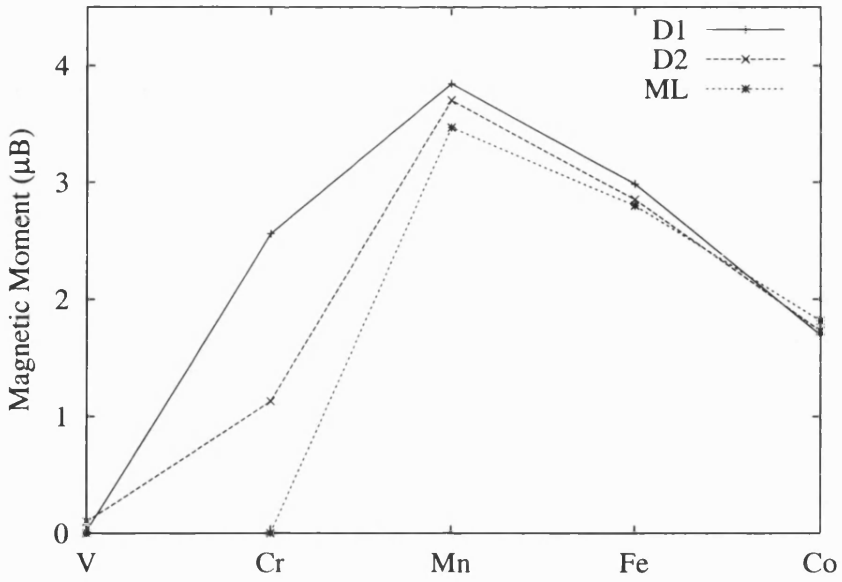

Figure 6.14: Magnetic moments for $3d$ single chains, double chains and monolayers on the Cu(001) surface.

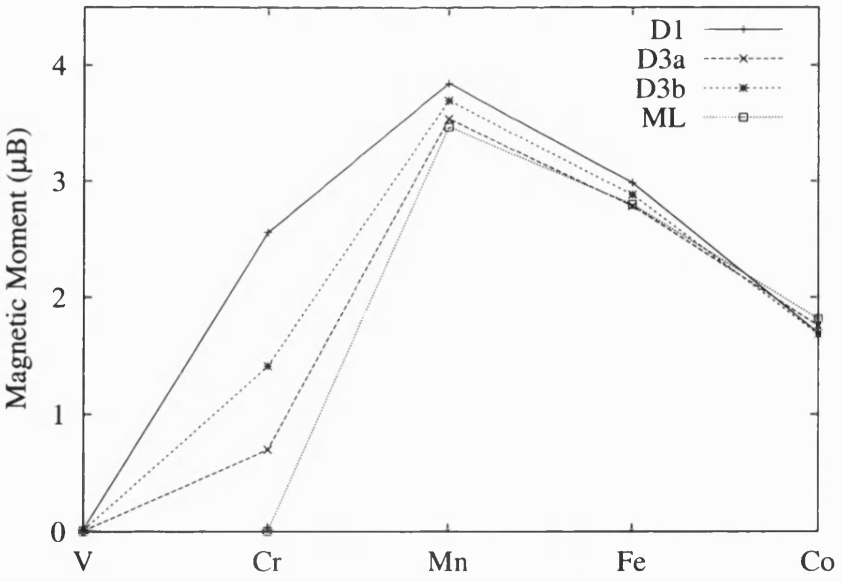

Figure 6.15: Magnetic moments for $3d$ single chains, triple chains and monolayers on the Cu(001) surface.

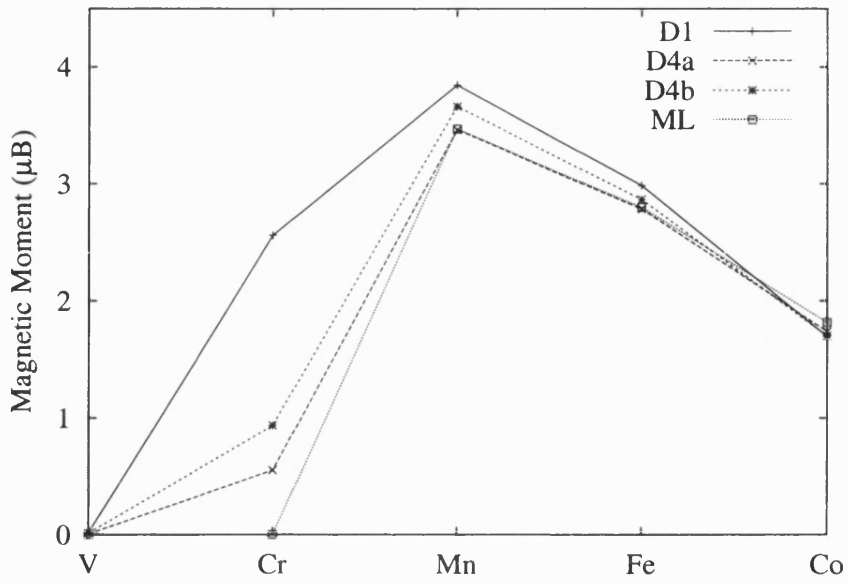

Figure 6.16: Magnetic moments for $3d$ single chains, quadruple chains and monolayers on the Cu(001) surface.

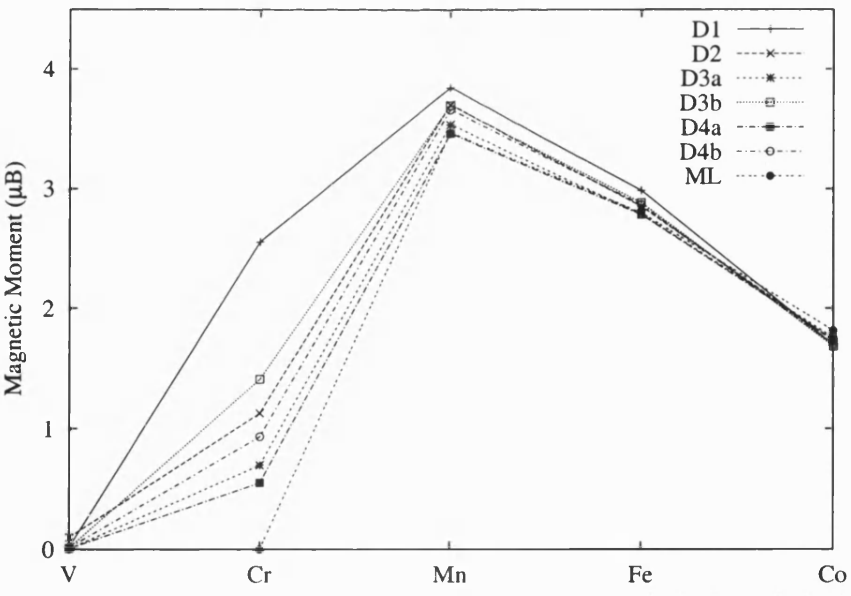

Figure 6.17: Magnetic moments for arrays of 1-4 $3d$ chains, and $3d$ monolayers, on the Cu(001) surface.

Figure (6.17) shows on one plot the moments for the defect sites of the 1, 2, 3 and 4 chain defect systems, and the monolayer moments. From this we can observe the same basic trends over the full range of systems. As we might expect, the D4a moment is closest to the monolayer value, followed by the D3a moment. The edge sites, that is 2, 3b and 4b, all fall between the single chain and the central chain (3a and 4a) moments. The edge sites have 3 nearest neighbours of the same species, compared to 2 for the single chain and 4 for the central sites, so this is to be expected. In addition, the edge site values tend to be quite close together, reflecting the similarity of their environments.

Some deviations from this general behaviour are the 4a moment for Mn and Fe being lower than the ML moment, and the 3b and 4b moments for Fe being higher than the 2 moment. These are all small effects, less than $0.03\mu_B$ and may be oscillatory in nature. The Co moments are also slightly inconsistent, with the 3b moment lower than 1 and 2, the 4b lower than 2 and the 3a higher than 4a. Again these are minor effects and it is difficult to determine if they are physical or numerical in nature.

The Cr chains are of particular interest since the chains couple antiferromagnetically. That is to say that the moments are aligned ferromagnetically along the chains, with adjacent chain moments alternating in sign. Thus for the 2 Cr chains on the Cu surface, one chain has a moment of $+1.13\mu_B$ and the other has $-1.13\mu_B$. This antiferromagnetic coupling is also seen in the 3 and 4 Cr chain defect systems. Attempts to converge defect systems with the chains coupled ferromagnetically were unsuccessful. Monolayer calculations find no ferromagnetic moment for Cr on the Cu(001) surface, but there is a significant moment found for the antiferromagnetic $c(2 \times 2)$ monolayer of Cr on Ag(001) [9, 5], suggesting that Cr monolayers favour this spin configuration. This appears to be reflected in the chain calculations favouring the antiferromagnetic coupling between chains. Calculations of antiferromagnetic chains (e.g., chains in which the spins alternate along the chain) and an antiferromagnetic $c(2 \times 2)$ monolayer of Cr on Cu(001) may shed more light on this matter, although without accurate total energy calculations it is not possible to determine the ground state spin configuration. The Cr 3b moment is significantly higher than the 2 site moment. This behaviour is also seen for the Fe chain, although less dramatically, and the Mn 3b and 2 moments are equal.

If calculations were performed for larger arrays of chains, the moments for the central chains should become steadily closer to the monolayer moment as the local environment becomes more similar to that for a monolayer site. Calculations of larger chain arrays would also allow study of possible oscillatory effects, e.g., the 3b site moment. It is possible that odd numbers of chains will tend to exhibit an increased moment for the edge chains than comparable arrays of even chains.

We can also examine some densities of states plots for multiple chain systems. Figure (6.18) shows the DOS for the various chain sites for Fe chains on Cu, compared with an Fe monolayer on Cu. The DOS plots behave largely as one would expect based on the number of nearest neighbour Fe atoms of the chain sites. The single chain site (D1) displays the narrowest DOS and largest exchange-split, corresponding to the largest enhancement of the moment. The edge sites (2, 3b and 4b) look broadly similar, with a slight enhancement of the exchange-split over the monolayer. The central sites (3a and 4a) differ little from the monolayer DOS. Examining the minority spin DOS, for the D1 site the three peaked structure is clearly present. For the edge sites this structure is still present, although less clear than in the D1 case, while for the central sites the DOS resembles that of the monolayer.

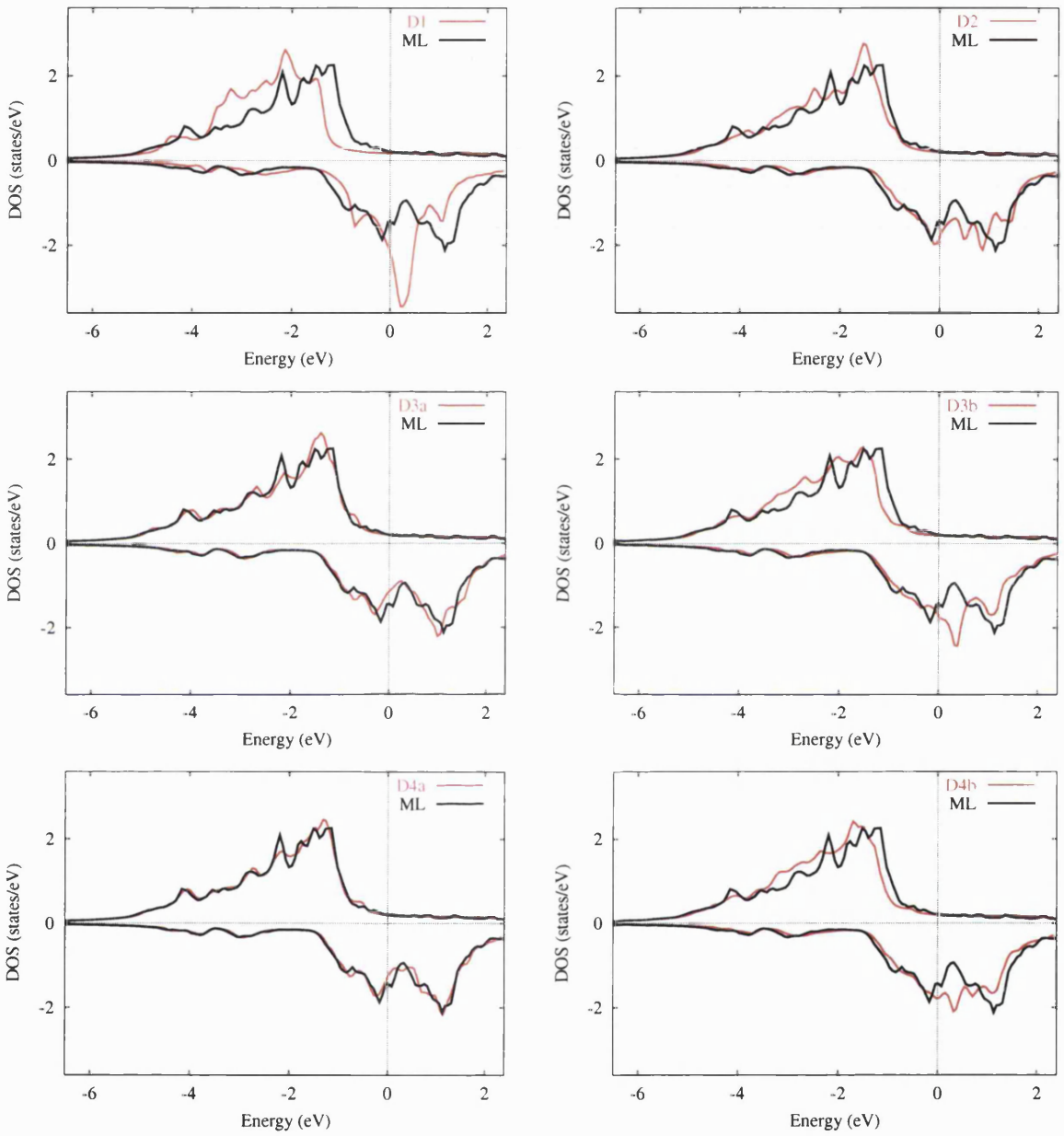

Figure 6.18: Spin-resolved densities of states for the unique chain sites of 1, 2, 3 and 4 Fe chains on the Cu(001) surface, compared to the DOS for an Fe monolayer on the Cu surface. In each case the upper panel shows the majority spin DOS and the lower panel the minority spin DOS.

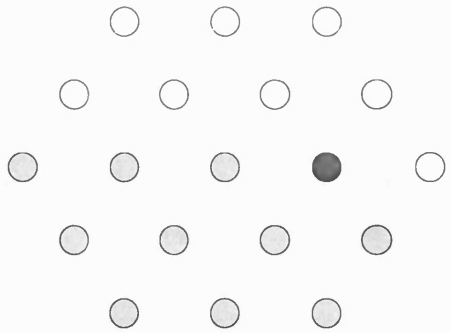

Figure 6.19: Cross-sectional schematic of the cluster geometry for a step-edge mimic structure. The darker chain is the adchain decorating the step, which is made up of the 3 Cu chains on the surface.

6.7 Step-edge calculations

One further system of interest is that of a stepped surface with decorated steps. Systems of this type are one method by which one-dimensional structures can be experimentally realised, as was discussed in the introduction. A decorated step-edge can be approximated in the method presented in this thesis by placing several substrate chains on the surface, adjacent to the adchain that would be present in a single chain defect calculation. This type of structure is shown in figure (6.19) for a 19 chain cluster. If we take this as the structure for an Fe chain on a Cu surface calculation, then across the central layer we have 3 Cu chains, an Fe chain and a vacuum chain.

This system can effectively be viewed as falling between the chain on the surface and the embedded chain cases. With respect to the number of Cu nearest neighbours for the adchain, the chain on the surface has 4, the embedded chain has 6, while the step-edge chain has 5. Using the familiar argument that hybridisation with the Cu substrate tends to reduce the moment, we expect the step-edge chain moment to fall between the values for the single and embedded chains.

The moments for Cr, Mn, Fe and Co step-edge adchains on the Cu(001) surface, calculated with the 19 chain structure shown in figure (6.19), are shown in figure (6.20) and listed in table (6.6). As expected the step-edge chain moments fall between the single chain and embedded chain moments. This is in agreement with the mechanism whereby increasing the number of Cu nearest neighbours increases the hybridisation between the Cu sp states and the $3d$ chain orbitals,

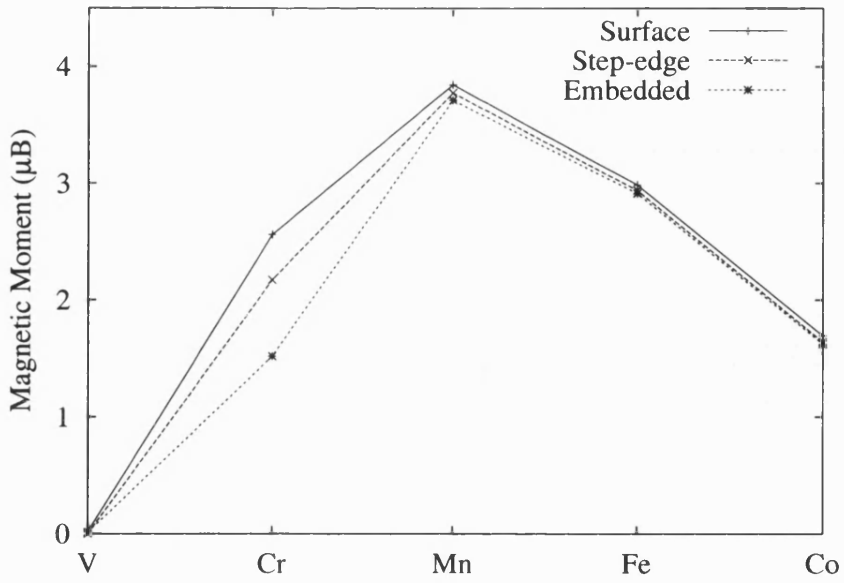

Figure 6.20: Magnetic moments for $3d$ single chains, step-edge chains and embedded chains on the Cu(001) surface.

thus broadening the DOS and reducing the magnetic moment.

In order to test the convergence properties of the approximate step-edge geometry a 24 chain Fe defect calculation was also performed. Across the central layer in the 24 chain case we have 4 Cu chains, an Fe chain and a vacuum chain. The moments for the Fe chain and the immediately adjacent Cu chains were consistent to within $0.002\mu_B$ to those from the 19 chain calculation, suggesting that the 19 chain geometry is sufficient to converge the magnetic moments for these types of approximate step-edge calculations.

	Cr	Mn	Fe	Co
Single chain	2.56	3.85	2.99	1.69
Step-edge chain	2.17	3.77	2.94	1.64
Embedded chain	1.52	3.71	2.91	1.62

Table 6.6: Magnetic moments in μ_B for $3d$ single chains, step-edge chains and embedded chains on the Cu(001) surface.

Chapter 7

Conclusions

7.1 Summary

An extension to layer multiple scattering theory, for performing electronic structure calculations within the single particle approximation to density functional theory, has been developed to allow for the treatment of systems with one-dimensional periodicity as defects embedded within systems with two-dimensional periodicity. This method is ideal for the study of monatomic wires on surfaces, for example, and avoids the use of ersatz supercell geometries.

An integral part of this development has been the derivation of a practical solution of the Poisson equation for a system with one-dimensional periodicity. This involves one-dimensional lattice sums, for which an Ewald sum technique for one-dimensional lattices has been derived and implemented. Comparison of the one-dimensional solution for arrays of chains to existing two-dimensional solutions has validated the method and confirmed its accuracy.

Expressions have been derived for the τ-matrix of a system with a defect which is periodic in one-dimension. This allows calculation of the τ-matrix for such a system from just the single site t-matrices, and the τ-matrices of the unperturbed reference system.

Systematic calculations of both bulk and surface defect chain systems have been

performed. The results demonstrate the convergence of the calculations with respect to **k**-point set, angular momentum cutoff, and cluster size. The convergence tests indicate that including a single shell of chains around the defect is sufficient to obtain converged densities of states and magnetic moments for the defect site.

This new theoretical tool has been used to study the electronic structure of $3d$ chains on the Cu(001) surface. Self-consistent calculations have been performed for a variety of chain configurations, including single and multiple chains on the surface, embedded chains and step-edge type chains. The systems have been investigated by studying the local densities of states, total charges and magnetic moments. Reference calculations have also been performed for $3d$ monolayers on the Cu(001) surface, using the standard LKKR method. These monolayer results were consistent with previous calculations for such systems [5].

The magnetic moments obtained for the chain calculations were consistent with the monolayer results, and also with previous calculations for $3d$ monolayers [5] and adatoms [75] on the Cu(001) surface using different methods. The chain systems can be thought of as falling between the monolayer (2D) and adatom (0D) regimes, and the values for the moments reflect this.

The behaviour of the magnetic moments for the chain systems has been successfully interpreted within a simple Stoner-like itinerant magnetism model. Trends in the moments across the $3d$ series, and between the various systems, can be understood in terms of the interaction between orbitals. Hybridisation between the d-orbitals of the $3d$ chain atoms and the sp-orbitals of the Cu substrate leads to broadening of the DOS, and a reduction in the magnetic moment. Hybridisation between the d-orbitals of the $3d$ chain atoms tends to reduce the moments for elements earlier in the series, while for the later elements this interaction can increase the moment.

The results for the different chain systems confirm these mechanisms. The moments for the single, embedded and step-edge chains behave as expected from considering the number of Cu nearest neighbour atoms. The moments for the multiple chain arrays are seen to approach the monolayer moments as more chains are added. Multiple arrays of Cr chains couple antiferromagnetically, which is consistent with theoretical predictions that a Cr monolayer on Cu(001) has a significant moment only in the antiferromagnetic spin configuration.

7.2 Future work

With regard to future work in this area, building upon that reported in this thesis, there are several avenues which would be of interest:

1. **Larger multiple chain arrays.**

   One possibility is the calculation of larger multiple chain arrays, with a view to examining the possible oscillatory effects seen in these systems. The edge chain moments for the 3 chain array are higher than the corresponding moments in the 2 and 4 chain arrays for some of the elements. Calculations for 5 chain arrays may indicate whether this is a feature of odd-chain arrays, or an exception for the 3 chain case.

2. **Alternative systems.**

   Extending these calculations to other systems is another possibility. Previous chain calculations include $4d$ chains on a vicinal Ag surface [4], Rh chains on the Ag(001) surface [3] and Co chains on the Pd(110) surface [105]. Calculations predict significant moments for some $3d$, $4d$ and $5d$ elements as monolayers on Ag(001) and Au(001) [9]. Further chain calculations could be performed for the $3d$, $4d$ and $5d$ transition metals as chains on the Ag(001) and Au(001) surfaces. Comparison to previous monolayer, chain and adatom calculations would then be possible.

3. **Full potential calculations.**

   The extension of the theory beyond the ASA to use the full non-spherical potential would represent a significant improvement. The site potentials in a chain on a surface are likely to be far from spherically symmetric. While useful results have been obtained in these chain calculations, a full potential scheme would serve to increase the accuracy of the calculations considerably. Use of the full non-spherical potentials opens up the possibility of accurate calculations of the energetics of chain systems. Total energy calculations would be feasible to determine which spin configuration represents the ground state in magnetic systems.

4. **Antiferromagnetic spin configurations.**

   Calculations for antiferromagnetic chains would also be of interest. The early $3d$ elements (e.g., V, Cr and Mn) are predicted to favour antiferro-

magnetic spin configurations as monolayers on Ag(001). The multi-chain Cr arrays were found to couple antiferromagnetically. Use of full potential total energy calculations would enable predictions to be made for the ground state spin configuration of these systems. Calculations of antiferromagnetic chains result in double the number of defect sites, due to the increased size of the unit cell along the chain axis.

5. **Experimental properties.**

The method used in this thesis is concerned with the calculation of the Green function, from which many other properties of interest can then be obtained, e.g., the charge density. However the Green function can also be used as the basis for calculations of properties that are obtained in experimental studies, e.g., photoemission and inverse photoemission spectra, and modelling of STM data. This would be useful as these methods are key surface science probes used to experimentally study monatomic chain systems.

Appendix A

$S_L(\mathbf{R})$ equations

A.1 One-dimensional lattice sums for $y = r_{\|}$

In terms of $S(\mathbf{r})$, the lattice sums required for the Madelung potential $S_L(\mathbf{R})$ may be obtained as [85]

$$S_L(\mathbf{R}) = \frac{1}{(2\ell-1)!!}\left[\mathcal{Y}_L(-\nabla)S(\mathbf{r})\right]_{\mathbf{r}=\mathbf{R}} \tag{A.1}$$

where

$$\mathcal{Y}_L(\mathbf{r}) = r^{\ell}Y_L(\mathbf{r}). \tag{A.2}$$

is a polynomial in x, y, z and the differential operator in (A.1) understood to be the result of substituting $x \rightarrow -\partial_x$, etc. Due to the cylindrical symmetry of the system taking the z-axis to coincide with $\mathbf{e}_{\|}$ results in more elegant expressions for the $S_L(\mathbf{R})$ terms, hence these are the expressions given in chapter 4. In order to remain compatible with the 2D LKKR method, described in chapter 3, a practical implementation of this 1D Ewald technique has been realised in which the chains are parallel to the y-axis, with the z-axis normal to the 2D layers. Thus the $S_L(\mathbf{R})$ expressions used in this code take the y-axis to coincide with $\mathbf{e}_{\|}$, and the corresponding expressions are given here .

Applying (A.1) to (4.20,4.21) and taking the z-axis to coincide with $\mathbf{e}_{\|}$, we obtain

$$S_{00}(\mathbf{R}) = \frac{S(\mathbf{R})}{\sqrt{4\pi}} \tag{A.3}$$

$$\begin{aligned} S_{10}(\mathbf{R}) = & \frac{2}{\sqrt{\pi}} {\sum_{\mathbf{u}_\parallel}}' \frac{\Gamma(3/2, \mu|\mathbf{R}-\mathbf{u}_\parallel|^2)}{|\mathbf{R}-\mathbf{u}_\parallel|^2} Y_{10}(\mathbf{R}-\mathbf{u}_\parallel) \\ & + \frac{2z\sqrt{3}}{a\sqrt{\pi}} \sum_{g_\parallel>0} g_\parallel \cos(g_\parallel R_\parallel) I_1(g_\parallel/2, R_\perp, \mu) \\ & - \frac{z}{aR_\perp^2} \frac{\sqrt{3}}{\sqrt{\pi}} \left(e^{-\mu R_\perp^2} - 1\right) \end{aligned} \tag{A.4}$$

$$\begin{aligned} S_{11}(\mathbf{R}) = & \frac{2}{\sqrt{\pi}} {\sum_{\mathbf{u}_\parallel}}' \frac{\Gamma(3/2, \mu|\mathbf{R}-\mathbf{u}_\parallel|^2)}{|\mathbf{R}-\mathbf{u}_\parallel|^2} Y_{11}(\mathbf{R}-\mathbf{u}_\parallel) \\ & - \frac{\sqrt{3}}{a\sqrt{2\pi}} \sum_{g_\parallel>0} \Big[2x \cos(g_\parallel R_\parallel) I_1(g_\parallel/2, R_\perp, \mu) \\ & + i g_\parallel \sin(g_\parallel R_\parallel) I_0(g_\parallel/2, R_\perp, \mu)\Big] \\ & + \frac{x}{aR_\perp^2} \frac{\sqrt{3}}{\sqrt{2\pi}} \left(e^{-\mu R_\perp^2} - 1\right) \end{aligned} \tag{A.5}$$

$$\begin{aligned} S_{20}(\mathbf{R}) = & \frac{4}{3\sqrt{\pi}} {\sum_{\mathbf{u}_\parallel}}' \frac{\Gamma(5/2, \mu|\mathbf{R}-\mathbf{u}_\parallel|^2)}{|\mathbf{R}-\mathbf{u}_\parallel|^3} Y_{20}(\mathbf{R}-\mathbf{u}_\parallel) \\ & - \frac{\sqrt{5}}{3a\sqrt{4\pi}} \sum_{g_\parallel>0} \cos(g_\parallel R_\parallel) \Big[g_\parallel^2 I_0(g_\parallel/2, R_\perp, \mu) - 2I_1(g_\parallel/2, R_\perp, \mu) \\ & + (8z^2 - 4x^2) I_2(g_\parallel/2, R_\perp, \mu)\Big] \\ & + \frac{\sqrt{5}}{3a\sqrt{4\pi}} \left[\left(\frac{1}{R_\parallel^2} - \frac{(4z^2-2x^2)}{R_\parallel^4} - \frac{\mu(4z^2-2x^2)}{R_\parallel^2}\right) e^{\mu R_\parallel^2} \right. \\ & \left. + \frac{(4z^2-2x^2)}{R_\parallel^4} - \frac{1}{R_\parallel^2}\right] \end{aligned} \tag{A.6}$$

$$\begin{aligned} S_{21}(\mathbf{R}) = & \frac{4}{3\sqrt{\pi}} {\sum_{\mathbf{u}_\parallel}}' \frac{\Gamma(5/2, \mu|\mathbf{R}-\mathbf{u}_\parallel|^2)}{|\mathbf{R}-\mathbf{u}_\parallel|^3} Y_{21}(\mathbf{R}-\mathbf{u}_\parallel) \\ & - \frac{\sqrt{10}}{a\sqrt{3\pi}} \sum_{g_\parallel>0} \Big[2zx \cos(g_\parallel R_\parallel) I_2(g_\parallel/2, R_\perp, \mu) \\ & + iz g_\parallel \sin(g_\parallel R_\parallel) I_1(g_\parallel/2, R_\perp, \mu)\Big] \\ & + \frac{zx\sqrt{10}}{aR_\parallel^2\sqrt{3}} \left[\left(\frac{1}{R_\parallel^2} + \mu\right) e^{-\mu R_\parallel^2} - \frac{1}{R_\parallel^2}\right] \end{aligned} \tag{A.7}$$

$$
\begin{aligned}
S_{22}(\mathbf{R}) = & \frac{4}{3\sqrt{\pi}} \sum_{\mathbf{u}_\parallel}{}' \frac{\Gamma(5/2, \mu|\mathbf{R}-\mathbf{u}_\parallel|^2)}{|\mathbf{R}-\mathbf{u}_\parallel|^3} Y_{22}(\mathbf{R}-\mathbf{u}_\parallel) \\
& + \frac{\sqrt{5}}{a\sqrt{24\pi}} \sum_{g_\parallel>0} \Big[\Big(4x^2 I_2(g_\parallel/2, R_\perp, \mu) - 2I_1(g_\parallel/2, R_\perp, \mu) \\
& + g_\parallel^2 I_0(g_\parallel/2, R_\perp, \mu) \Big) \cos(g_\parallel R_\parallel) + i4x g_\parallel I_1(g_\parallel/2, R_\perp, \mu) \sin(g_\parallel R_\parallel) \Big] \\
& + \frac{\sqrt{5}}{a\sqrt{24\pi}} \left[\left(\frac{1}{R_\parallel^2} - \frac{2x^2}{R_\parallel^4} - \frac{2\mu x^2}{R_\parallel^2} \right) e^{\mu R_\parallel^2} + \frac{2x^2}{R_\parallel^4} - \frac{1}{R_\parallel^2} \right]
\end{aligned}
\tag{A.8}
$$

References

[1] M Abramowitz and I A Stegun, editors. *Handbook of Mathematical Functions.* Dover, New York, 1972.

[2] K N Altmann, J N Crain, A Kirakosian, J-L Lin, D Y Petrovykh, F J Himpsel, and R Losio. *Phys. Rev. B*, 64:035406, 2001.

[3] D I Bazhanov, W Hergert, V S Stepanyuk, A A Katsnelson, P Rennert, K Kokko, and C Demangeat. *Phys. Rev. B*, 62:6415, 2000.

[4] V Bellini, N Papanikolaou, R Zeller, and P H Dederichs. *Phys. Rev. B*, 64:094403, 2001.

[5] L H Bennett and R E Watson, editors. *Magnetic Multilayers.* World Scientific Publishing Co. Pte. Ltd., 1994.

[6] G Bihlmayer, Ph Kurz, and S Blugel. *Phys. Rev. B*, 62:4726, 2000.

[7] G Bihlmayer, X Nie, and S Blugel. unpublished.

[8] A Blondel, J P Meier, B Doudin, and J-Ph Ansermet. *Appl. Phys. Lett.*, 65:3019, 1994.

[9] S Blugel. *Phys. Rev. Lett.*, 68:851, 1992.

[10] S Blugel. *Europhys. Lett.*, 18:257, 1992.

[11] S Blugel. *Phys. Rev. B*, 51:2025, 1995.

[12] S Blugel. *Appl. Phys. A*, 63:595, 1996.

[13] S Blugel, B Drittler, R Zeller, and P H Dederichs. *Appl. Phys. A*, 49:547, 1989.

[14] M V Bollinger, J V Lauritsen, K W Jacobsen, J K Norskov, S Helveg, and F Besenbacher. *Phys. Rev. B*, 61:5133, 2000.

[15] H Bross and M Kauzmann. *Phys. Rev. B*, 51:17135, 1995.

[16] C G Broyden. *Math. Comput.*, 19:577, 1965.

[17] W H Butler. *Phys. Rev. B*, 14:468, 1976.

[18] R J Cellota, R Gupta, R E Scholten, and J J McClelland. *J. Appl. Phys.*, 79:6079, 1996.

[19] S Crampin. *Self Consistent Charge Defects at Isolated Planar Defects in Metals.* PhD thesis, 1989.

[20] S Crampin. *J. Phys.: Condens. Matter*, 5:4647, 1993.

[21] S Crampin. unpublished.

[22] M F Crommie, C P Lutz, and D M Eigler. *Science*, 262:218, 1993.

[23] S L Cunningham. *Phys. Rev. B*, 10:1988, 1974.

[24] A Dallmeyer, C Carbone, W Eberhardt, C Pampuch, O Rader, W Gudat, P Gambardella, and K Kern. *Phys. Rev. B*, 61:5133, 2000.

[25] J de la Figuera, M A Huerta-Garnica, J E Prieto, C Ocal, and R Miranda. *Appl. Phys. Lett.*, 66:1006, 1995.

[26] J Delhalle, J Cizek, I Flamant, J L Calais, and J G Fripiat. *J. Chem. Phys.*, 101:10717, 1994.

[27] J Dorantes-Davila, A Mokrani, H Dreysse, and C Demangeat. *J. Magn. Magn. Mater.*, 165:268, 1997.

[28] J Dorantes-Davila and G M Pastor. *Phys. Rev. Lett.*, 81:208, 1998.

[29] R Druzinic and W Hubner. *Phys. Rev. B*, 55:347, 1997.

[30] Ising E. *Z. Phys.*, 31:253, 1925.

[31] H J Elmers, J Hauschild, H Hoche, U Gradmann, H Bethge, D Heuer, and U Kohler. *Phys. Rev. Lett.*, 73:898, 1994.

[32] P P Ewald. *Ann. Phys.*, 64:253, 1921.

[33] J S Faulkner. *Phys. Rev. B*, 19:6186, 1979.

[34] J S Faulkner. *Phys. Rev. B*, 32:1339, 1985.

[35] J S Faulkner. *Phys. Rev. B*, 38:1686, 1988.

[36] J S Faulkner and G M Stocks. *Phys. Rev. B*, 21:3222, 1980.

[37] V Fock. *Z. Phys.*, 61:126, 1930.

[38] C L Fu, A J Freeman, and T Oguchi. *Phys. Rev. Lett.*, 54:2700, 1985.

[39] P Gambardella, M Blanc, L Bergi, K Kuhnke, and K Kern. *Surf. Sci.*, 449:93, 2000.

[40] P Gambardella, M Blanc, H Brune, K Kuhnke, and K Kern. *Phys. Rev. B*, 61:2254, 2000.

[41] P Gambardella, A Dallmeyer, K Maiti, M C Malagoli, W Eberhardt, K Kern, and C Carbone. *Nature*, 416:301, 2002.

[42] J G Gay, J R Smith, and F J Arlinghaus. *Phys. Rev. Lett.*, 42:332, 1979.

[43] R Gomez-Abal and A M Llois. *Phys. Rev. B*, 65:155426, 2002.

[44] A Gonis. *Phys. Rev. B*, 34:5914, 1986.

[45] A Gonis. *Green Functions for Ordered and Disordered Systems.* North-Holland, 1992.

[46] A Gonis and W H Butler. *Multiple Scattering in Solids.* Springer, New York, 2000.

[47] A Gonis, X G Zhang, and D M Nicholson. *Phys. Rev. B*, 38:3564, 1988.

[48] A Gonis, X G Zhang, and D M Nicholson. *Phys. Rev. B*, 40:947, 1988.

[49] B L Györffy and M J Stott. *Solid State Commun.*, 9:613, 1971.

[50] F S Ham and B Segall. *Phys. Rev.*, 124:1786, 1961.

[51] M S Hantush and C E Jacob. *Trans. Am. Geophys. Union*, 36:95, 1955.

[52] W A Harrison. *Solid State Theory.* McGraw-Hill, New York, 1970.

[53] D R Hartree. *Proc. Cambridge Philos. Soc.*, 24:89, 1928.

[54] J Hauschild, H J Elmers, and U Gradmann. *Phys. Rev. B*, 57:677, 1998.

[55] F J Himpsel, K N Altmann, R Bennewitz, J N Crain, A Kirakosian, J-L Lin, and J L McChesney. *J. Phys.: Condens. Matter*, 13:11097, 2001.

[56] F J Himpsel and J E Ortega. *Phys. Rev. B*, 50:4992, 1994.

[57] F J Himpsel, J E Ortega, G J Mankey, and R F Willis. *Adv. Phys.*, 47:511, 1998.

[58] P Hohenberg and W Kohn. *Phys. Rev.*, 136:B864, 1964.

[59] J D Jackson. *Classical Electrodynamics*. John Wiley & Sons, 1975.

[60] J F Janak. *Phys. Rev. B*, 16:255, 1977.

[61] T Jung, Y W Mo, and F J Himpsel. *Phys. Rev. Lett.*, 74:1641, 1995.

[62] T Jung, R Schlittler, J K Gimzewski, and F J Himpsel. *Appl. Phys. A*, 61:467, 1995.

[63] K Kambe. *Z. Naturforsch*, 22a:322, 1967.

[64] K Kambe. *Z. Naturforsch*, 22a:422, 1967.

[65] K Kambe. *Z. Naturforsch*, 23a:1280, 1968.

[66] K Kambe. *Z. Naturforsch*, 24c:1432, 1969.

[67] K Kern, H Niehus, A Schatz, P Zeppenfeld, J Goerge, and G Comsa. *Phys. Rev. Lett.*, 67:855, 1991.

[68] S J Koh and G Ehrlich. *Phys. Rev. Lett.*, 87:106103, 2001.

[69] W Kohn and N Rostoker. *Phys. Rev.*, 94:1111, 1953.

[70] W Kohn and L J Sham. *Phys. Rev.*, 140:A1133, 1965.

[71] J Korringa. *Physica*, XIII:392, 1947.

[72] P Kruger, M Taguchi, and S Meza-Aguilar. *Phys. Rev. B*, 61:15277, 2000.

[73] N D Lang and Ph Avouris. *Phys. Rev. Lett.*, 81:3515, 1998.

[74] N D Lang and Ph Avouris. *Phys. Rev. B*, 62:7325, 2000.

[75] P Lang, V S Stepanyuk, K Wildberger, R Zeller, and P H Dederichs. *Solid State Commun.*, 92:755, 1994.

[76] D J Langridge, J F Hart, and S Crampin. *Comput. Phys. Commun.*, 134:78, 2001.

[77] R B Laughlin. *Rev. Mod. Phys.*, 71:863, 1999.

[78] Y Li, M C Bartelt, J W Evans, N Waelchli, E Kampshoff, and K Kern. *Phys. Rev. B*, 56:12539, 1997.

[79] K Liu, K Nagodawithana, P C Searson, and C L Chien. *Phys. Rev. B*, 51:381, 1995.

[80] R Losio, K N Altmann, and F J Himpsel. *Phys. Rev. B*, 61:10845, 2000.

[81] R Losio, K N Altmann, A Kirakosian, J-L Lin, D Y Petrovykh, and F J Himpsel. *Phys. Rev. Lett.*, 86:4632, 2001.

[82] J M Luttinger. *J. Math. Phys.*, 4:1154, 1963.

[83] J M MacLaren, S Crampin, D D Vvedensky, and J B Pendry. *Phys. Rev. B*, 40:12164, 1989.

[84] V Marsico, M Blanc, K Kuhnke, and K Kern. *Phys. Rev. Lett.*, 78:94, 1997.

[85] M S Methfessel. *Phd Thesis.* PhD thesis, University of Nijmegen, 1986.

[86] J Molenaar. *J. Phys. C*, 21:1455, 1988.

[87] V L Moruzzi, J F Janak, and A R Williams. *Calculated Electronic Properties of Metals.* Pergamon, New York, 1978.

[88] R K Nesbet. *Phys. Rev. B*, 30:4230, 1984.

[89] R K Nesbet. *Phys. Rev. B*, 33:8027, 1986.

[90] B Nonas, K Wildberger, R Zeller, and P H Dederichs. *J. Magn. Magn. Mater.*, 165:137, 1997.

[91] B Nonas, K Wildberger, R Zeller, P H Dederichs, and B L Gyorffy. *Phys. Rev. B*, 57:84, 1998.

[92] Gunnarsson O. *J Phys. F*, 6:587, 1976.

[93] S Okada and A Oshiyama. *Phys. Rev. B*, 62:R13286, 2000.

[94] C Pampuch, O Rader, T Kachel, W Gudat, C Carbone, R Klasges, G Bihlmayer, S Blugel, and W Eberhardt. *Phys. Rev. Lett.*, 85:2561, 2000.

[95] R Pascal, Ch Zarnitz, M Bode, and R Wiesendanger. *Phys. Rev. B*, 56:3636, 1997.

[96] R F Peierls. *Quantum Theory of Solids.* Oxford: Clarendon, 1955.

[97] J B Pendry. *Low Energy Electron Diffraction.* Academic Press, London, 1974.

[98] R M Penner. *J. Phys. Chem. B*, 106:3339, 2002.

[99] J P Perdew and Y Wang. *Phys. Rev. B*, 45:13244, 1992.

[100] J L Perez-Diaz and M C Munoz. *Phys. Rev. B*, 50:8824, 1994.

[101] D Y Petrovykh, J K, F J Himpsel, and T Jung. *Surf. Sci.*, 407:189, 1998.

[102] L Piraux, J M George, J F Despres, C Leroy, E Ferain, R Legras, K Ounadjela, and A Fert. *Appl. Phys. Lett.*, 65:2482, 1994.

[103] L Pleth Nielsen, F Besenbacher, I Stensgaard, E Laegsgaard, C Engdahl, P Stoltze, and J K Norskov. *Phys. Rev. Lett.*, 74:1159, 1995.

[104] W H Press, S A Teukolsky, W T Vetterling, and B P Flannery. *Numerical Recipes.* Cambridge University Press, Cambridge, 1994.

[105] R Robles, J Izquierdo, and A Vega. *Phys. Rev. B*, 61:6848, 2000.

[106] H Roder, E Hahn, H Brune, J-P Bucher, and K Kern. *Nature*, 366:141, 1993.

[107] G Rubio-Bollinger, S R Bahn, N Agrait, K W Jacobsen, and S Vieira. *Phys. Rev. Lett.*, 87:026101, 2001.

[108] D Sanchez-Portal, J D Gale, A Garcia, and R M Martin. *Phys. Rev. B*, 65:081401, 2002.

[109] L I Schiff. *Quantum Mechanics.* McGraw-Hill Book Company, 1955.

[110] P Segovia, D Purdie, M Hengsberger, and Y Baer. *Nature*, 402:504, 1999.

[111] J Shen, R Skomski, M Klaua, H Jenniches, S Sundar Manoharan, and J Kirschner. *Phys. Rev. B*, 56:2340, 1997.

[112] H-S Sim, H-W Lee, and K J Chang. *Phys. Rev. Lett.*, 87:096803, 2001.

[113] H L Skriver. *The LMTO Method.* Springer, Berlin, 1984.

[114] H L Skriver and N M Rosengaard. *Phys. Rev. B*, 43:9538, 1991.

[115] J R Smith, J G Gay, and F J Arlinghaus. *Phys. Rev. B*, 21:2201, 1980.

[116] K S Sohn, D G Dempsey, L Kleinmann, and E Caruthers. *Phys. Rev. B*, 13:1515, 1976.

[117] V S Stepanyuk, W Hergert, P Rennert, J Izquierdo, A Vega, and L C Balbas. *Phys. Rev. B*, 54:R14020, 1998.

[118] V S Stepanyuk, W Hergert, P Rennert, K Wildberger, R Zeller, and P H Dederichs. *Phys. Rev. B*, 54:14121, 1996.

[119] V S Stepanyuk, W Hergert, K Wildberger, R Zeller, and P H Dederichs. *Phys. Rev. B*, 53:2121, 1996.

[120] E C Stoner. *Proc. Roy. Soc.*, 165:372, 1938.

[121] E C Stoner. *Proc. Roy. Soc.*, 169:339, 1939.

[122] H L Stormer. *Rev. Mod. Phys.*, 71:875, 1999.

[123] M A Van Hove and G A Somorjai. *Surf. Sci.*, 92:489, 1980.

[124] J Viernow, J-L Lin, D Y Petrovykh, F M Leibsle, F K Men, and F J Himpsel. *Appl. Phys. Lett.*, 72:948, 1998.

[125] P Villasenor-Gonzalez, J Dorantes-Davila, H Dreysse, and G M Pastor. *Phys. Rev. B*, 55:15084, 1997.

[126] S Watanabe. *Phys. Rev. B*, 54:R17308, 1996.

[127] P Weinberger. *Electron scattering theory for ordered and disordered matter.* Oxford University press, New York, 1990.

[128] K Wildberger, V S Stepanyuk, P Lang, R Zeller, and P H Dederichs. *Phys. Rev. Lett.*, 75:509, 1995.

[129] A Yajima. *Phys. Rev. B*, 60:1456, 1999.

[130] A I Yanson, G Rubio-Bollinger, H E van den Brom, N Agrait, and J M van Ruitenbeek. *Nature*, 396:783, 1998.

[131] N Zabala, M J Puska, and R M Nieminen. *Phys. Rev. Lett.*, 80:3336, 1998.

[132] A Zangwill. *Physics at Surfaces.* Cambridge University Press, 1988.

[133] R Zeller. *Phys. Rev. B*, 30:4230, 1984.

[134] R Zeller. *J. Phys. C*, 20:2347, 1987.

[135] R Zeller, P H Dederichs, B Ujfalussy, L Szunyogh, and P Weinberger. *Phys. Rev. B*, 52:8807, 1995.